

DISS. ETH NO. 24459

SELECTIVE HYDROGENATION OF ALKYNES FOR VITAMIN PRODUCTION

A thesis submitted to attain the degree of
DOCTOR OF SCIENCES of ETH ZURICH

(Dr. sc. ETH Zurich)

presented by

SERGIO VERNUCCIO

Laurea Specialistica, Università degli Studi di Napoli Federico II

born on 28.01.1986

citizen of Italy

accepted on the recommendation of

Prof. Dr. Philipp Rudolf von Rohr (ETH Zurich), examiner

Prof. Dr. Massimo Morbidelli (ETH Zurich), co-examiner

Dr. Jonathan Medlock (DSM Nutritional Products), co-examiner

2017

*Dans la vie, rien n'est à craindre,
tout est à comprendre.*

Marie Curie

Acknowledgements

First of all, I would like to sincerely thank my advisor Prof. Dr. Philipp Rudolf von Rohr for accepting me in his research group. Philipp, I truly appreciate the opportunity you gave me to move back from industry to academia. Thank you very much for your trust, support, constructive criticism and for investing time in my scientific development.

I would like to extend my gratitude to Prof. Dr. Massimo Morbidelli and to Dr. Jonathan Medlock for having agreed to act as co-examiners of this PhD thesis.

My research has benefited from a number of collaborations. Without the strong technical and financial support of DSM Nutritional Products and in particular of Dr. Jonathan Medlock, Dr. Roman Goy, Dr. Simon Walter, Dr. Andreas Keller, Dr. Werner Bonrath, Dr. Francesco Mascarello, this project would not have been possible. The fruitful discussions during our regular meetings have undoubtedly guided the development of this work.

Jonathan and Roman, I sincerely appreciate the time you invested in the design of the catalyst. Your scientific inputs were essential to shape many parts of this thesis.

I also want to express my gratitude to the Swiss Commission for Technology and Innovation (CTI) for their financial support.

The Scientific Center for Optical and Electron Microscopy (ScopeM) at ETH Zürich is acknowledged for providing access to their facilities. Thank you, in particular, to Dr. Anne Greet Bittermann, Dr. Simona Rodighiero, Dr. Joakim Reuteler and Dr. Karsten Kunze for introducing me into the world of Electron Microscopy.

I also want to express my gratitude to Dr. Robert Büchel for his help with BET analysis and temperature programmed studies, to Dr. Frank Krumeich for the STEM analysis and to Sung Min Kim for the CO chemisorption.

I am indebted to the students who worked with me giving a strong contribution to the results presented in this thesis. In particular, many thanks go to Mazlum, Quirin, Philip, Adrian, David and Jordan.

Thank you also to Eliane, Bruno, Peter, Daniel and Stephan for their exceptional administrative and technical support.

Current and previous members of LTR are thanked for the enjoyable working atmosphere. Thank you Agnieszka, Christoph, Christos, Denis, Dragana, Dustin, Brian, Edoardo, Feifei, Gina, Helena, Marco, Martin, Max, Michael, Paolo, Pascal, Richard, Roger, Thierry, Thomas, Vito, Yannick for being great colleagues and friends. Special thanks go to Marco for our fruitful collaboration on the project.

All my friends in Zurich are thanked for the nice moments we have shared, in particular Vito for our daily discussions and Italian coffee breaks, Paolo for being a real “Maestro” with his precious advices about research and life, Basilio for the nice games on Saturday evening and the football matches we watched together. Marco G. thank you for the great time we spent together. It would have been definitely nicer knowing you before. Nevertheless, I am very glad that our paths crossed.

Dr. Ilaria Di Somma and Prof. Roberto Andreozzi deserve a special thank for opening my eyes and introducing me, several years ago, into the beautiful world of academic research.

I further thank my friend Mauro for his support before the start of my doctoral studies, during a difficult period of my life.

One of the greatest thanks goes to my best friends Giovanna and Giuseppe. Despite the distance they were always ready to discuss about my problems, listening to my stories, and supporting me after every failure. You are the best friends I could ever ask for! Giuseppe, thank you also for your scientific inputs and continuous advices on my papers and on this thesis.

Finally, my deep and sincere gratitude to my family for their constant presence in my life. I am grateful to my brother Giovanni, my sister Gloria and my uncles Eugenio and Franco for always being there for me as mentors and guides.

Mamma and papà, I will be forever indebted to you for your infinite love and care. This long journey would not have been possible without your support and encouragement over the years. For this, and for many other reasons I dedicate this milestone to you.

Sergio Vernuccio

Zurich, July 2017

Abstract

Heterogeneously-catalysed hydrogenations represent key reactions for many industrial processes. In particular, selective hydrogenations of alkynes lie at the heart of pharmaceutical and fine chemicals industry for production of vitamins.

These reactions are usually carried out in batch processes in the presence of supported palladium-based catalysts modified with the addition of lead. The presence of this toxic element strongly limits the sustainability of these processes. Furthermore, the need of energy savings led, in the past decade, to a growing interest in new technologies for Process Intensification. For the aforementioned reasons, new reactor solutions need to be further investigated in order to reduce the energy consumption and to establish safe and environment-friendly process solutions.

This thesis contributes to the application and characterization of structured reactors for three-phase solvent-free continuous hydrogenation of alkynes. The proposed reactors consist of metal porous structures, with regular geometries, coated with a zinc oxide/alumina layer and impregnated with palladium nanoparticles.

The performance of this structured catalyst, in terms of reaction selectivity and activity, is found to be higher than that of Lindlar catalyst. This consideration, associated with the stringent environmental regulations regarding the industrial use of lead, makes this material a valuable alternative to the commercial catalysts.

Mathematical models are initially developed using a stirred slurry reactor with the aim of predicting the experimental behaviour of the

investigated reacting systems in the typical operating ranges of industrial processes.

The knowledge acquired during these preliminary studies is transferred to the porous structured reactor operated firstly with recirculation of the process liquid and then in fully continuous mode.

The kinetic and adsorption parameters governing the process are estimated in the kinetic regime by means of a numerical optimization procedure. The extension of the model to the mass transfer limited regime allows the estimation of an overall mass transfer coefficient under reacting conditions.

The mathematical model is successfully validated, to confirm its reliability, using the results of additional experimental runs not included in the pool used during the optimization procedure. In this case the model is used to predict the experimental results without any further adjustment of the estimated parameters.

This work enriches the understanding of three-phase selective hydrogenation of alkynes in designed structured reactors and proposes a mathematical model able to predict the performance of the experimental setup.

The model is developed in a step-by-step process and can be used to simulate the intrinsic kinetics and the mass transfer phenomena of this class of reactions in designed structured reactors. These novel reactor concepts are applied for the first time in continuous operation showing potential for Process Intensification.

Riassunto

Le reazioni di idrogenazione catalitica degli alchini in fase eterogenea rivestono notevole importanza nell'industria chimica e farmaceutica soprattutto per la produzione di vitamine.

Queste reazioni sono tradizionalmente condotte attraverso processi discontinui in presenza di catalizzatori al palladio avvelenati con piombo. La tossicità di quest'ultimo elemento limita notevolmente la sostenibilità ambientale di tali processi. L'esigenza di risparmio energetico ha portato negli ultimi anni ad un crescente interesse verso innovazioni tecnologiche per l'intensificazione di processo. Nuove soluzioni reattoristiche potrebbero contribuire in futuro a ridurre i consumi energetici attenuando gli impatti ambientali di tali processi.

Il presente lavoro di tesi contribuisce all'applicazione e alla caratterizzazione di reattori strutturati per l'idrogenazione trifase di alchini in modalità continua e in assenza di solvente.

Il reattore proposto consiste in una struttura metallica porosa con geometria regolare rivestita di uno strato di ossido di zinco ed allumina. Nanoparticelle di palladio sono depositate sulla superficie esterna del catalizzatore. Il suddetto catalizzatore strutturato, privo di piombo, offre prestazioni migliori del classico "catalizzatore di Lindlar" in termini di selettività ed attività e risulta, per questo motivo, una valida alternativa ai catalizzatori commerciali.

L'utilizzo di un reattore discontinuo agitato ha consentito lo sviluppo di modelli matematici capaci di predire il comportamento sperimentale dei sistemi reattivi in oggetto al variare delle condizioni operative negli intervalli tipici dei processi industriali.

Le informazioni acquisite durante questi studi preliminari sono state successivamente estese all'utilizzo di reattori strutturati operati

inizialmente con riciclo del fluido di processo e, successivamente, in modalità continua.

I parametri cinetici tipici delle reazioni di idrogenazione in oggetto sono stati stimati attraverso un'opportuna procedura di ottimizzazione numerica utilizzando i risultati sperimentali ottenuti in regime cinetico. L'estensione del modello matematico al regime diffusivo ha consentito la stima di un coefficiente globale di trasporto di materia.

Per confermarne l'affidabilità, il modello matematico è stato opportunamente validato utilizzando i risultati di ulteriori prove sperimentali non impiegati nella precedente fase di ottimizzazione. Durante questa fase di validazione il modello matematico è stato utilizzato per predire i risultati sperimentali senza alcuna modifica dei parametri cinetici precedentemente stimati.

Il presente lavoro contribuisce alla comprensione dei processi selettivi di idrogenazione trifase degli alchini proponendo un modello matematico utilizzabile per prevedere i risultati dell'apparato sperimentale. Il modello proposto appare in grado di simulare sia le cinetiche intrinseche di questa classe di reazioni, sia i fenomeni di trasporto in reattori strutturati.

Il reattore strutturato in oggetto è stato applicato per la prima volta per condurre reazioni di idrogenazione in modalità continua mostrando il suo potenziale per l'intensificazione di processo.

Table of Contents

Acknowledgements	I
Abstract	V
Riassunto	VII
Nomenclature	XIII
1 Introduction	1
1.1 Hydrogenation in vitamin production	1
1.2 Catalysts	3
1.3 Process intensification	4
1.4 Objectives and outline	6
2 Kinetic modelling of the hydrogenation of 2-methyl-3-butyn-2-ol	9
2.1 Introduction	9
2.2 Experimental	11
2.2.1 Materials	11
2.2.2 Setup and procedure	14
2.2.3 Analysis	14
2.3 Results and discussion	15
2.3.1 Mass transport resistances	15
2.3.2 Gas-Liquid mass transport	17
2.3.3 Liquid-Solid mass transport	20
2.3.4 Hydrogen solubility	23

2.3.5	Kinetic model.....	24
2.3.6	Results	31
2.3.7	Conclusions	40
3	Kinetic modelling of the hydrogenation of dehydroisophytol	41
3.1	Introduction.....	41
3.2	Experimental.....	43
3.2.1	Materials	43
3.2.2	Setup, procedure and analysis.....	44
3.3	Results and discussion	44
3.3.1	Hydrogen solubility.....	44
3.3.2	Mass transport resistances	45
3.3.3	Isophytol hydrogenation.....	47
3.3.4	Dehydroisophytol hydrogenation.....	48
3.3.5	Model validation	62
3.3.6	Effect of quinoline	64
3.3.7	Conclusions	67
4	A Pd/ZnO catalyst for selective hydrogenation of alkynes	69
4.1	Introduction.....	69
4.2	Experimental.....	70
4.2.1	Catalyst preparation	70
4.2.2	Catalyst characterization	71
4.3	Results.....	72
4.3.1	Catalyst characterization	72
4.3.2	Mass transport resistances	78
4.3.3	Hydrogenation of MBY	79
4.3.4	Hydrogenation of DIP	83
4.3.5	Catalyst reuse	86
4.3.6	Conclusions	86
5	Alkyne hydrogenation in a structured reactor	89
5.1	Introduction.....	89

5.2	Experimental.....	92
5.2.1	Structured reactor	92
5.2.2	Experimental setup	95
5.3	Results	98
5.3.1	Reactor characterization	98
5.3.2	Analysis of initial rate data.....	102
5.3.3	Kinetic model.....	103
5.3.4	Mass transfer limited regime.....	109
5.3.5	Model validation	113
5.3.6	Catalyst reuse	115
5.3.7	Conclusions	116
6	Continuous hydrogenation in a structured reactor	117
6.1	Introduction	117
6.2	Experimental.....	119
6.3	Results	121
6.3.1	Reaction rate.....	121
6.3.2	Overall external mass transfer coefficient.....	125
6.3.3	Mass transfer modelling	126
6.3.4	Reactor design.....	132
6.3.5	Conclusions	134
7	Conclusions	137
8	Outlook	141
8.1	Design of the porous structure	141
8.2	Preliminary experiments	143
8.3	Bubble size measurement	145
	Bibliography	147
	List of publications	163
	Curriculum Vitae	167

Nomenclature

Abbreviations

Al	aluminium
Al(NO ₃) ₃	aluminium nitrate
Al ₂ O ₃	aluminium oxide, alumina
Ar	argon
BET	Brunauer–Emmett–Teller adsorption method
C	carbon
cal	calculated
cat	catalyst
C _n H _{2n-2}	alkyne
C _n H _{2n}	alkene
C _n H _{2n+2}	alkane
CaCO ₃	calcium carbonate
CO	carbon monoxide
D	C ₁₀ dimers
DIP	dehydroisophytol
EDX	energy dispersive X-ray analysis
exp	experimental
FIB	focused ion beam
FID	flame ionization detector
G	gas
GC	gas chromatography
H, H ₂	hydrogen
HAADF	high-angle annular dark-field imaging
He	helium
HIP	dihydroisophytol

H ₂ O	water
IP	isophytol
L	liquid
MBA	2-methyl-2-butanol
MBE	2-methyl-3-buten-2-ol
MBY	2-methyl-3-butyn-2-ol
(MBY) ₂ , Y ₂	complex originated in step (2.20)
N ₂	nitrogen
O ₂	oxygen
Pb	lead
Pd	palladium
PdO	palladium oxide
PID	proportional-integral-derivative
P _x	radical
Q	quinoline
Q _x	radical
R _x	radical
S	solid
SE	secondary electrons
SEM	scanning electron microscope
STEM	scanning transmission electron microscope
TEM	transmission electron microscope
TMHQ	trimethylhydroquinone
TOF	turnover frequency
TPO	temperature programmed oxidation
TPR	temperature programmed reduction
Zn	zinc
ZnO	zinc oxide

Latin letters

a	m ⁻¹	specific gas-liquid contact area
a _s	m ⁻¹	specific liquid-solid contact area

C_H^*	mol L^{-1}	hydrogen solubility in the liquid phase
C_i	mol L^{-1}	concentration of species i
C_i^0	mol L^{-1}	initial concentration of species i
D_H	$\text{m}^2 \text{s}^{-1}$	molecular diffusivity of hydrogen in the liquid phase
D_{ax}	$\text{m}^2 \text{s}^{-1}$	axial dispersion
d_{50}	m	median diameter
d_p	m	catalyst particle diameter
d_{pore}	m	pore diameter
d_r	m	reactor diameter
d_I	m	stirrer diameter
E_i	kJ mol^{-1}	activation energy of reaction i
H	bar L mol^{-1}	Henry's constant
H_0	bar L mol^{-1}	pre-exponential factor of Henry's constant
k_{0i}	$\text{mol} (\text{mol}_{\text{Pd}} \text{s})^{-1}$	pre-exponential factor of reaction i
k_i	$\text{mol} (\text{mol}_{\text{Pd}} \text{s})^{-1}$	kinetic constant of reaction i
k_2^*	$\text{L}^2 (\text{mol mol}_{\text{Pd}} \text{s})^{-1}$	kinetic constant of the hydrogenation of IP to HIP
k_{02}^*	$\text{L}^2 (\text{mol mol}_{\text{Pd}} \text{s})^{-1}$	pre-exponential factor of the hydrogenation of IP to HIP
K_{0i}	L mol^{-1}	pre-exponential factor of the equilibrium adsorption constant of species i
K_i	L mol^{-1}	equilibrium adsorption constant of species i
k_L	m s^{-1}	gas-liquid mass-transfer coefficient
$k_{L,a}$	s^{-1}	volumetric gas-liquid mass-transfer coefficient
K_{ov}	s^{-1}	overall external mass-transfer coefficient
k_S	m s^{-1}	liquid-solid mass-transfer coefficient
$k_{S,aS}$	s^{-1}	volumetric liquid-solid mass-transfer coefficient

L	m	structured reactor length
m	g	mass
\dot{m}	kg h ⁻¹	mass flowrate
M	g mol ⁻¹	molecular weight
n	mol	number of moles
n _I	s ⁻¹	stirrer speed
N _p	-	power number
p	bar	pressure
p _H	bar	hydrogen partial pressure
p ⁰	bar	vapor pressure
Q	m ³ s ⁻¹	volumetric flowrate
q _i	-	volumetric fraction of catalyst particles with diameter d _{p,i}
r _i	mol (mol _{Pd} s) ⁻¹	rate of reaction <i>i</i>
r ₀	mol (L s) ⁻¹	observed initial reaction rate
R	kJ (mol K) ⁻¹	universal gas constant
S	-	selectivity
T	K	temperature
t	min, s	time
u	m s ⁻¹	velocity
V _H	cm ³ mol ⁻¹	hydrogen molar volume
V	L, m ³	volume
w	mol L ⁻¹	weighting factor
w _I	m	stirrer blade width
X	-	conversion

Greek letters

β	-	left hand side of Eq. (2.4)
δ	%	palladium dispersion
ΔE	kJ mol ⁻¹	absorption activation energy
ΔH ^{ad} _i	kJ mol ⁻¹	enthalpy of adsorption of species <i>i</i>
ε	-	porosity
γ	L mol ⁻¹	inhibition parameter
λ ₀	-	fractional surface coverage of vacant sites (type *)

λ_{H}	-	fractional surface coverage of hydrogen
φ	mol L ⁻¹	objective function
ρ	kg m ⁻³	density
μ	Pa s	viscosity
Θ	-	vector of the parameters
ϑ_0	-	fractional surface coverage of vacant sites (type \times)
ϑ_i	-	fractional surface coverage of species i
σ	%	standard deviation

Dimensionless numbers

Ca	Carberry number
Pe	Péclet number
Re	Reynolds number
Re _{pore}	pore Reynolds number
Sc	Schmidt number
Sh	Sherwood number

1 Introduction

1.1 Hydrogenation in vitamin production

Selective hydrogenation of alkynes belongs to the most widely studied industrial catalytic processes. The interest for these reactions is justified by their large application in chemical manufactures. Nowadays, more than 10 % of all chemical steps in the synthesis of pharmaceuticals and fine chemicals are catalytic hydrogenations [1][2].

In petrochemical industry, hydrogenations are useful methods to upgrade the quality of the streams from steam reforming and catalytic cracking for production of low-price and large-volume bulk chemicals [3]. Unlike these products, fine chemicals are functionalized high-purity substances produced in small quantities and sold for their high quality rather than for their performance [4].

An important application of selective hydrogenations in pharmaceutical industry is in the production of vitamins [5][6]. Vitamins are necessary for human and animal organisms to perform a large variety of life-giving functions. Nevertheless, they are synthesized only in insufficient amounts in the body [7].

Most vitamins are typically considered fine chemicals with production volumes of about $10^3 - 10^4$ tons per year [8]. Some vitamins can even be considered belonging to the class of bulk chemicals.

With production quantities exceeding $3 \cdot 10^4$ tons per year worldwide, α -tocopherol represents the component with the highest vitamin E activity. Of this quantity, the predominant amount is used for animal feeding and about a quarter goes to human applications [9]. One of the possible schemes of the synthesis of α -tocopherol,

widely applied in industry, is depicted in Figure 1.1, involving multiple semi-hydrogenations.

The production of isophytol, usually representing the side chain building block of α -tocopherol involves a series of C_2 and C_3 chain extension steps starting from 2-methyl-3-butyn-2-ol. This is in turn synthesized from acetone, acetylene and hydrogen [5][6]. The C_2 chain extensions can be carried out by ethynylation followed by semi-hydrogenation, or by adding the vinyl-Grignard reagent [5]. The C_3 extension is preferably obtained by Carroll [10] or Saucy-Marbet [11] reactions. The final product (α -tocopherol) is consequently produced by condensation reaction of trimethylhydroquinone (TMHQ) and isophytol.

The semi-hydrogenations of 2-methyl-3-butyn-2-ol and dehydroisophytol are two of the main steps in this reaction network. Both hydrogenations are “selective”. Aim of these processes is to prevent the further conversion of the semi-hydrogenated product to the corresponding alkane by maximizing the selectivity to the alkene. A general scheme of a selective alkyne hydrogenation is shown in Figure 1.2.

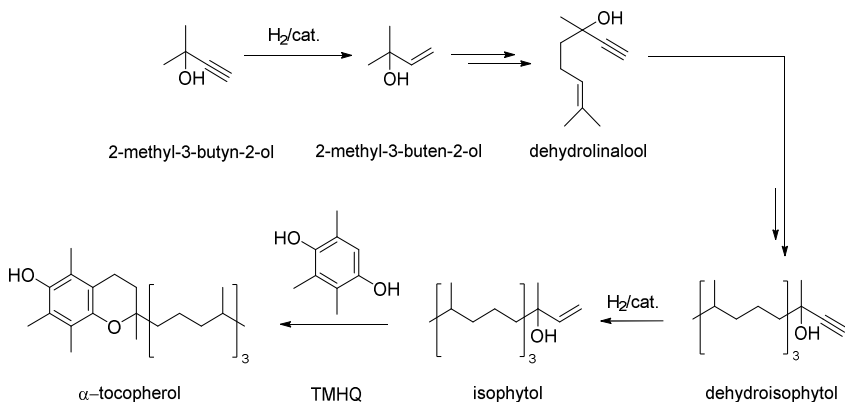


Figure 1.1: Simplified reaction network of the synthesis of α -tocopherol.

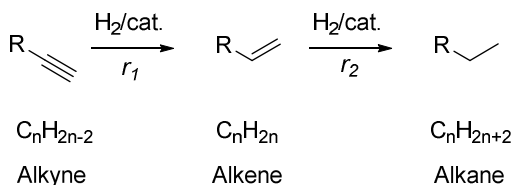


Figure 1.2: General scheme of alkyne hydrogenations.

The intrinsic reaction rate of an alkene hydrogenation is usually faster than the respective one of the corresponding alkyne [12]. Therefore, the high selectivity to the olefinic product can be mainly explained by the thermodynamic of alkyne hydrogenations. A “thermodynamic selectivity” can be defined as the ability of the catalyst to preferentially adsorb the alkyne even in presence of the alkene. If a catalyst exhibits a high thermodynamic selectivity, the adsorption of the alkene on the active surface is hindered. Additionally, the produced alkene, adsorbed on the surface, is replaced by the alkyne during the course of the reaction.

1.2 Catalysts

The absolute majority of hydrogenation processes are conducted using heterogeneous catalysts [13]. Heterogeneous catalysts for hydrogenations are typically supported, namely based on two solid phases: an inert phase, generally in the form of fine particles and an active phase constituted by noble metals or alloys. The active metal is generally deposited on the support in the form of nanoparticles (diameter in the range 1 – 10 nm)[2]. In case of porous materials used as support, the metal penetrates the micropores increasing the specific surface area of the catalyst. The most important properties required for a heterogeneous catalyst for alkyne hydrogenations are high activity and selectivity, high filtration rate and recycle capability. Activity and selectivity are directly dependent on the choice of the metal. This can strongly influence adsorption/desorption strength of

reactants and products as well as the intrinsic rate of the chemical transformation [2].

One of the most commonly used catalysts for this class of reactions is the Lindlar catalyst, a 5 wt % Pd/CaCO₃ powder, modified by the addition of lead to improve alkene selectivity [14][15].

However, the use of the toxic lead as modifier has encouraged the search for more environmental friendly materials in accordance to the principles of Green Chemistry [16].

Lindlar catalyst can be directly used for hydrogenation or further modified by nitrogen-based organic compounds (process modifiers) for selectivity enhancement. The higher selectivity is in this case due to a reduced rate of alkene hydrogenation, while semi-hydrogenation of the triple bond is largely unaffected [17]. However, the incorporation of these compounds requires further process steps, such as separation, resulting in additional costs.

Alternative approaches to enhance the hydrogenation selectivity are mostly directed on catalyst modification. It is reported, for example, that the catalyst support can interact with the active phase affecting the catalyst performance [18].

ZnO, in particular, is considered a good alternative to CaCO₃ because zinc is known to act as a promoter in the Pd-based catalysts. The electron donating effect of zinc results in a higher electron density of palladium. The selectivity of the process is enhanced, as a consequence, due to the reduced alkene adsorption.

1.3 Process intensification

The price pressure on vitamins and intermediate products for fine chemical production has significantly increased in recent years. Therefore, pharmaceutical and fine chemical companies have directed their R&D towards the necessity of improving energy and material efficiency, avoiding the use of toxic reagents, improving catalysts performances and achieving sustainable processes [19]. These goals can be summarized under the term “Process Intensification”, defined as the strategy for making reductions in the size of a chemical plant

reaching a certain production objective [20]. These size reductions can be intended as shrinking the size of individual equipment or reducing the number of unit operations required in a process.

The original definition of Process Intensification was extended by Stankiewicz and Moulijn and referred to any engineering development leading to a substantially smaller, cleaner and more energy efficient technology [21].

One of the major topics in the field of Process Intensification is the switch from batch to continuous processes. This has a great relevance in the vitamin industry, where conventional manufacturing is generally accomplished using batch processing [22][23]. Discontinuous operations afford an intrinsic flexibility: batch reactors can be operated over relatively short periods of time, repeatedly, making them convenient for manufacturing a wide variety of products.

However, despite these advantages, they are highly inefficient leading to long cycle times, energy waste and significant catalyst handling issues [24]. For the specific case of hydrogenations, developing safe batch processes is also challenging since these reactions are generally highly exothermic. A commonly recognized problem is the inability of batch reactors to efficiently remove the heat produced during the reaction. This can result, in the worst case, in reactions running out of control leading to elevated temperatures [25].

Continuous processing, on the other hand, offers several advantages such as:

- elimination of dead times and intermediate storages
- straightforward scale-up
- high throughput
- intrinsic safety due to the small reacting volumes

This contribution focuses on the use of designed structured reactors for alkyne hydrogenation. These devices, combining static mixing elements and catalyst carrier functions, consist on metal porous structures coated with a catalytic layer [26][27][28].

Catalytic conversion and catalyst separation are conventionally carried out in separate pieces of equipment. The structured reactors combine these functions in single units offering an elegant form of Process Intensification [29][30].

In contrast to conventional packed-bed reactors, structured reactors are characterized by large void fractions allowing chemical processes to be conducted with high flowrates and low pressure drops [30]. Random packed-bed reactors, on the other hand, can cause maldistribution of reactants and products due to channeling effects, which in turns leads to non-uniform flow and concentration profiles and, in case of exothermic reactions, to the formation of hot spots [27][28]. The unavoidable heat accumulation due to the poor heat transfer properties can dramatically affect the selectivity of the process.

A similar analysis holds for slurry reactors. The mixing intensity in a mechanically stirred-tank reactor is highly non-uniform and only a relatively small annulus around the tip of the stirrer can often be considered as an effective reaction space [29].

1.4 Objectives and outline

The work presented in this thesis focuses on the characterization of kinetics and mass transfer phenomena of selective hydrogenation of alkynes in structured reactors. Core of the work is the application of a designed structured reactor in the hydrogenation of 2-methyl-3-butyn-2-ol in flow in prospect of Process Intensification.

This thesis is structured as follows:

Chapter 2 and 3 focus on the hydrogenations of 2-methyl-3-butyn-2-ol and of dehydroisophytol, two of the main hydrogenation steps for the industrial production of vitamin E. These hydrogenations, chosen as model reactions, are studied in a slurry stirred reactor over a commercial Lindlar catalyst.

The main goal of these chapters is the development of general kinetic models able to predict the kinetic behaviour of these reacting systems in the typical operating ranges of industrial reactors. Despite

their extensive use in the fine chemical industry, a detailed kinetic characterization of these processes over a wide range of operating conditions has not been proposed in literature.

Chapter 4 presents the chemical characterization of a lead-free non-traditional catalyst based on Pd deposited on a metal support coated with a layer of ZnO/Al₂O₃. The performance of this catalyst in terms of selectivity is compared with Lindlar catalyst under the same operating conditions.

The metal support makes this catalyst suitable for its direct application in a structured reactor in prospect of Process Intensification.

Chapter 5 presents a novel concept of structured reactor consisting in a metal porous structure with regular geometry internally coated with the previously introduced Pd/ZnO/Al₂O₃ catalyst. The reactor is chemically characterized and tested in the hydrogenation of 2-methyl-3-butyn-2-ol with recirculation of the process liquid and continuous supply of hydrogen (semi-batch operation).

The observed hydrogenation rate is found strongly dependent on the hydrogen flowrate. The mathematical model, previously developed in Chapter 2, is applied to the kinetic regime in order to estimate the kinetic and adsorption parameters governing the process. The extension of the model to the mass transfer limited regime allows the estimation of an overall mass transfer coefficient K_{ov} under reacting conditions.

The structured reactor operated in semi-batch mode can be considered a promising device to combine catalyst separation and chemical conversion in a single piece of equipment.

Chapter 6 presents the operation of the structured reactor in a continuous plant for the hydrogenation of 2-methyl-3-butyn-2-ol. The reaction appears to be mass transfer limited with estimated K_{ov} lower than 1.2 s⁻¹. A predictive correlation is proposed in order to estimate K_{ov} for varying operating temperatures, pressures, gas and liquid flowrates.

Overall, a detailed mathematical model is developed and validated in order to simulate both intrinsic kinetics and mass transfer phenomena of the continuous hydrogenation of 2-methyl-3-butyn-2-ol in designed structured reactors. These devices are found to be a viable

alternative to transform batch processes with considerable industrial relevance into sustainable and more efficient continuous processes.

Final aim of the thesis is to propose a practical tool that can be used to design a pilot plant for the continuous hydrogenation of 2-methyl-3-butyn-2-ol in flow over a lead-free catalyst. The mathematical model allows to predict conversion, selectivity and reaction rate of the reacting system and, therefore, it can be used to optimize the operating conditions of the process.

Each chapter of this thesis is written based on one or more separate publications and can be read independently.

2 Kinetic modelling of the hydrogenation of 2-methyl-3-butyn-2-ol

2.1 Introduction

The selective semi-hydrogenation of 2-methyl-3-butyn-2-ol (MBY) is a key reaction in fine chemicals production [19]. It is a classic example of a catalytic three-phase process following a consecutive reaction network. The selectivity of this reaction system concerns the possibility of hydrogenating MBY to 2-methyl-3-buten-2-ol (MBE) while preventing a further hydrogenation to 2-methyl-2-butanol (MBA).

The partially hydrogenated product MBE has a great importance in the industrial synthesis of vitamins A and E and is also a key intermediate in the manufacture of aroma compounds [31]. The reaction network assumed for the hydrogenation of MBY is depicted in Figure 2.1.

Due to its industrial relevance, the hydrogenation of MBY has been investigated over the past years by several researchers [32][33][34].

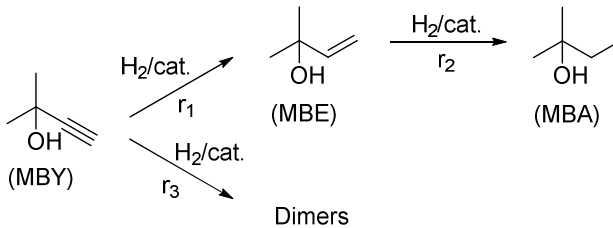


Figure 2.1: Reaction network of MBY hydrogenation.

Bruehwiler *et al.* [33] studied the kinetic of hydrogenation of MBY over a modified 5 wt % Pd/CaCO₃ catalyst at 333 K and 2.8 bar, proposing rate equations based on the Langmuir-Hinshelwood type rate mechanism with competitive adsorption of the reactants/products on the catalyst surface. The aforementioned model assumes a first order of reaction with respect to hydrogen and is simplified by the use of estimated apparent kinetic parameters, lumping together kinetic and adsorption constants, and hydrogen concentrations.

The same mechanism was used by Crespo-Quesada *et al.* [32] to describe the hydrogenation of MBY over a Pd/ZnO structured catalyst. In that work, an estimate of the activation energy is proposed, for the main hydrogenation (MBY to MBE), according to a simplification of the reaction rate expression in a power law rate.

A different mechanism was developed by Rebrov *et al.* [34] to describe the kinetic of MBY hydrogenation over Pd-based catalysts at 333 K and 5.0 bar. The proposed reaction rate equations suggest that hydrogen reacts with the liquid phase directly from the gas phase, without adsorption on the catalyst surface, resulting in a typical Eley-Rideal approach.

Despite its extensive use, a detailed characterization of the kinetic parameters governing the hydrogenation process of MBY has not been proposed in literature. Thus, all the preceding results are related to specific temperatures and pressures and have not been proven to predict the evolution of the system over a wide range of operating conditions.

In this chapter a general kinetic model is developed and validated in order to simulate the system behaviour under varying temperatures (313 – 353 K), pressures (3.0 – 10.0 bar) and catalyst loadings (0.075 – 0.175 wt %). The experimental runs were designed in order to investigate the typical operating ranges of industrial reactors.

A kinetic model based on the non-competitive adsorption between hydrogen and organics has been successfully applied for the first time to the hydrogenation of MBY. The final purpose was to provide reliable kinetic expressions and a detailed set of adsorption and kinetic parameters (activation energies, enthalpies of adsorption and pre-exponential factors) for each of the reactions involved in the process. The proposed model, reliably validated, is able to predict the kinetic behaviour of the system knowing its temperature, its pressure and the loaded amount of catalyst.

2.2 Experimental

2.2.1 Materials

MBY (> 98 %) was supplied by DSM Nutritional Products. MBE (≥ 98 %) and MBA (≥ 99 %) for analytical purposes were purchased from Sigma-Aldrich. The physical properties of MBY are listed in Table 2.1.

Hydrogen (99.995 %) and nitrogen (99.995 %), for inertization purposes, were supplied by Pangas.

The hydrogenation experiments were conducted using a commercial Lindlar catalyst (5 wt % Pd/CaCO₃ modified with Pb) purchased from Sigma-Aldrich. All the reagents and the catalyst were used as received. A fresh sample of catalyst was used for each hydrogenation experiment. Some of the physical characteristics of the catalyst are listed in Table 2.2. An SEM microphotograph of a catalyst particle is shown in Figure 2.2. The external surface of CaCO₃ support appears to be decorated by large metal clusters (size up to ~ 1 μm) containing Pd and Pb according to EDX analysis. The metal loadings of Pd and Pb are listed in Table 2.2.

Table 2.1: Physical properties of MBY.

T	Density, ρ_L	Viscosity, $10^3 \mu_L$	Vapor pressure, p^0
[K]	[kg m ⁻³]	[Pa s]	[bar]
313	843	1.79	0.05
333	821	1.04	0.16
343	809	0.82	0.25
353	798	0.66	0.39

Table 2.2: Lindlar catalyst characteristics.

Property	Value
	< 60 for 100%
	< 43 for 83 %
Cumulative particles	< 36 for 72 %
size distribution	< 22 for 50 %
[μm]	< 9 for 30 %
	< 4 for 18 %
	< 1 for 6 %
d_{50}	22
[μm]	
BET surface area	1.2
[m ² g ⁻¹]	
Density, ρ_S	2710 [35]
[kg m ⁻³]	
Pd loading	5.0
[wt %]	
Pb loading	1.2
[wt %]	

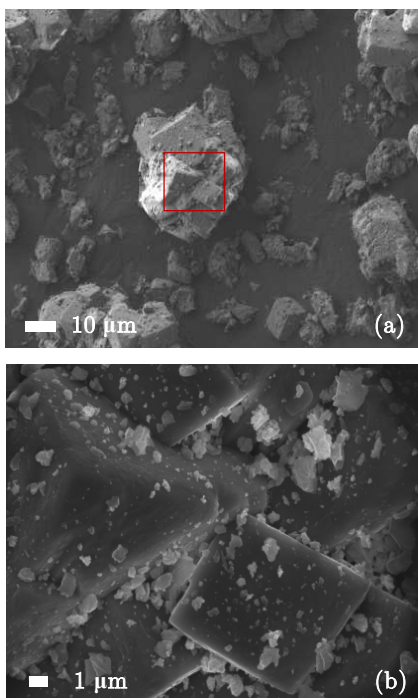


Figure 2.2: (a) SEM microphotograph of a Lindlar catalyst particle. Detector: SE2, voltage 2 kV. (b) Magnified image of the selected area (red box) in (a) Detector: in-lens, voltage: 12 kV.

2.2.2 Setup and procedure

All the experiments were performed charging 200 g of the initial mixture in a 400 mL batch autoclave (Premex Reactor AG, Lengnau, Switzerland) made of titanium with an inner diameter of 65 mm and a height of 118 mm. The reactor was equipped with a system of four equidistant baffles with a width of 12 mm and a thickness of 2.5 mm. A 4-blade gas-entrainment stirrer of diameter $d_I = 38$ mm and width $w_I = 12$ mm allowed the gas in the head space to be dispersed into the liquid.

The rotational speed of the impeller was controlled by means of an electronic frequency controller. The reactor was equipped with an electrical heating jacket. Isothermal conditions during experiments were ensured by a water cooling control system. The temperature of the liquid phase was measured with a thermocouple immersed in the reaction mixture, controlled, and maintained constant within ± 0.2 K during the experiments using a water cooling control system.

Before heating, the headspace of the reactor was flushed three times with nitrogen to ensure an inert atmosphere and remove any dissolved oxygen. In the typical experiment for the kinetic study, the reactor was heated to the operating temperature under atmospheric nitrogen pressure and low stirring (3 Hz). The system was then flushed with pure hydrogen and pressurized to the required level. During the reaction the pressure was maintained constant by supplying hydrogen from an external cylinder (all the pressure values mentioned in this work are given as absolute). The reactor was equipped with digital pressure transducer with a precision of ± 0.1 bar.

The reaction time was initialized to zero as soon as the liquid phase with suspended catalyst came in contact with hydrogen and the stirrer was switched on at its maximum rate (20 Hz).

Hydrogenation experiments were carried out in a temperature range of 333 – 353 K and in a pressure range of 3.0 – 10.0 bar.

2.2.3 Analysis

Liquid samples were withdrawn at defined intervals of time through a valve connected to the reactor and analysed using a Bruker

GC-450 gas-chromatograph with a flame ionization detector (FID). The GC was equipped with a *VF-Wax ms* separation column (25 m \times 0.25 mm, coating thickness 0.25 μm). Injector and flame ionization detector temperatures were 523 K and 493 K respectively. The oven temperature was increased at 20 K min^{-1} from 353 to 473 K.

For each analysis a sample of approximately 1.5 mL of liquid was subtracted so that the total uptake for each experiment never exceeded 10 % of the initial liquid volume. No significant differences were observed between test experiments conducted by sampling 10 and 5 % of the initial liquid quantity. Hence, the liquid-to-catalyst ratio was considered to remain constant during the sampling.

The densities of the reacting solutions during the experimental runs were assumed constant and equal to that of MBY. The average molecular weight of the dimers formed during the hydrogenation of MBY was assumed to be 160 g mol^{-1} [32]. The concentration of dimers was indirectly estimated from the C-moles loss during the process.

Hydrogenation tests under two different sets of experimental conditions were repeated three times to ensure their reproducibility.

The results, in terms of concentration of the species, were found to be reproducible within 7 %.

2.3 Results and discussion

2.3.1 Mass transport resistances

Mass transfer is a critical process affecting the apparent reaction rate of a three-phase hydrogenation. Figure 2.3 shows a schematic of the concentration profile of hydrogen in a multiphase catalytic reactor. Hydrogen diffuses from the gas phase through the liquid phase in order to reach the catalyst active sites and react. In a general case the hydrogen mass transfer process can be described by the following steps:

- (i) Transfer of hydrogen from the gas phase bulk to the gas-side film.
- (ii) Transfer of hydrogen from the gas-side film to the gas-liquid interface.
- (iii) Transfer of hydrogen from the gas-liquid interface to the liquid-side film.
- (iv) Diffusion of hydrogen through the liquid bulk to the liquid film surrounding the surface of the catalyst.
- (v) Diffusion of hydrogen through the liquid film to the surface of the catalyst.
- (vi) Diffusion of hydrogen inside the pores of the catalyst to the active sites.

Steps (i) and (ii) can be neglected assuming that the gas phase is constituted by pure hydrogen. Step (vi) is obviously relevant only in case of porous catalysts. The products of reaction are assumed to diffuse back from the surface of the catalyst to the liquid phase. At high conversions, the liquid-solid mass transfer of the liquid reactant may also influence the observed reaction rate.

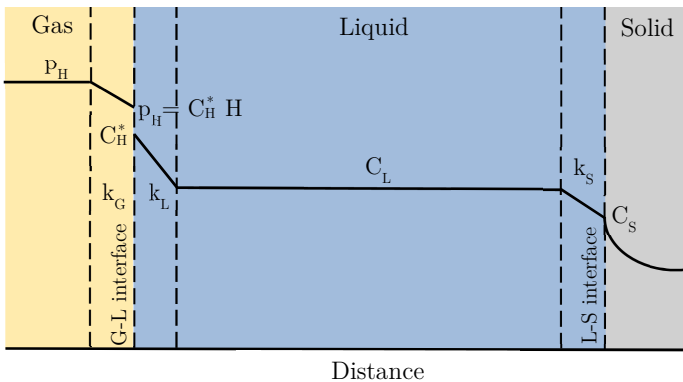


Figure 2.3: Sketch showing the hydrogen concentration profile for mass transfer in a gas-liquid system with reaction on the surface of a catalyst.

2.3.2 Gas-Liquid mass transport

The volumetric gas-liquid (G-L) mass transfer coefficients $k_L a$ for hydrogen in MBY were estimated in the absence of the catalyst, by the gas absorption method [36][37].

The operating procedure consists of the following steps:

- (i) The liquid is degassed at low stirring at known hydrogen pressure p_{H0} and the desired temperature T is reached.
- (ii) The reactor is pressurized with the gas which is to be absorbed to the desired pressure p_{H1} without stirring.
- (iii) Agitation is started (20 Hz) and the pressure decay is followed as function of time until the equilibrium pressure p_{H2} is reached.

The differential mass balance for hydrogen in the liquid phase gives:

$$\frac{dn_L}{dt} = V_L \cdot k_L a \cdot (C_H^* - C_L) \quad (2.1)$$

Where n_L indicates the moles of hydrogen dissolved in the liquid phase.

The effect of pressure on the solubility can be described by Henry's law as:

$$C_H^* = \frac{p_H}{H} \quad (2.2)$$

Henry's constant H was assumed to be independent of the pressure of the system [38]. Hydrogen partial pressure p_H was obtained as difference between the absolute pressure of the system and the vapour pressure of MBY reported in Table 2.1.

A differential form of the ideal gas law is:

$$\frac{dp_H}{dt} = -\frac{RT}{V_G} \frac{dn_L}{dt} \quad (2.3)$$

The integration of Eq. (2.1) between $t = 0$ ($p_H = p_{H1}$) and t ($p_H = p_H(t)$) gives the following equation:

$$\frac{p_{H2} - p_{H0}}{p_{H1} - p_{H0}} \ln \left(\frac{p_{H1} - p_{H2}}{p_H(t) - p_{H2}} \right) = k_L a \cdot t \quad (2.4)$$

More details about the derivation of this equation can be found in the above-mentioned references [36][37].

The left hand side of Eq. (2.4) ($\beta(t)$) can be plotted versus t to calculate $k_L a$ as slope of the line depicted in the exemplary Figure 2.4.

Some of the experiments were conducted under inert atmosphere (N_2) in the presence and absence of the catalyst since, as reported in literature, $k_L a$ can be affected by the presence of solid particles [36][39].

The values for $k_L a$ were assumed not to change with the concentration of MBY during the reaction due to the similar physical properties between the species involved in the system.

Table 2.3 shows the obtained results; it is concluded that low concentrations of catalyst do not affect $k_L a$. On the other hand, increasing the temperature considerably increases $k_L a$ values. At high temperature the liquid viscosity and surface tension decrease, leading to a decrease of the average bubble size and accordingly, to an increase of the specific G-L contact area a . Furthermore, the increase of diffusivity at high temperatures implies a direct increase of the G-L mass transfer coefficient k_L .

It is usually accepted in literature that the pressure effect on $k_L a$ is small or negligible [40][41]. For this reason $k_L a$ was considered in this work independent of pressure in the investigated range between 3.0 and 10.0 bar.

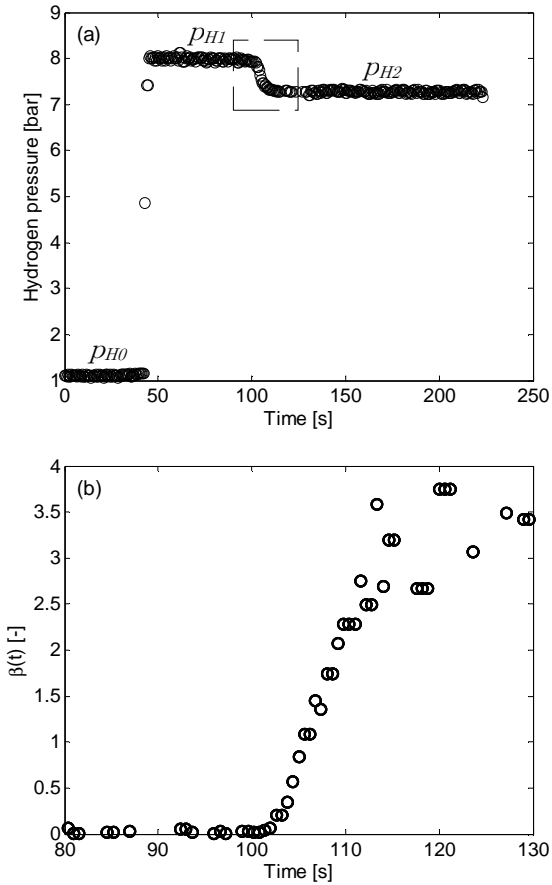


Figure 2.4: (a) Exemplary pressure profile during the batch hydrogen absorption in MBY. (b) Left hand side of Eq. (2.4) versus time referring to the rectangular box in (a).

Table 2.3: G-L mass transfer coefficients for hydrogen and nitrogen in MBY in the presence and absence of the catalyst.

Gas	T [K]	Catalyst loading [wt %]	k_{La} [s ⁻¹]
H ₂	313	0	0.36 ± 0.01
H ₂	333	0	0.43 ± 0.02
H ₂	343	0	0.47 ± 0.02
H ₂	353	0	0.51 ± 0.01
N ₂	353	0	0.32 ± 0.02
N ₂	353	0.075	0.30 ± 0.02
N ₂	353	0.125	0.33 ± 0.01
N ₂	353	0.175	0.34 ± 0.02

2.3.3 Liquid-Solid mass transport

To estimate the limitations set by external liquid-solid (L-S) mass transfer, the Sherwood-Frössling correlation [33][42] was used:

$$Sh_i = 2 + 0.4Re_i^{1/4}Sc^{1/3} \quad (2.5)$$

with:

$$Sh_i = \frac{k_{S,i} \cdot d_{p,i}}{D_H} \quad (2.6)$$

$$Re_i = \frac{N_p \cdot d_i^5 \cdot n_i^3 \cdot d_{p,i}^4 \cdot \rho_L^3}{V_L \cdot \mu_L^3} \quad (2.7)$$

$$Sc = \frac{\mu_L}{\rho_L \cdot D_H} \quad (2.8)$$

The subscript i is referred to the catalyst particle diameter $d_{p,i}$ according to the cumulative distribution function of particle sizes presented in Table 2.2. The power number N_p was assumed to be 5.5 for a 4-blade stirrer with $w_l/d_i \approx 0.3$ [43]. All the properties of the liquid phase were considered equal to those of pure MBY.

The molecular diffusivity of hydrogen in the liquid phase D_H was estimated from the Wilke-Chang correlation for unassociated solvents, usually accurate to within 10 – 15 % [44].

$$D_H = 7.4 \cdot 10^{-15} \frac{T \sqrt{M_L}}{\mu_L \cdot V_H^{0.6}} \quad (2.9)$$

with the hydrogen molar volume V_H equal to $14.3 \text{ cm}^3 \text{ mol}^{-1}$ [44].

Based on the particle size distribution of the catalyst powder, the L-S mass transfer coefficients were calculated as follows:

$$k_S a_S = \sum_i^n q_i k_{S,i} a_{S,i} \quad (2.10)$$

where q_i is the volumetric fraction of catalyst particles with diameter $d_{p,i}$.

Assuming that the catalyst particles can be approximated as spherical, the specific L-S interface area was estimated as:

$$a_{S,i} = \frac{6}{d_{p,i}} \frac{m_S \rho_L}{m_L \rho_S} \quad (2.11)$$

At high conversion, the observed reaction rate may also be influenced by L-S mass transfer of MBY. The L-S mass transfer coefficient for MBY in the liquid phase was estimated considering a diffusivity of $1.47 \cdot 10^{-9} \text{ m}^2 \text{ s}^{-1}$ at the reference temperature $T_{ref} = 333 \text{ K}$ [33]. The Stokes-Einstein equation allowed to estimate the diffusivity of MBY at other temperatures:

$$D_Y(T) \frac{\mu_L(T)}{T} = D_Y(T_{ref}) \frac{\mu_L(T_{ref})}{T_{ref}} \quad (2.12)$$

At the most severe reaction temperature of 353 K a L-S mass transfer coefficient of 2.10 s^{-1} was calculated for MBY in the liquid mixture.

The calcium carbonate catalyst support is non-porous [45] and no large aggregates of particles were detected by laser diffraction (maximum diameter 60 μm). For this reason, the catalyst effectiveness factor was considered to be equal to one and the internal L-S mass transfer neglected. The results in Table 2.3 and Table 2.4 show that the calculated L-S mass transfer coefficients k_{saS} are substantially higher than the correspondent G-L k_{La} . Therefore, the L-S mass transfer resistance was neglected during this phase.

Table 2.4: Overview of the hydrogenation experiments on pure MBY used for the calculation of the kinetic parameters with the corresponding estimated L-S mass transfer coefficients

Run	T [K]	p [bar]	Catalyst loading [wt %]	k_{saS} [s^{-1}]
1	333	9.0	0.125	2.67
2	353	9.0	0.125	4.33
3	333	9.0	0.175	3.74
4	333	9.0	0.075	1.60
5	333	7.0	0.125	2.67
6	313	9.0	0.125	1.48
7	333	10.0	0.125	2.67
8	333	4.0	0.125	2.67
9	353	10.0	0.125	4.33
10	353	3.0	0.125	4.33
11	313	7.0	0.125	1.48
12	353	9.0	0.175	6.33
13	333	6.0	0.125	2.67
14	353	9.0	0.075	2.71

2.3.4 Hydrogen solubility

The solubility of hydrogen in MBY was experimentally estimated between 313 and 353 K using the physical absorption method introduced in Section 2.3.2.

The temperature dependence of Henry's constant is shown in Figure 2.5. The linear trend suggests to model the effect of temperature on H by an Arrhenius type equation following the approach proposed by Fillion and Morsi [46]. Thus, hydrogen solubility in MBY was theoretically expressed as:

$$C_H^* = \frac{p_H}{H_0 \cdot \exp\left(-\frac{\Delta E}{RT}\right)} \quad (2.13)$$

Estimated values for the pre-exponential factor and the apparent activation energy of adsorption are $H_0 = 33.8 \text{ bar L mol}^{-1}$ and $\Delta E = -6.81 \text{ kJ mol}^{-1}$. These results were obtained with linear regression of the experimental data depicted in Figure 2.5 ($r^2 = 99.3 \%$).

At 333 K, Henry's constant is estimated to be $396 \text{ bar L mol}^{-1}$. This value is close to those reported in literature at the same temperature for similar systems: $357 \text{ bar L mol}^{-1}$ for hydrogen in alkynes [47] or $440 \text{ bar L mol}^{-1}$ for hydrogen in MBY [33].

Values ranging between $6.0 \cdot 10^{-3}$ and $2.8 \cdot 10^{-2} \text{ mol L}^{-1}$ were obtained for the hydrogen solubility in MBY over the ranges of investigated temperatures and pressures.

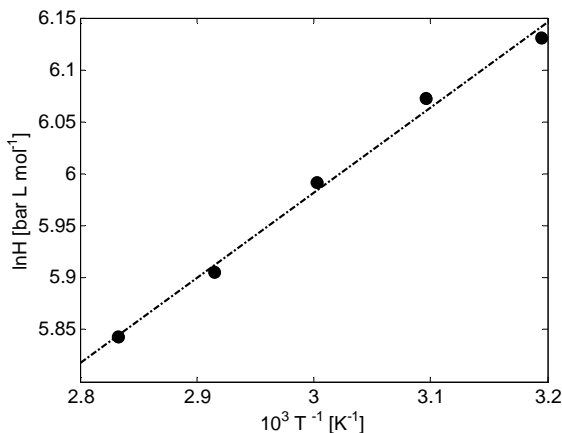


Figure 2.5: Effect of temperature on Henry's constant of hydrogen in MBY.

2.3.5 Kinetic model

The great importance of selective hydrogenation of alkynes has addressed considerable efforts in developing mathematical models able to predict and simulate the experimental results. Kinetic studies are extremely important in the field of catalytic processes representing a bridge between theory and practice of catalysis [48].

Aim of a kinetic model is providing a mathematical description of the hydrogenation process describing the behaviour of the system under different operating conditions.

Kiperman highlights the difference between kinetic model and reaction mechanism [49]. The first is a quantitative description of the rate of a process. The latter is the qualitative characterization of the intrinsic characteristics of a reaction on a certain catalyst. Both concepts are strongly related. Even if a mathematical model is always built according to a specific reaction mechanism it is also true that

the results of a kinetic modelling can be decisive to elucidate the right mechanism governing a process.

Mathematical models of catalytic reactions represent the basis for designing industrial reactors and improving existing technologies. Finding a mechanism able to represent what occurs in reality allows to safely extrapolate the results obtainable under different operating conditions.

In several cases elementary power laws can be used to fit catalytic conversion data. More complex kinetic mechanisms can be postulated by decomposing the hydrogenation process into different elementary steps. In this case the reaction rates of alkyne hydrogenations are usually expressed as:

$$r = \frac{(\textit{kinetic term})(\textit{driving force})}{(\textit{adsorption term})} \quad (2.14)$$

In general the reaction is supposed to take place on the active sites of the surface of the catalyst. This contribution focuses on the most used kinetic mechanism to describe the selective hydrogenation of triple-bond: the Langmuir-Hinshelwood mechanism. This can be characterized by competitive or non-competitive adsorption of hydrogen and alkyne and by dissociative or associative adsorption of hydrogen.

The approach followed in this thesis is to propose a sequence of elementary steps consistent with the stoichiometry of the reaction. A rate expression is derived using the steady-state approximation together with other assumptions (e.g. rate-determining step) and compared to the experimental data. The sequence of elementary steps is considered plausible if the functional dependence is described with satisfactory approximation by the proposed rate expression.

The reaction network proposed for the hydrogenation of MBY is summarized below:





Reaction r_3 involves the formation of dimeric C_{10} products, as result of the reaction between two molecules of MBY adsorbed on the catalyst surface and hydrogen.

According to various authors, the formation of the alkane takes place not only in a consecutive way, but also in parallel by direct hydrogenation of MBY to MBA [32][33][34]. However, in our experiments, only negligible amounts of MBA were detected before the complete hydrogenation of MBY, resulting in a relatively high selectivity of the process to MBE. Therefore, in order to simplify the network, it was decided to lay the consumption of MBY only at its partial hydrogenation to MBE and at its dimerization. The same approach was followed by Nikoshvili *et al.* [50].

Figure 2.6 shows the effect of hydrogen partial pressure on the initial hydrogenation rate of MBY in a range of 313 – 353 K. These values were obtained from experiments carried out with pure MBY and the same catalyst loading at different operating conditions. The initial rate of MBY hydrogenation appears to vary linearly with hydrogen partial pressure for the three investigated temperatures. This analysis indicates that the rate of reaction is first-order with respect to hydrogen in the investigated range of conditions.

One of the relevant catalytic mechanisms for the hydrogenation of MBY over Pd was posed by Crespo-Quesada *et al.* [32], assuming competitive adsorption of the reactants on one type of active site. However, we adopted in this work the simplest Langmuir-Hinshelwood model for a catalysed reaction between large and small molecules, namely non-competitive adsorption of hydrogen and organics. This hypothesis, usually accepted in literature for both hydrogenation of alkynes [51] and alkenes [52], is justified considering that the studied solvent-free system was highly concentrated in unsaturated organic species while the pressure range was limited from 3.0 to 10.0 bar. For these reasons, a high catalyst surface coverage is

expected for MBY while the corresponding one for hydrogen, is lower and not supposed to dramatically change over the pressure range.

Dissociative adsorption of hydrogen was assumed to occur on sites represented by (*), different from those involved in the adsorption of organic species, represented by (\times).

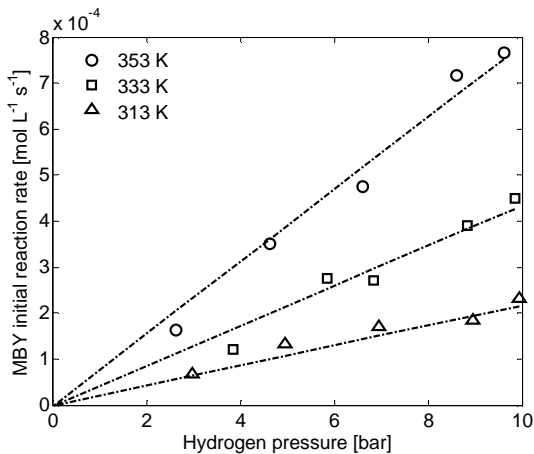
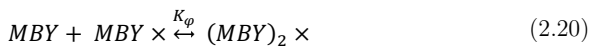
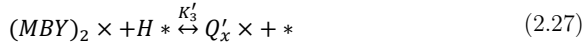
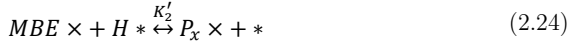
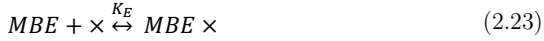
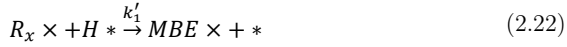


Figure 2.6: Effect of hydrogen pressure on the initial rate of MBY hydrogenation. Catalyst loading: 0.125 wt %.

The elementary steps proposed to describe the complete hydrogenation mechanism of MBY are listed below. A similar mechanism was assumed by Alves *et al.* [53] for the liquid-phase hydrogenation of 1-butyne over a Pd-based catalyst.





Steps (2.18), (2.19), (2.23), (2.26) and (2.31) describe the absorption/desorption of MBY, hydrogen and of the reaction products on the catalyst surface. All the adsorption and desorption steps were assumed to be fast enough to reach quasi-equilibria. The complex $(MBY)_2$ is originated from step (2.20) when two molecules of MBY adsorb on one active site. The addition of 4 hydrogen atoms to this complex (steps (2.27)-(2.30)) leads to the formation of a dimer.

It is accepted that the formation of MBE involves two consecutive elementary steps by dissociative adsorption of hydrogen [32]. A first hydrogen atom is added to the adsorbed molecule of MBY in the step (2.21). The semi-hydrogenated radical R_x reacts with an additional hydrogen atom in the step (2.22) to produce an adsorbed molecule of MBE.

The same H-addition steps are assumed to describe the over hydrogenation of MBE to MBA and the production of dimers.

The observed dependency of MBY hydrogenation rate on hydrogen pressure (Figure 2.6) suggests to consider the first hydrogen addition quasi-equilibrated and the second non-reversible. The same approach was followed for the production of dimers considering reversible the first three hydrogen atom additions. Similar hypothesis have been assumed in literature for the hydrogenation of dehydroisophytol [54], MBY [33], *n*-butene [52], 1-butyne [53], 1-hexyne [55]. During the hydrogenation of carbon-carbon multiple bonds, the last hydrogen addition is usually considered non-reversible because the resulting molecule desorbs from the surface of the catalyst [56].

Under this assumption, the rate equation for the hydrogenation of MBY to MBE can be expressed as:

$$r_1 = k'_1 \vartheta_{R_x} \lambda_H \quad (2.32)$$

The fractional surface coverages for the active sites (\times) and ($*$) (respectively ϑ_i and λ_i) can be obtained from the combination of the two mass balances:

$$\vartheta_Y + \vartheta_E + \vartheta_A + \vartheta_D + \vartheta_{Y_2} + \vartheta_0 = 1 \quad (2.33)$$

$$\lambda_H + \lambda_0 = 1 \quad (2.34)$$

with the expressions of the equilibrium constants of the reversible reaction steps. The symbols ϑ_0 and λ_0 indicate the fractional surface coverages of vacant sites. Low coverages for the intermediate species R_x have been assumed in the mass balance for the catalyst active sites.

Combining Eq. (2.33) and (2.34) with the expressions of the equilibrium constants, it results:

$$\lambda_H = \frac{\sqrt{K_H C_H}}{1 + \sqrt{K_H C_H}} \quad (2.35)$$

$$\vartheta_{R_x} = \frac{K_1' K_Y C_Y \sqrt{K_H C_H}}{1 + K_Y C_Y (1 + K_\varphi C_Y) + K_E C_E + K_A C_A + K_D C_D} \quad (2.36)$$

The following expression of the reaction rate of MBY hydrogenation is finally deduced:

$$r_1 = k_1 \frac{K_Y C_Y}{1 + K_Y C_Y (1 + K_\varphi C_Y) + K_E C_E + K_A C_A + K_D C_D} \cdot \frac{K_H C_H}{1 + \sqrt{K_H C_H}} \quad (2.37)$$

where $k_I = k_I' K_I'$ is the apparent kinetic constant of the hydrogenation of MBY to MBE.

The concentration of dimers detected during all the experiments was substantially low compared to the concentrations of the other species involved in the system. Furthermore, the adsorption constant of MBA is small, due to the weak adsorption of the single bond on the catalyst surface. For this reasons, the terms $K_D C_D$ and $K_A C_A$ were neglected in Eq. (2.37). The weak hydrogen adsorption on the Pd surface [55] and the low hydrogen concentrations allow to neglect the hydrogen inhibition contribution too. The hydrogen inhibition term would become important only in case of high pressures leading to higher values of hydrogen solubility, according to Eq. (2.13).

Under these assumptions, Eq. (2.37) can be simplified to:

$$r_1 = k_1 \frac{K_Y C_Y K_H C_H}{1 + K_Y C_Y (1 + K_\varphi C_Y) + K_E C_E} \quad (2.38)$$

For the reaction rates of the hydrogenation of MBE to MBA and of MBY to dimers, the following equations were similarly obtained:

$$r_2 = k_2 \frac{K_E C_E K_H C_H}{1 + K_Y C_Y (1 + K_\varphi C_Y) + K_E C_E} \quad (2.39)$$

$$r_3 = k_3 \frac{K_Y K_\varphi C_Y^2 K_H^2 C_H^2}{1 + K_Y C_Y (1 + K_\varphi C_Y) + K_E C_E} \quad (2.40)$$

According to the reaction network, we derived the following set of ordinary differential equations to express the mass balances of the species involved in the process:

$$\frac{dC_Y}{dt} = \frac{n_{Pd}}{V_L}(-r_1 - 2r_3) \quad (2.41)$$

$$\frac{dC_E}{dt} = \frac{n_{Pd}}{V_L}(r_1 - r_2) \quad (2.42)$$

$$\frac{dC_A}{dt} = \frac{n_{Pd}}{V_L}r_2 \quad (2.43)$$

$$\frac{dC_D}{dt} = \frac{n_{Pd}}{V_L}r_3 \quad (2.44)$$

$$\frac{dC_H}{dt} = k_L a(C_H^* - C_H) - \frac{n_{Pd}}{V_L}(r_1 + r_2 + 2r_3) \quad (2.45)$$

The kinetic constants k_i were assumed to obey an Arrhenius temperature dependence:

$$k_i = k_{oi} \cdot \exp\left(-\frac{E_i}{RT}\right) \quad (2.46)$$

The adsorption equilibrium constants K_i were expressed as function of temperature according to the Van't Hoff equation:

$$K_i = K_{oi} \cdot \exp\left(-\frac{\Delta H_i}{RT}\right) \quad (2.47)$$

2.3.6 Results

The proposed mathematical model (Eq. (2.13), (2.38) to (2.47)) was solved according to proper initial conditions. The experimental results of the 14 runs listed in Table 2.4 were simultaneously used in a single optimization procedure in order to estimate the equilibrium and the kinetic constants (pre-exponential factors, activation energies and enthalpies of adsorption) governing the process.

The objective function $\varphi(\Theta)$ to be minimized, was expressed as:

$$\varphi(\theta) = \sum_{k=1}^q \left(\sum_{j=1}^n \frac{1}{w_{j,k}} \sum_{i=1}^m (C_{i,j,k}^{exp} - C_{i,j,k}^{cal}(\theta))^2 \right) \quad (2.48)$$

and obtained as sum of the squares of the errors between the experimental (C^{exp}) and the calculated (C^{cal}) concentration data. In Eq. (2.48) m is the number of experimental points recorded during each run, n the number of detected species and q the number of the experiments involved in the optimization. The vector θ contains the 14 parameters to be estimated. The weighting factors $w_{j,k}$ are defined as:

$$w_{j,k} = \frac{1}{m} \sum_{i=1}^m C_{i,j,k}^{exp} \quad (2.49)$$

The analysis was conducted using 528 data points to estimate 14 parameters.

In Figure 2.7 – Figure 2.10 [57] the experimental (points) and the calculated (lines) concentrations are shown for four exemplary runs carried out over different combinations of pressure (7.0 – 10.0 bar), temperature (313 – 353 K) and catalyst loading (0.175 and 0.125 wt %).

The prediction accuracy of the model was evaluated in terms of overall standard deviation calculated as:

$$\sigma_k = 100 \sum_{j=1}^n \left(\frac{1}{w_{j,k}} \sqrt{\sum_{i=1}^m \frac{(C_{i,j,k}^{exp} - C_{i,j,k}^{cal})^2}{m}} \right) \quad (2.50)$$

The proposed model appears to have a good capability to simulate the behaviour of the system. The total percentage standard deviation for the experiments in Figure 2.7 – Figure 2.10 range between 13.7 % and 15.7 %). Similar results in terms of standard deviation were

obtained for the data collected under the other studied operating conditions (data not shown).

Figure 2.11, Figure 2.12 and Figure 2.13 [57] focus on the influence of pressure, catalyst loading and temperature on MBY hydrogenation rate. The obtained results show that the proposed model is able to accurately describe the experimental trends observed when varying the operating conditions in the investigated ranges.

It is interesting to note that the depicted results exhibit a slightly acceleration of MBY hydrogenation rate during the reaction. This observation confirms the negative order of hydrogenation with respect to MBY obtained including step (2.20) in the kinetic mechanism. The negative order of reaction with respect to MBY suggests that the active sites of the catalyst remain occupied with MBY even at very low concentrations. For this reason, the adsorption of MBE and the consequent over-hydrogenation to MBA are inhibited.

The estimated parameters, result of the optimization procedure, are shown in Table 2.5 with their 95 % confidence intervals. The uncertainties associated with the estimates, remarkably low, show that the parameters were calculated with a satisfactory precision. Table 2.6 reports the most representative kinetic and adsorption constants in the investigated interval of temperatures.

At 333 K, the adsorption equilibrium constant of MBY is found to be $0.80 \pm 0.08 \text{ L mol}^{-1}$. This finding is in line with the value of 1.03 L mol^{-1} reported by Bruehwiler *et al.* [33].

In all the range of investigated temperatures K_Y appears to be significantly higher compared to the adsorption equilibrium constant of MBE K_E (K_Y/K_E ranging between 70 and 100) as reported in literature for Pd-based catalysts [58]. Meanwhile the apparent kinetic constants of MBE hydrogenation k_2 is higher than the correspondent of MBY hydrogenation k_1 (k_2/k_1 ranging between 1.1 and 1.9).

These results agree with the thermodynamic of alkyne hydrogenations. As long as the alkyne is still present in the reacting system, it occupies the catalyst active sites displacing the alkene. The high selectivity to the olefinic product is due to the stronger adsorption of alkyne compared to alkene and not to the higher kinetic constant [12]. The value obtained for the activation energy of MBY hydrogenation

E_I agrees satisfactory with the one reported by Crespo-Quesada *et al.* [32] of 25.2 kJ mol⁻¹ for Pd/ZnO structured catalyst. Furthermore, the ratio E_2/E_I is about 1.4 as proposed in literature for 1-hexyne hydrogenation over Pd-based catalyst [59]. The enthalpy of adsorption of MBY and MBE range from -20 to -30 kJ mol⁻¹, in fair agreement with the data available in literature [32][52][59].

Table 2.5: Kinetic parameter estimates with 95 % confidence intervals.

k_{01} [mol(mol _{Pd} s) ⁻¹]	$(1.13 \pm 0.1) \cdot 10^8$	E_I [kJ mol ⁻¹]	29.2 ± 1.4
k_{02} [mol(mol _{Pd} s) ⁻¹]	$(8.80 \pm 0.3) \cdot 10^9$	E_2 [kJ mol ⁻¹]	40.2 ± 2.0
k_{03} [mol(mol _{Pd} s) ⁻¹]	$(2.87 \pm 0.2) \cdot 10^8$	E_3 [kJ mol ⁻¹]	29.4 ± 1.5
K_{0Y} [L mol ⁻¹]	$(3.87 \pm 0.4) \cdot 10^{-5}$	$-\Delta H_Y$ [kJ mol ⁻¹]	27.5 ± 1.4
K_{0E} [L mol ⁻¹]	$(6.44 \pm 0.3) \cdot 10^{-6}$	$-\Delta H_E$ [kJ mol ⁻¹]	20.2 ± 1.0
K_{0H} [L mol ⁻¹]	$(1.83 \pm 0.1) \cdot 10^{-2}$	$-\Delta H_H$ [kJ mol ⁻¹]	4.7 ± 0.2
$K_{0\phi}$ [L mol ⁻¹]	$(3.80 \pm 0.2) \cdot 10^{-2}$	$-\Delta H_\phi$ [kJ mol ⁻¹]	7.3 ± 0.4

Table 2.6: Exemplary kinetic and adsorption constants at various temperatures.

	313 K	333 K	353 K
k_I [mol(mol _{Pd} s) ⁻¹]	$1.50 \cdot 10^3$	$2.95 \cdot 10^3$	$5.37 \cdot 10^3$
k_2 [mol(mol _{Pd} s) ⁻¹]	$1.71 \cdot 10^3$	$4.32 \cdot 10^3$	$9.84 \cdot 10^3$
K_Y [L mol ⁻¹]	1.51	$8.01 \cdot 10^{-1}$	$4.56 \cdot 10^{-1}$
K_E [L mol ⁻¹]	$1.52 \cdot 10^{-2}$	$9.53 \cdot 10^{-3}$	$6.30 \cdot 10^{-3}$

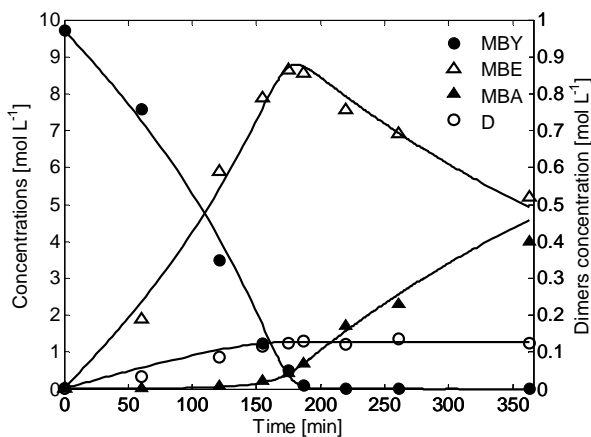


Figure 2.7: Experimental points and calculated kinetic curves. Conditions: 0.175 wt % of catalyst, 333 K, 9.0 bar, pure MBY as initial solution.

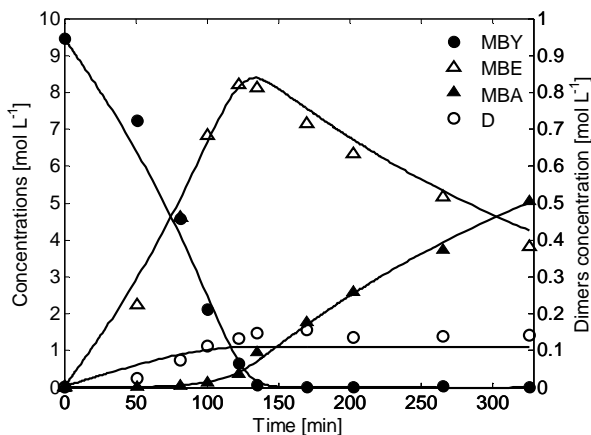


Figure 2.8: Experimental points and calculated kinetic curves. Conditions: 0.125 wt % of catalyst, 353 K, 9.0 bar, pure MBY as initial solution.

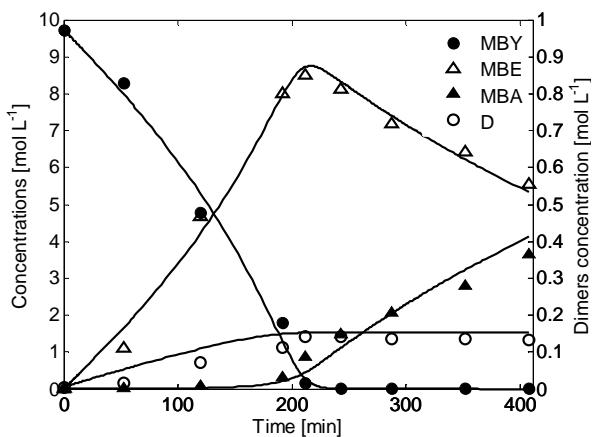


Figure 2.9: Experimental points and calculated kinetic curves. Conditions: 0.125 wt % of catalyst, 333 K, 10.0 bar, pure MBY as initial solution.

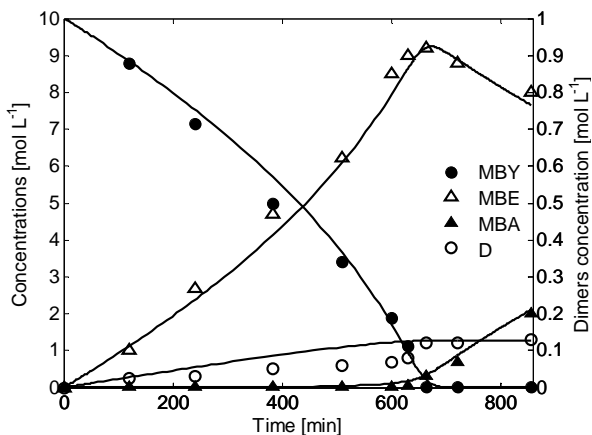


Figure 2.10: Experimental points and calculated kinetic curves. Conditions: 0.125 wt % of catalyst, 313 K, 7.0 bar, pure MBY as initial solution.

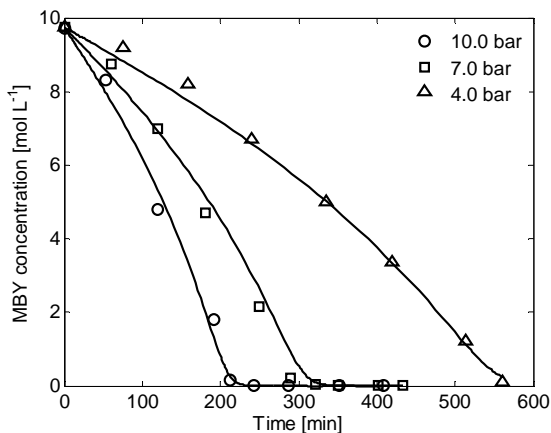


Figure 2.11: Influence of pressure on MBY hydrogenation rate: experimental points and calculated kinetic curves. Conditions: 0.125 wt % of catalyst, 333 K, pure MBY as initial solution.

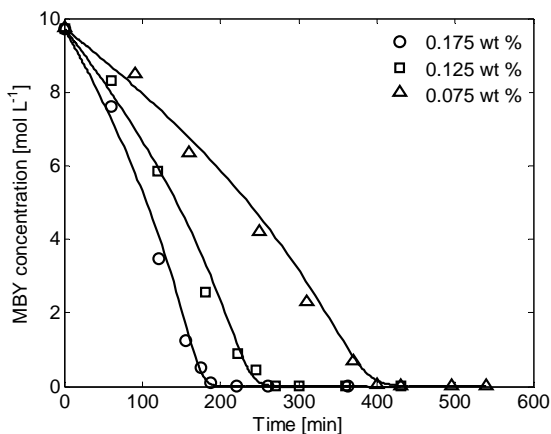


Figure 2.12: Influence of catalyst loading on MBY hydrogenation: experimental points and calculated kinetic curves. Conditions: 333 K, 9.0 bar, pure MBY as initial solution.

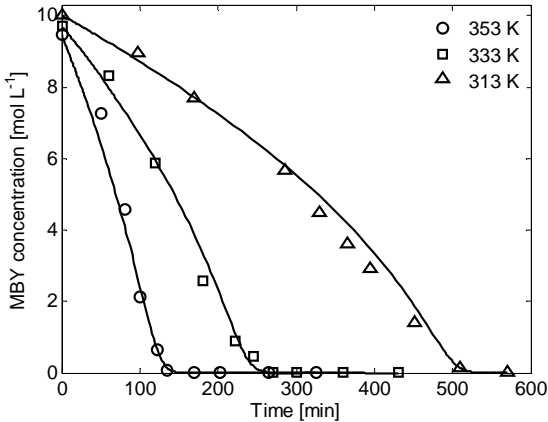


Figure 2.13: Influence of temperature on MBY hydrogenation: experimental points and calculated kinetic curves. Conditions: 0.125 wt % of catalyst, 9.0 bar, pure MBY as initial solution.

In order to validate the model and the estimated parameters, the simulation work was extended to additional experiments not included in the group used for the parametric optimization. It is worthy to note that during this validation procedure, the estimated parameters were only used to predict the experimental results without any additional adjustment. A comparison between experimental and calculated concentrations is shown in Figure 2.14 and Figure 2.15. Figure 2.14 shows the results obtained during an additional run conducted under a new combination of operating conditions chosen within the investigated ranges (343 K, 7.0 bar and a catalyst loading of 0.150 wt %). The total percentage standard deviation results to be 14.7 %.

In Figure 2.15 the results obtained with an initial solution of MBY and MBA (approximately 80 wt % of MBY) are depicted. Similar results were also obtained for an initial solution of MBY and MBE at the same concentration. The good agreement between the experimental and the calculated concentrations (total percentage standard deviation 9.3 %) shows that the model can successfully simulate the behavior of the system even at lower initial concentrations of MBY.

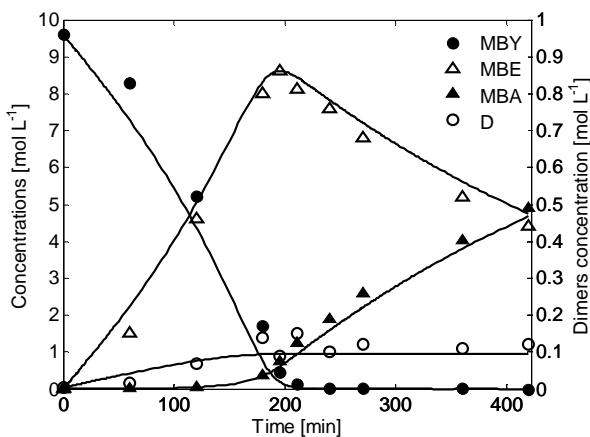


Figure 2.14: Comparison between experimental points and calculated kinetic curves. Conditions: 0.150 wt %, 343 K, 7.0 bar, pure MBY as initial solution.

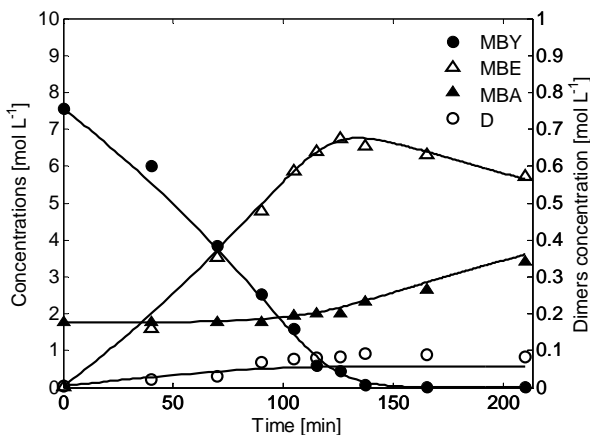


Figure 2.15: Comparison between experimental points and calculated kinetic curves. Conditions: 0.125 wt %, 353 K, 7.0 bar, initial solution: MBY 80 wt %, MBA 20 wt %.

2.3.7 Conclusions

A general kinetic model was developed to predict the hydrogenation of MBY over a commercial Pd-based catalyst.

Volumetric G-L mass transfer coefficients k_{La} were estimated in the absence of the catalyst, for different temperatures by gas absorption experiments. The L-S mass transfer coefficients k_{sas} were theoretically calculated with the Sherwood-Frössling correlation and found to be significantly higher than the correspondent k_{La} . For this reason the L-S mass transfer resistance was neglected. Hydrogen solubility in MBY was expressed as function of temperature and hydrogen pressure.

The intrinsic kinetics of the reactions involved in the network were based on a Langmuir-Hinshelwood mechanism with non-competitive adsorption of hydrogen and organics on the catalyst surface. The data of 14 runs conducted on pure MBY under different experimental conditions (temperatures 313 – 353 K, pressures 3.0 – 10.0 bar, catalyst loadings 0.075 – 0.175 wt %) were used to estimate the kinetic and the adsorption parameters governing the process. A good capability of the model to describe the behavior of the reacting system was observed for the full range of experimental conditions.

The model was validated using the best estimates of the parameters, without any further adjustment, to simulate the concentration profiles of the species during additional experiments. The validation procedure was also extended to experimental runs conducted at lower initial concentrations of MBY.

3 Kinetic modelling of the hydrogenation of dehydroisophytol

3.1 Introduction

A prominent step in the industrial production of α -tocopherol is the selective hydrogenation of dehydroisophytol (3,7,11,15-tetramethyl-1-hexadecyn-3-ol, DIP), as depicted in Figure 1.1. The target product of this reaction is isophytol (IP), a C_{20} olefinic alcohol that can be further hydrogenated to dihydroisophytol (HIP)[50][60]. This catalytic process is usually considered to follow a parallel-consecutive pathway as shown in Figure 3.1 [54][61].

The undesired reactions r_2 and r_3 affect the selectivity of the process to IP. In industry the hydrogenation of DIP is carried out in absence of solvent using palladium supported on calcium carbonate doped with a lead acetate solution (Lindlar catalyst). Typical operating ranges are 288 – 368 K and 1.2 – 8.0 bar [62].

Only a limited number of papers have been devoted in the past to the hydrogenation of DIP. Some of these contributions [63][64] investigate the effect of the operating parameters on the kinetics of the process over Pd-based catalysts without focusing on the mathematical modelling of the experimental results.

In a more recent paper Yarulin *et al.* [54] dealt with the kinetics of the hydrogenation of DIP in ethanol over unsupported Pd nanoparticles. The aforementioned study proposes a Langmuir-Hinshelwood mechanism with competitive adsorption of hydrogen and organics on the catalyst surface to model the experimental results collected over a limited range of operating conditions. Despite its wide industrial use, a detailed kinetic characterization of the solvent-free hydrogenation of DIP has not been proposed in literature.

This chapter is devoted to developing and validating a general kinetic model and a set of kinetic parameters able to simulate the behaviour of the reacting system in the typical operating ranges of industrial reactors. Different kinetic mechanisms are proposed and tested to predict the concentration profiles result of a large number of experimental runs. The kinetic study is extended to the analysis of the process selectivity to IP under varying temperatures and pressures and after the addition of quinoline in different concentrations.

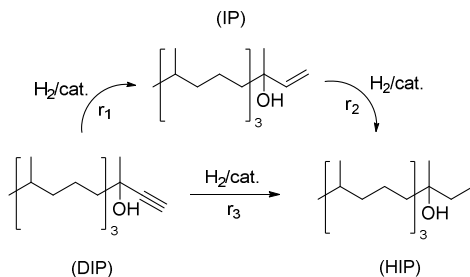


Figure 3.1: Reaction network of the hydrogenation of DIP.

3.2 Experimental

3.2.1 Materials

DIP (> 98 %) was supplied by DSM Nutritional Products. IP (95 %) for analytical purposes was purchased from aber GmbH. Quinoline (98 %) was purchased from Sigma-Aldrich.

The physical properties of DIP are listed in Table 3.1.

Hydrogen (99.995 %) and nitrogen (99.995 %), for inertization purposes, were supplied by Pangas.

The hydrogenation experiments were conducted using the commercial Lindlar catalyst characterized in the previous chapter. A fresh sample of catalyst was used for each hydrogenation experiment.

Table 3.1: Physical properties of DIP.

T	Density, ρ_L	Viscosity, $10^2 \mu_L$
[K]	[kg m ⁻³]	[Pa s]
313	840	3.31
323	831	1.79
333	821	1.08
343	812	0.71
353	803	0.49

3.2.2 Setup, procedure and analysis

The experimental setup used during this study has been extensively described in Section 2.2.2. During each experiment 7 to 10 samples of liquid solution were withdrawn at defined intervals of time from a sampling valve. The total liquid uptake never exceeded 10 % of the initial liquid mass (200 g). This volume reduction was taken into account during the analysis of the experimental data.

After dilution in ethyl acetate the samples of mixtures DIP/IP/HIP were analyzed using a Bruker GC-450 gas chromatograph with flame ionization detector (FID). The gas chromatograph was equipped with a *VF-Wax ms* separation column (25 m \times 0.25 mm, coating thickness = 0.25 μ m). The oven temperature was increased from 353 to 393 K at 20 K min⁻¹ and then to 508 K at 15 K min⁻¹. The injector and flame ionization detector temperatures were respectively 523 and 493 K.

The kinetic experiments starting from pure DIP were carried out in the temperature range 313 – 353 K and the pressure range 5.0 – 9.0 bar. Repetition of the experimental runs under the same operating conditions delivered results reproducible within 4 %.

3.3 Results and discussion

3.3.1 Hydrogen solubility

The solubility of hydrogen in DIP was experimentally estimated using the gas absorption method described in the previous chapter. The total pressure in the reactor was assumed equal to the hydrogen pressure due to the low volatility of DIP and IP (vapor pressure = $\sim 7.0 \cdot 10^{-5}$ at 373 K).

The parameters $H_0 = 2.5$ bar L mol⁻¹ and $\Delta E = -14.5$ kJ mol⁻¹ were estimated for Eq. (2.13) by linear regression of the experimental data depicted in Figure 3.2.

Hydrogen solubility was found to increase with temperature as previously reported for MBY.

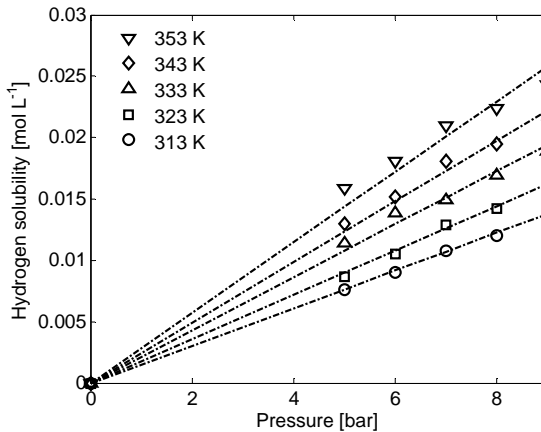


Figure 3.2: Effect of pressure and temperature on the hydrogen solubility in DIP.

3.3.2 Mass transport resistances

For the purpose of kinetic study of the hydrogenation of DIP, it is necessary to characterize quantitatively the G-L and L-S mass transport resistances.

The gas absorption method [36][37] allowed the experimental estimation of the G-L mass transfer coefficient in the absence of the catalyst.

The theoretical calculation of the L-S mass transfer coefficient k_{saS} was extensively described in the previous chapter. The catalyst particles were approximated as spherical, according to the particle size distribution by weight basis (see Table 2.2).

Due to the lack of literature data, the diffusivity of hydrogen in DIP was assumed equal to the one of hydrogen in a C₁₈ vegetable oil with viscosity similar to DIP. This diffusivity was found to span between $4.0 \cdot 10^{-9}$ and $1.0 \cdot 10^{-8}$ m² s⁻¹ in the range of temperature 313 – 353 K [46]. Additionally, the analysis of the L-S mass transfer resistances for DIP in the mixture IP/DIP was conducted for the most severe reaction conditions (353 K and 9.0 bar) at 95 % of conversion.

The Carberry numbers, defined as the ration between the observed reaction rate and the maximum transport rate were calculated, as follows, for hydrogen and DIP:

$$Ca^{GL} = \frac{r_H}{k_L a \cdot C_H^*} \quad (3.1)$$

$$Ca_H^{LS} = \frac{r_H}{k_{S_H} a_S \cdot C_H^*} \quad (3.2)$$

$$Ca_{DIP}^{LS} = \frac{r_{DIP}}{k_{S_{DIP}} a_S \cdot C_{DIP}^*} \quad (3.3)$$

This study was conducted using the initial reaction rate for hydrogen mass transfer and the DIP reaction rate at 95 % of conversion for DIP mass transfer.

The mass transfer resistances were neglected at Carberry numbers smaller than 0.1, following the criteria originally proposed by Ramachandran and Chaudari [65][66].

As observed during the study of the hydrogenation of MBY, the L-S mass transfer coefficients $k_{s a_S}$ were significantly higher than the corresponding $k_L a$ values resulting in Carberry numbers lower than 0.012.

The Carberry numbers for G-L mass transfer are plotted in Figure 3.3 at varying temperatures and pressures. The reported values, lower than 0.1 in the ranges of operating conditions, indicate negligible external mass-transfer resistances. This claim was additionally supported by measuring the catalyst activity at varying stirring rates. No effect on the initial reaction rate was observed above 16 Hz, which was regarded as an evidence of the kinetic regime.

High temperatures were obviously found to enhance the mass transfer effects due to the high observed reaction rates (Figure 3.3).

The absence of microporosity, confirmed by BET analysis, justifies the lack of internal liquid-solid diffusion limitations.

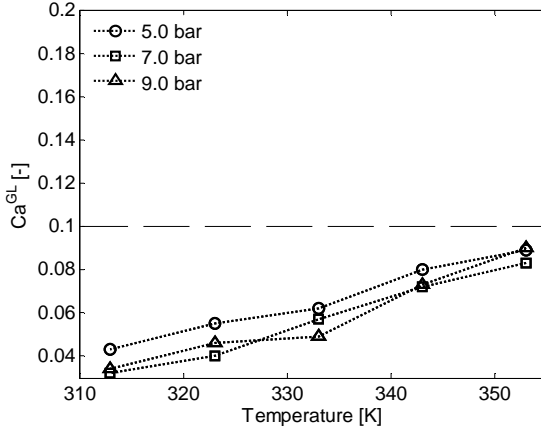


Figure 3.3: Effect of temperature and pressure on the G-L Carberry number Ca^{GL} .

3.3.3 Isophytol hydrogenation

In order to simplify the estimation of the kinetic parameters a first analysis was conducted on the subsystem consisting in the hydrogenation of IP to HIP. A simple power law kinetic expression was found to simulate satisfactory the experimental results:

$$r_2 = k_2^* C_{IP} C_H \quad (3.4)$$

The temperature dependence of the kinetic coefficient obeys an Arrhenius-type equation as:

$$k_2^* = k_{02}^* \cdot \exp\left(-\frac{E_2}{RT}\right) \quad (3.5)$$

The two rate equations:

$$\frac{dC_{IP}}{dt} = -\frac{n_{Pd}}{V_L} r_2 \quad (3.6)$$

$$\frac{dC_{HIP}}{dt} = -\frac{dC_{IP}}{dt} = \frac{n_{Pd}}{V_L} r_2 \quad (3.7)$$

were numerically integrated with the initial conditions:

$$C_j(t = 0) = C_j^0 \quad (3.8)$$

Three examples of calculated (continuous lines) and experimental (symbols) concentration profiles are shown in Figure 3.4. These experiments were conducted using, as initial solution, a mixture of IP and HIP resulting from previous hydrogenation experiments with DIP. IP (95 %) commercially available showed a lower reactivity that could be ascribed to the not identified impurities.

The optimization procedure described in Section 2.3.6 was applied in order to assess the values of the kinetic parameter $k_{o2}^* = (1.1 \pm 0.1) \cdot 10^8 \text{ L}^2(\text{mol mol}_{Pd} \text{ s})^{-1}$ and $E_2 = 47.2 \pm 2.3 \text{ kJ mol}^{-1}$.

3.3.4 Dehydroisophytol hydrogenation

The hydrogenation network depicted in Figure 3.1 was used to build the mathematical model describing the process. According to the previous study on the hydrogenation of MBY, the consumption of the alkynol during the process can be also attributed to the production of oligomers. However, the direct GC analysis conducted during the present study did not reveal the presence of heavy molecules.

Figure 3.5 shows the results of the carbon mole balances for the 15 experiments conducted during the kinetic study. The increasing trend of C-moles loss in the range of investigated temperatures indicates that additional species are formed during the hydrogenation process. These species are undoubtedly originated from DIP because the signals tend to stabilize as soon as the alkyne in the reacting system is fully consumed. As result, the loss of C-moles may be attributed to

the oligomerization of DIP. However, due to the low quantity of oligomers indirectly estimated using the mole balances (C-loss < 1.0 %), it was decided to simplify the reaction network to the scheme reported in Figure 3.1, excluding this additional reaction. The same simplification was followed in literature during previous studies dealing with the hydrogenation of DIP [54][61][67].

Kinetic data are in general insufficient to validate the mechanism of a catalytic reaction. Nevertheless, a plausible reaction mechanism has to be proposed in order to derive the kinetic expressions representing the experimental trends. Three different models were applied to describe the hydrogenation of DIP to IP:

- *Model 1:* Power-law
- *Model 2:* Langmuir-Hinshelwood kinetics with non-competitive adsorption of hydrogen and organics
- *Model 3:* Langmuir-Hinshelwood kinetics with competitive adsorption of hydrogen and organics

The mechanistic models 2 and 3 proposed for the hydrogenation of DIP to IP are depicted in Table 3.2. Similar elementary steps (not reported) were assumed for the other two reactions involved in the network. The symbols (\times) and ($*$) represent the active sites on the catalyst surface. Different active sites for hydrogen and organics in Model 2 describe the absence of competition between these molecules to adsorb on the surface of the catalyst.

Table 3.2: Kinetic mechanisms proposed for the hydrogenation of DIP to IP.

Model 2		Model 3	
$DIP + \times \xrightleftharpoons{K_{DIP}} DIP \times$	(3.9)	$DIP + \times \xrightleftharpoons{K_{DIP}} DIP \times$	(3.10)
$H_2 + 2 * \xrightleftharpoons{K_H} 2H *$	(3.11)	$H_2 + 2 \times \xrightleftharpoons{K_H} 2H \times$	(3.12)
$DIP \times + H * \xrightleftharpoons{K'_1} R_x \times + *$	(3.13)	$DIP \times + H \times \xrightleftharpoons{K'_1} R_x \times + \times$	(3.14)
$R_x \times + H * \xrightleftharpoons{k'_1} IP \times + *$	(3.15)	$R_x \times + H \times \xrightleftharpoons{k'_1} IP \times + \times$	(3.16)
$IP + \times \xrightleftharpoons{K_{IP}} IP \times$	(3.17)	$IP + \times \xrightleftharpoons{K_{IP}} IP \times$	(3.18)

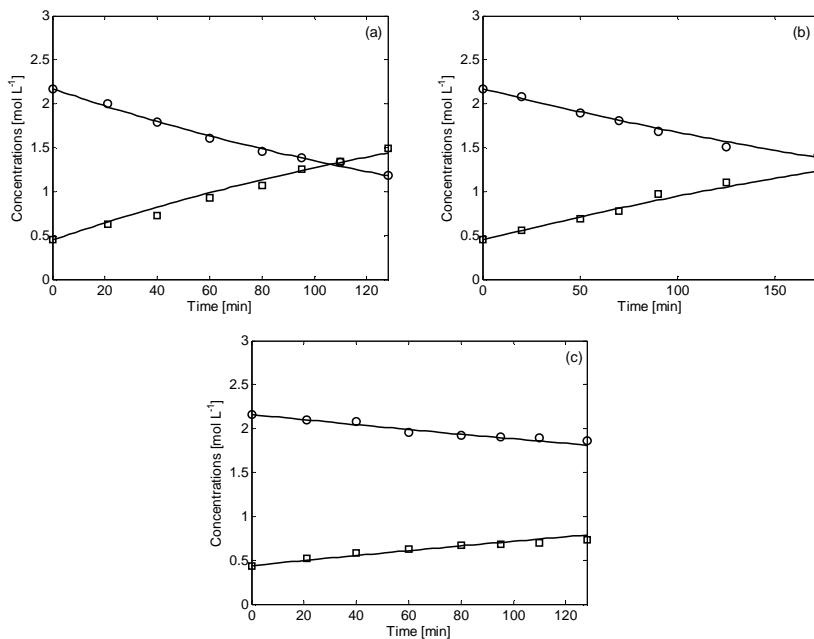


Figure 3.4: Predicted (continuous lines) and experimental (symbols) concentration profiles for the hydrogenation of IP at 7.0 bar, 353 K (a), 343 K (b), 333 K (c), catalyst loading = 0.1 wt %. (○) IP, (□) HIP.

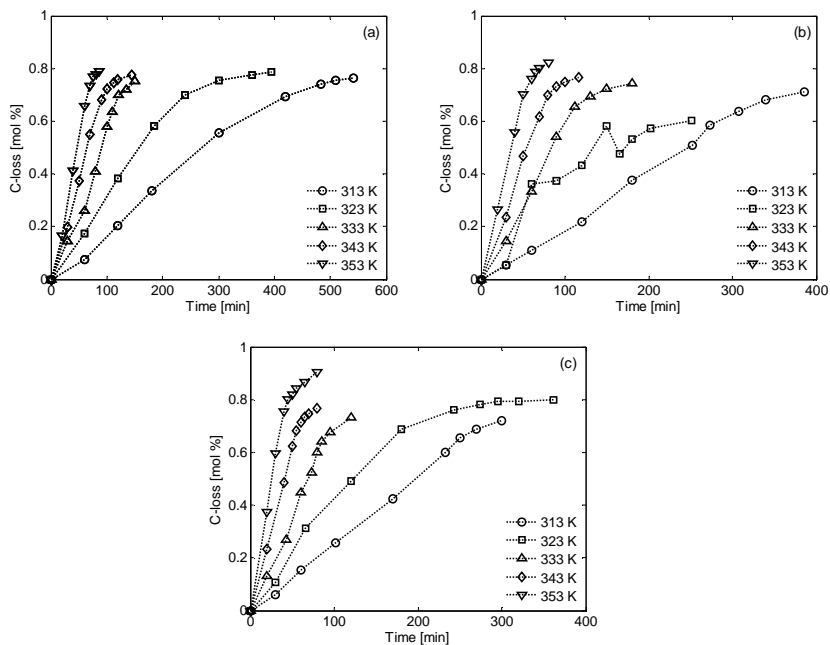


Figure 3.5: Carbon loss during the DIP hydrogenation experiments at various temperatures and 5.0 bar (a), 7.0 bar (b), 9.0 bar (c).

Table 3.3: Kinetic expressions of the reaction rates proposed for the hydrogenation of DIP.

Model	$DIP \rightarrow IP$
1	$r_1 = k_1 C_{DIP} C_H$
2	$r_1 = k_1 \frac{K_{DIP} C_{DIP} K_H C_H}{(1 + K_{DIP} C_{DIP} + K_{IP} C_{IP})(1 + \sqrt{K_H C_H})}$
3	$r_1 = k_1 \frac{K_{DIP} C_{DIP} K_H C_H}{(1 + K_{DIP} C_{DIP} + K_{IP} C_{IP} + \sqrt{K_H C_H})^2}$
Model	$DIP \rightarrow HIP$
1	$r_3 = k_3 C_{DIP} C_H^2$
2	$r_3 = k_3 \frac{K_{DIP} C_{DIP} (K_H C_H)^2}{(1 + K_{DIP} C_{DIP} + K_{IP} C_{IP})(1 + \sqrt{K_H C_H})}$
3	$r_3 = k_3 \frac{K_{DIP} C_{DIP} (K_H C_H)^2}{(1 + K_{DIP} C_{DIP} + K_{IP} C_{IP} + \sqrt{K_H C_H})^2}$

The adsorption and desorption elementary steps were assumed to be in equilibrium as previously discussed for the hydrogenation of MBY. Furthermore, the last hydrogen additions (Eq. (3.15) and (3.16)) were considered the rate determining steps.

Table 3.3 shows the analytical expressions finally deduced for the rates of reaction. The adsorption of HIP on the catalyst surface is neglected due to the weak adsorption of the single bond on the surface of Pd-based catalysts [33][59].

The mole balances for DIP and the hydrogenated species can be expressed by the following set of ordinary differential equations.

$$\frac{dC_{DIP}}{dt} = -\frac{n_{Pd}}{V_L} (r_1 + r_3) \quad (3.19)$$

$$\frac{dC_{IP}}{dt} = \frac{n_{Pd}}{V_L} (r_1 - r_2) \quad (3.20)$$

$$\frac{dC_{HIP}}{dt} = \frac{n_{Pd}}{V_L} (r_2 + r_3) \quad (3.21)$$

This system was numerically integrated with the initial conditions:

$$C_j(t = 0) = C_j^0 \quad (3.22)$$

The temperature dependency of the kinetic constants was modeled with the same approach previously used for k_2 . The van't Hoff equation describes the temperature dependency of the adsorption coefficients:

$$K_i = K_{oi} \cdot \exp\left(-\frac{\Delta H_i^{ad}}{RT}\right) \quad (3.23)$$

The experimental and theoretical selectivities to IP can be calculated as:

$$S_{IP} = \frac{C_{IP} - C_{IP}^0}{C_{DIP}^0 - C_{DIP}} \quad (3.24)$$

Conversion of DIP is expressed by:

$$X_{DIP} = \frac{C_{DIP}^0 - C_{DIP}}{C_{DIP}^0} \quad (3.25)$$

15 experimental runs were conducted combining pressure and temperature levels (operating conditions listed in Table 3.4). The catalyst loading was 0.1 wt % for all the experiments.

The results of these runs were used in the single optimization procedure described in Section 2.3.6. The kinetic parameters previously estimated for reaction 2 were used without any further adjustment during this second optimization. Both mechanistic models have the same number of parameters to be estimated (10) while the power-law kinetics only use 4 parameters.

Table 3.5 shows the values of the objective function $\varphi(\Theta)$ (defined in the previous chapter) calculated at the end of the optimization procedures conducted using the three investigated kinetic models.

Compared to the empirical power-law, the mechanistic kinetic models (2 and 3) result in a better fit of the experimental data. A slightly better result in terms of objective function has been observed for Model 2. It is worth noting that the hypothesis of non-competitive adsorption between hydrogen and organics is widely accepted in literature for similar hydrogenation of alkynes [52][68].

Figure 3.6, Figure 3.7 and Figure 3.8 show the results of the optimization procedure (using Model 2) as visual comparison between calculated (continuous curves) and experimental concentrations (symbols) of DIP, IP and HIP [69]. The goodness of the fitting can be evaluated with the overall standard deviations σ listed in Table 3.4.

Acceptable results ($\sigma < 15\%$) were obtained for all the runs involved in the optimization indicating the suitability of the proposed model to describe the investigated hydrogenation process. An advantage of the proposed model is that it allows the study of the hydrogenation of DIP without including the full kinetic complexity of IP hydrogenation.

Table 3.4: Operating conditions of the experimental runs used during the optimization procedure and overall percentage standard deviations.

Run	T [K]	p [bar]	σ [%]	Run	T [K]	p [bar]	σ [%]
1	353	9.0	11.9	9	323	7.0	7.4
2	343	9.0	4.2	10	313	7.0	5.7
3	333	9.0	9.7	11	353	5.0	8.9
4	323	9.0	11.3	12	343	5.0	7.7
5	313	9.0	9.6	13	333	5.0	7.8
6	353	7.0	9.1	14	323	5.0	14.8
7	343	7.0	9.6	15	313	5.0	14.1
8	333	7.0	7.4				

Table 3.5: Values of the objective function $\varphi(\Theta)$ calculated at the end of the optimization procedure.

Model	φ value [mol L ⁻¹]
1	16.8
2	5.1
3	5.6

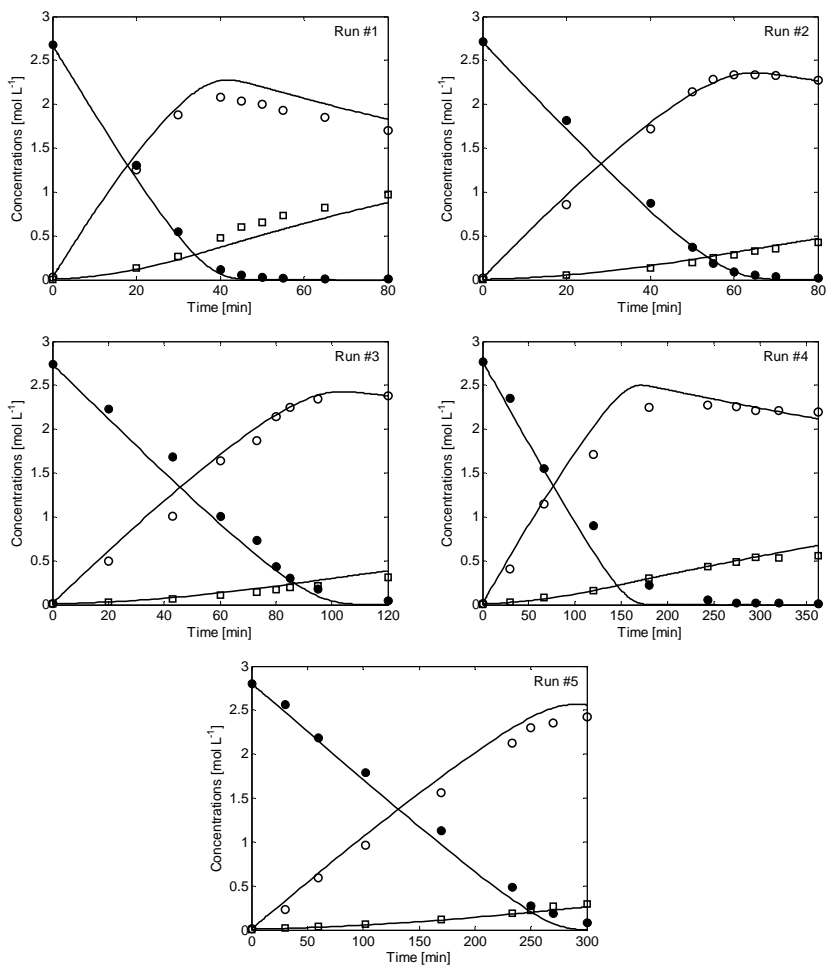


Figure 3.6: Predicted (continuous lines) and experimental (symbols) concentration profiles for the hydrogenation of DIP at 9.0 bar. The operating conditions of the runs are listed in Table 3.4. (●) DIP, (○) IP, (□) HIP.

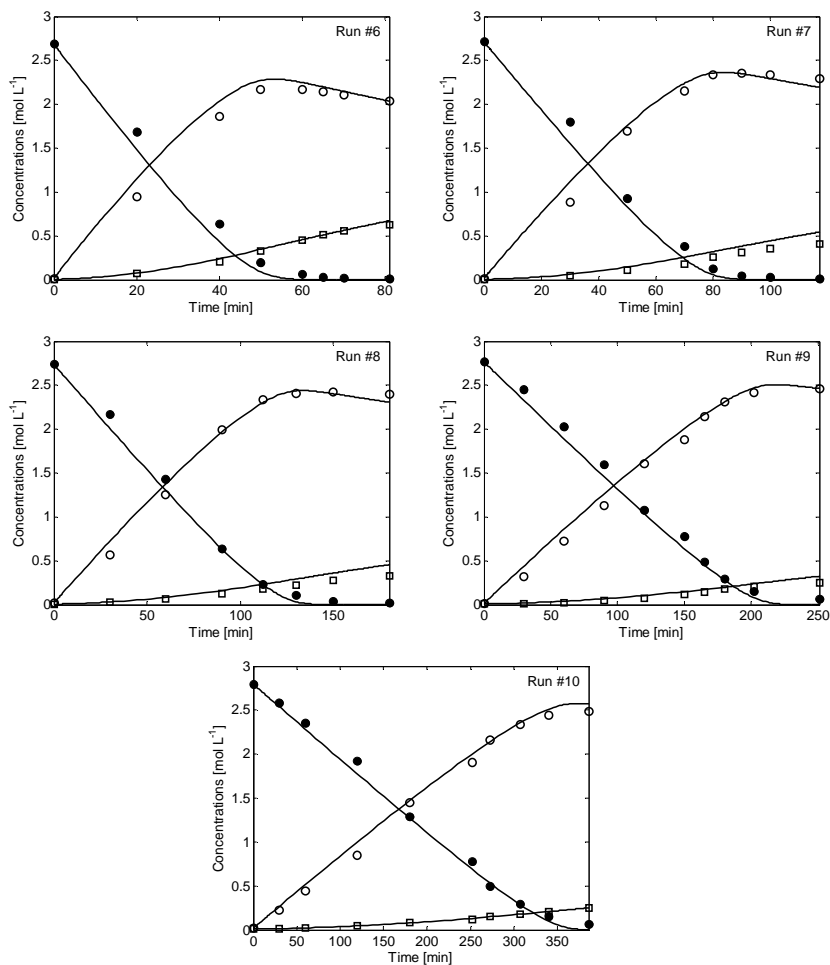


Figure 3.7: Predicted (continuous lines) and experimental (symbols) concentration profiles for the hydrogenation of DIP at 7.0 bar. The operating conditions of the runs are listed in Table 3.4. (●) DIP, (○) IP, (□) HIP.

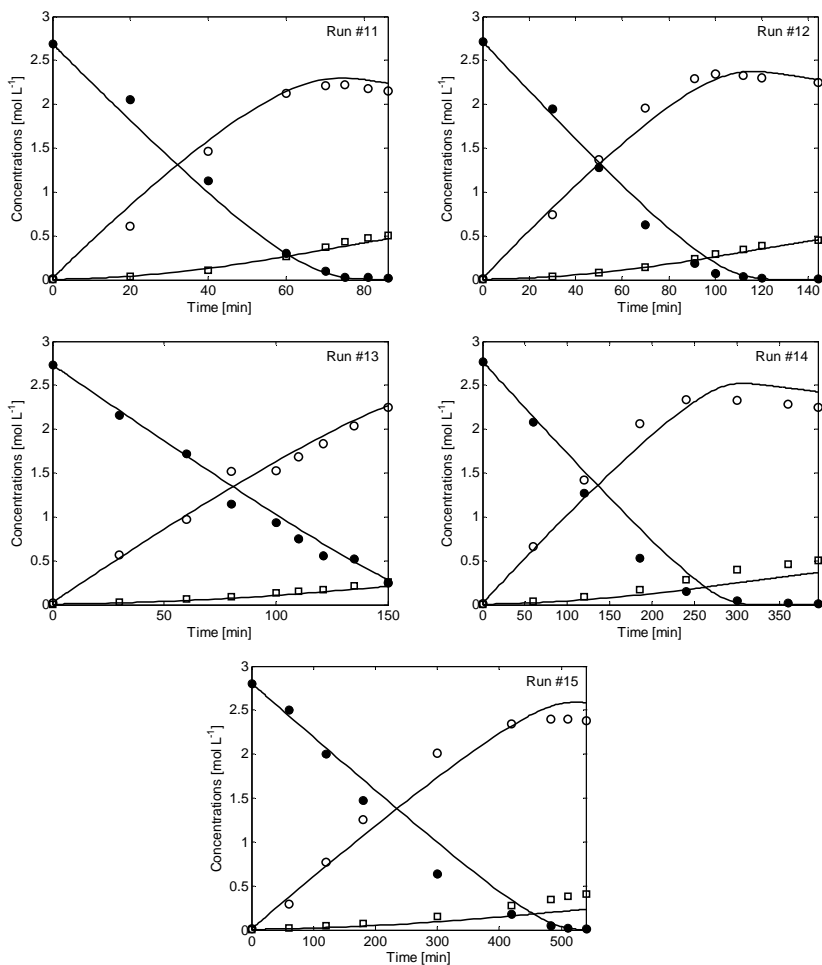


Figure 3.8: Predicted (continuous lines) and experimental (symbols) concentration profiles for the hydrogenation of DIP at 5.0 bar. The operating conditions of the runs are listed in Table 3.4. (●) DIP, (○) IP, (□) HIP.

In some cases the prediction of the maximum on IP profile is not excellent (runs #4, #14, #15). However, the predicted times of maximum IP concentration fall in general in the range experimentally estimated as demonstrated by Figure 3.9.

In Table 3.6 the best-estimated values of the unknown kinetic and adsorption parameters for Model 2 are reported along with their 95 % confidence intervals.

The ratio k_1/k_2 is higher than 1 as reported by Yarulin *et al.* for the same reacting system resulting in a favorable alkene formation [54].

The ratio of the adsorption equilibrium constants K_{DIP}/K_{IP} ranges between 12 and 31 in the field of investigated temperatures. In general this ratio is reported to be higher for alkyne/alkene systems with shorter hydrocarbon tail [12][32][58]. However, this finding is consistent with the relatively low selectivity to alkene of this hydrogenation compared with similar processes involving smaller alkynes [54].

Figure 3.10 shows the selectivity profiles during the hydrogenation of DIP at 7.0 bar in the temperature range 323 – 353 K.

The continuous lines represent the theoretical selectivities calculated using the proposed mathematical model and the best-estimated values for the kinetic and adsorption parameters. The selectivity appears to decrease with temperature in the range of investigated conditions. This finding is consistent with the results recently shown for the hydrogenation of propyne over Pd-based catalysts [70].

Table 3.6: Estimated kinetic and adsorption parameters for Model 2 with 95 % confidence intervals.

k_{01} [mol(mol _{Pd} s) ⁻¹]	$(2.3 \pm 0.1) \cdot 10^8$	E_1 [kJ mol ⁻¹]	37.2 ± 1.9
k_{03} [mol(mol _{Pd} s) ⁻¹]	$(2.2 \pm 0.6) \cdot 10^7$	E_3 [kJ mol ⁻¹]	17.2 ± 1.4
K_{0DIP} [L mol ⁻¹]	$(2.4 \pm 0.1) \cdot 10^5$	$-\Delta H_{DIP}$ [kJ mol ⁻¹]	68.9 ± 3.4
K_{0IP} [L mol ⁻¹]	$(2.1 \pm 0.3) \cdot 10^3$	$-\Delta H_{IP}$ [kJ mol ⁻¹]	48.3 ± 2.4
K_{0H} [L mol ⁻¹]	$(3.6 \pm 0.2) \cdot 10^2$	$-\Delta H_H$ [kJ mol ⁻¹]	5.1 ± 0.2

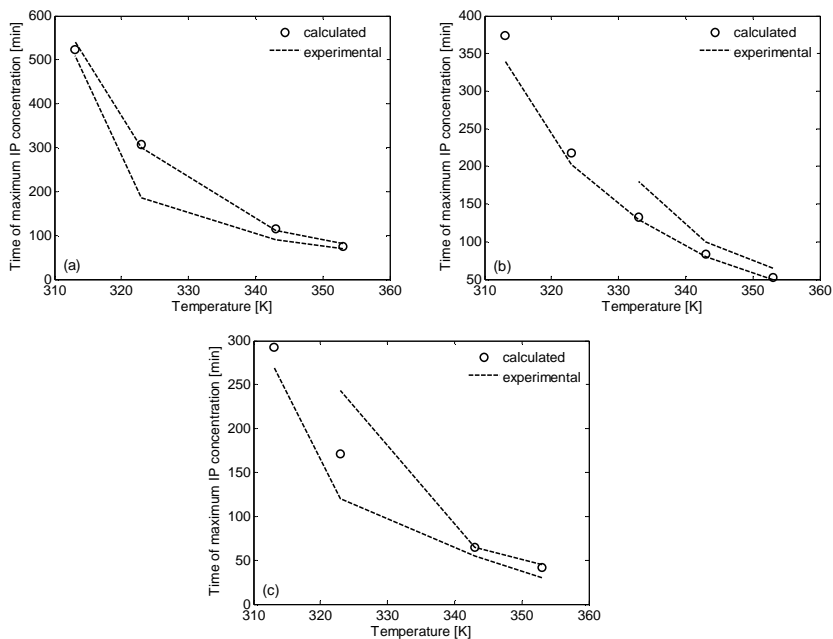


Figure 3.9: Time of maximum IP concentration at varying temperatures for the experimental runs conducted at 5.0 bar (a), 7.0 bar (b), 9.0 bar (c). The dotted lines delimit the experimental ranges of the maximum IP concentrations.

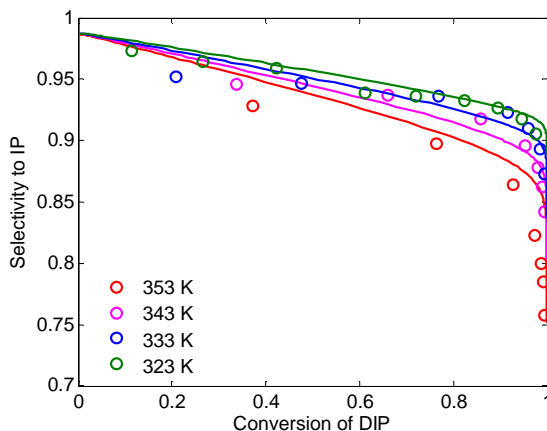


Figure 3.10: Effect of temperature on the selectivity to IP. Predicted (continuous lines) and experimental (symbols) selectivity profiles at 7.0 bar.

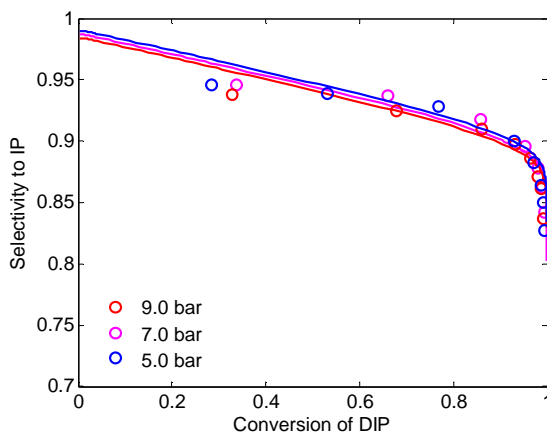


Figure 3.11: Effect of pressure on the selectivity to IP. Predicted (continuous lines) and experimental (symbols) selectivity profiles at 343 K.

The direct hydrogenation of the triple to the single bond is often neglected during alkyne hydrogenations [50]. The validity of this assumption may be confirmed by the large uncertainty relative to the estimated pre-exponential factor k_{03} . However, a detailed analysis of the process selectivity takes benefit of including the direct hydrogenation r_3 in the reaction network. The case $r_3 = 0$ results into a higher initial selectivity ($S_{IP} = 1$ at $X_{DIP} = 0$) and, as consequence, in a worse fitting of the profiles depicted in Figure 3.10.

The selectivity drop with temperature is accentuated by the ratio between the activation energies $E_2/E_1 > 1$. Similar values for this ratio are reported in literature for other alkyne hydrogenations [59].

Figure 3.11 shows the experimental and calculated selectivity profiles for varying pressures. No significant effect of the pressure is observed due to the narrow investigated interval (5.0 – 9.0 bar). This finding can be also considered a confirmation of the same order of reaction with respect to hydrogen for both hydrogenations of DIP and IP in the investigated range of conditions. According to the proposed mathematical model this order of reaction is approximately 1 being $K_H C_H \ll 1$. A different reaction order of the hydrogenations in series would result in a more pronounced influence of the pressure on the process selectivity.

In Figure 3.10 and Figure 3.11 the mathematical model exhibits good predictions of the experimental selectivity especially at conversions relevant for industrial processes ($X_{DIP} > 0.9$). A slightly overestimation of the slope of the selectivity profiles is depicted at low conversions. A better agreement with the experimental results could be obtained including the production of oligomers from DIP in the reaction network.

3.3.5 Model validation

Additional experiments were conducted at varying catalyst loadings and varying initial concentrations of DIP, IP and HIP. The experimental results of these runs were simulated using the proposed mathematical model without any adjustment of the estimated parameters. Two examples, result of this validation procedure, are

shown in Figure 3.12 and Figure 3.13 with the estimated overall standard deviations.

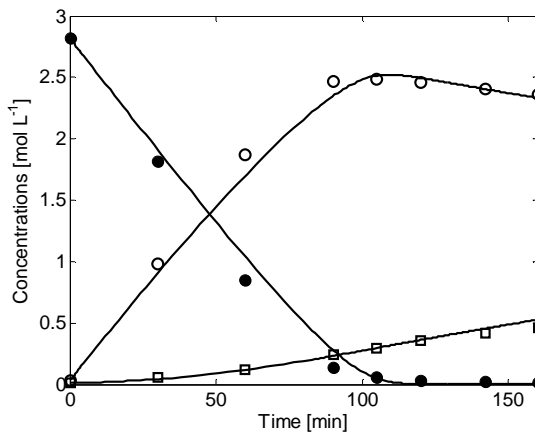


Figure 3.12: Comparison between calculated (continuous lines) and experimental (symbols) concentration profiles. Conditions: 333 K, 7.0 bar, catalyst loading = 0.125 wt %. (●) DIP, (○) IP, (□) HIP. $\sigma = 7.2\%$.

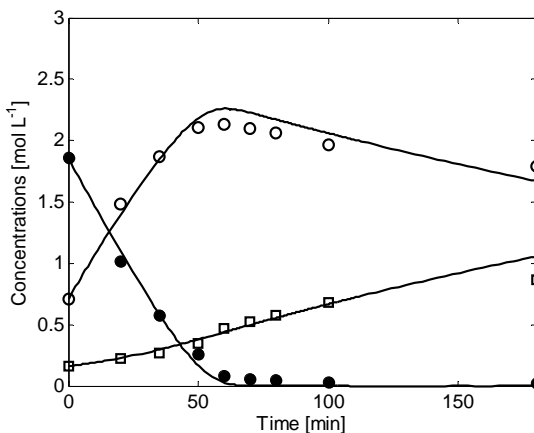


Figure 3.13: Comparison between calculated (continuous lines) and experimental (symbols) concentration profiles. Conditions: 343 K, 7.0 bar, catalyst loading = 0.1 wt %, initial concentration: 68 wt % DIP, 26 % IP, 6 wt % HIP. (●) DIP, (○) IP, (□) HIP. $\sigma = 7.4$ %.

3.3.6 Effect of quinoline

In order to improve the selectivity of the process to IP, quinoline was added to the reaction mixture with different concentrations ranging between 0.5 and 5.0 wt %. The effect of quinoline on the alkyne hydrogenation is usually ascribed to its preferential adsorption on the catalyst active sites [71]. Nitrogen bases are also thought to donate electrons to Pd modifying the adsorption strength of alkynes and alkenes [72][73].

In this work, no significant change in the reaction rate of DIP was observed after addition of quinoline. On the other hand, it contributed to a drastic decrease of the over-hydrogenation rate to HIP. For this reason, an attempt to simulate the experimental results, was conducted simply replacing Eq. (3.4) of the mathematical model with the following:

$$r_2 = k_2^* \left(\frac{C_{IP}C_H}{1 + \gamma C_Q} \right) \quad (3.26)$$

where γ is a parameter describing the inhibition of IP hydrogenation caused by the addition of quinoline.

The optimization procedure, previously described, was applied to simulate the results of 4 experimental runs conducted in presence of quinoline by estimating the only additional parameter γ . The 12 kinetic and adsorption parameters previously reported were used without any further adjustment. Figure 3.14 and Figure 3.15 show the effect of quinoline respectively on the concentration profile of HIP and on the selectivity to IP at 343 K and 7.0 bar.

The lower reaction rate of HIP formation corresponds to a higher selectivity to IP. The effect of quinoline is also evident at very low concentration (0.5 wt %). The calculated profiles depicted in Figure 3.14 correspond to an estimated parameter $\gamma = (7.1 \pm 0.7) \cdot 10 \text{ L mol}^{-1}$ at 343 K. It is evident that the proposed mathematical model with the addition of the only parameter γ is able to predict the effect of different concentrations of quinoline in the reaction mixture both in terms of concentration and selectivity profiles.

It is worth noting that the effect of the modifier incorporated in this manner in the model does not fully explain the mechanism of selectivity enhancing. Different electronic properties of the catalyst surface should be the consequence of the electron donation of quinoline to Pd. This would result into different adsorption constants for all reactants and products. Further investigations in this direction are currently in progress.

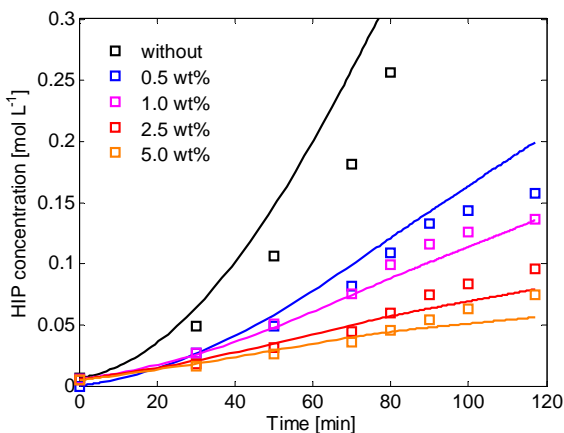


Figure 3.14: Predicted (continuous lines) and experimental (symbols) profiles for concentration of HIP during the hydrogenation of DIP with and without addition of quinoline. Conditions: 7.0 bar, 343 K and catalyst loading = 0.1 wt %.

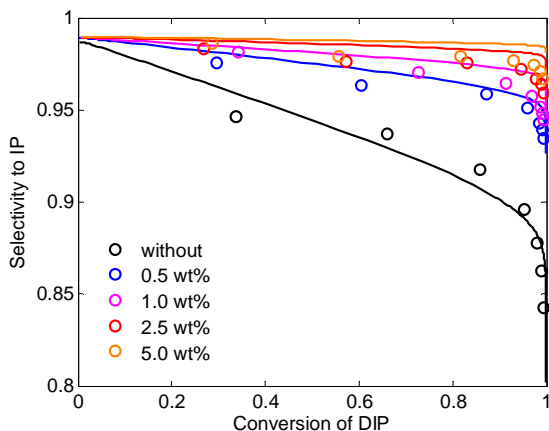


Figure 3.15: Predicted (continuous lines) and experimental (symbols) profiles for selectivity to IP during the hydrogenation of DIP with and without addition of quinoline. Conditions: 7.0 bar, 343 K and catalyst loading = 0.1 wt %.

3.3.7 Conclusions

In this chapter the hydrogenation of dehydroisophytol has been studied in absence of solvent. A mathematical model is proposed based on the results of experimental runs collected in a range of operating conditions relevant for industrial applications. The intrinsic rate of reactions are based on a Langmuir-Hinshelwood kinetic mechanism with non-competitive adsorption of hydrogen and organics on the catalyst surface. The mathematical model exhibits a satisfactory capability to describe the behavior of the system with overall standard deviations lower than 15 %.

The model is proved to reliably predict the selectivity of the process to isophytol under varying temperatures and pressures. No significant effect of the pressure on the process selectivity are observed. On the other hand increasing the operating temperature has a negative effect on the selectivity. This effect is enhanced by the ratio of the activation energies $E_2/E_1 > 1$. The validation of the proposed model has been conducted using the best estimated parameters to predict the concentration profiles of experimental runs at varying catalyst loadings and initial concentrations. The model was finally extended to predict the selectivity enhancing effect of the addition of a modifier (quinoline) to the reacting system.

The knowledge of the parameters governing kinetics and selectivity of the process is of crucial importance for designing new reactors concepts that could, in the future, intensify and improve the synthesis of isophytol.

4 A Pd/ZnO catalyst for selective hydrogenation of alkynes

4.1 Introduction

As previously discussed, the hydrogenation of MBY is carried out in industry for production of vitamins and fine chemicals. High selectivities to MBE are required due to the difficulties in separation of the mixture MBE/MBA [19]. A typical approach to enhance the selectivity (see Section 3.3.6) during alkyne hydrogenations is the addition of nitrogen-based modifiers (e.g. quinoline, pyridine, ammonia) [73]. These electron donor compounds inhibit alkene surface interactions due to their preferential adsorption on the surface of the catalyst [74]. However, this incorporation requires further process steps, such as separation, resulting in additional costs.

Alternative approaches have mostly been directed on catalyst modifications. Bimetallic catalysts, for example, are known to improve olefin selectivity during alkyne hydrogenations [54].

Zinc, in particular, is known to act as a promoter in the palladium-based catalysts because of its ability to form an intermetallic Pd-Zn phase affecting the adsorption strength of alkynes and alkenes [73][75].

The performance of Pd-based catalysts during alkyne hydrogenations is also strongly influenced by the nature of the support. ZnO in

particular is often considered a good alternative to CaCO_3 with respect to reaction selectivity [73]. High selectivities towards the alkene have been reported for monometallic Pd-based catalysts over ZnO [32][73][76]. The electron donating effect of Zn results in a higher electron density of Pd. The selectivity of the process is enhanced due to a decreased alkene adsorption [77]. This makes these catalysts a valuable alternative to the lead-containing Lindlar catalyst, well suited for industrial applications.

Goal of this chapter is characterizing the performances of a Pd/ZnO/ Al_2O_3 catalyst patented by DSM Nutritional Products for the hydrogenation of MBY [78]. This catalyst is coated on a metal support and is, for this reason, suitable for application in a structured reactors.

The performance of the Pd/ZnO catalyst in terms of MBE selectivity are compared with the ones achievable with a commercial Lindlar catalyst under the same operating conditions and the same palladium loading.

The catalytic response of the Pd/ZnO system on the reaction selectivity for alkynols with different hydrocarbon tail length (DIP) is also addressed.

4.2 Experimental

4.2.1 Catalyst preparation

The catalyst used during this study was prepared at DSM Nutritional Products following the procedure described below.

EOS MaragingSteel MS1 metal powder (20.0 g) was heated in an oven under air at 723 K for 3 h. The resulting metal powder was initially coated with an $\text{Al}_2\text{O}_3/\text{ZnO}$ base layer. Separately a solution of Pd nanoparticles was prepared and deposited on the metal powder containing the $\text{Al}_2\text{O}_3/\text{ZnO}$ layer.

A solution of $\text{Al}(\text{NO}_3)_3 \cdot 9\text{H}_2\text{O}$ (200 g) in water (700 mL) was heated to 368 K and ZnO powder (43.4 g) was added slowly. The mixture was stirred until completely dissolved. After cooling to room

temperature, the solution was filtered. The oxidized metal powder (20.0 g) was added to 50 mL of the Al/Zn solution and the mixture was stirred at room temperature for 15 min, filtered through a 0.45 μm membrane filter and dried under vacuum at 313 K for a minimum of 2 h. This process was repeated two additional times.

Sodium molybdate dihydrate (162 mg) and anhydrous palladium(II)chloride (108 mg) were added in 30 mL of deionized water. The solution was evaporated slowly under stirring until a solid residue was formed. Afterwards, 30 mL of deionized water were added to the solid residue. This evaporation-dissolving cycle was repeated two times in order to completely dissolve the palladium salt. Finally, 50 mL of hot water were added to the solid residue. The deep brown solution was cooled down to room temperature, filtered and water was added to adjust the volume to 60 mL. Hydrogen gas was slowly bubbled through the solution at room temperature for 1 h. The obtained solution of Pd(0) was added to a suspension of the metal powder- $\text{Al}_2\text{O}_3/\text{ZnO}$ in water (60 mL). The mixture was stirred for 30 min and then filtered. The powder was finally dried under vacuum at 313 K overnight. The catalyst was thermally activated in a tube furnace at 573 K for 4 h (temperature ramp 10 K min^{-1}) under H_2 -Ar flow (1:9; total flow rate: 450 mL min^{-1}). The performances of the catalyst were tested in the setup previously described in Section 2.2.2 following the same experimental procedure.

4.2.2 Catalyst characterization

The microstructure of the catalyst was observed by FIB/SEM (Zeiss NVision 40) equipped with EDX apparatus. Samples were opened at the region of interest through milling with gallium-ions at 30 kV/6 nA perpendicular to the sample surface. The cross section was polished at 30 kV/1.5 nA and imaged by detection of secondary electrons (SE) using an in-lens detector. EDX measurements were performed at 9 kV.

The morphology of the supported Pd-nanoparticles was studied by HAADF-STEM conducted on an aberration-corrected dedicated STEM microscope HD-2700CS (Hitachi). The microscope was oper-

ated at an acceleration potential of 200 kV. Temperature programmed oxidation/reduction (TPO/TPR) were performed in a Micrometrics AutoChem 2920 II instrument using 5 vol % of O₂/H₂ in Ar. The data were collected at a ramp of 8 K min⁻¹.

4.3 Results

4.3.1 Catalyst characterization

Some of the physical characteristics of the Pd/ZnO catalyst are listed in Table 4.1.

Table 4.1: Pd/ZnO catalyst characteristics.

Property	Value
	< 73 for 100%
	< 43 for 73 %
Cumulative particles	< 36 for 58 %
size distribution	< 21 for 20 %
[μm]	< 10 for 3 %
	< 4 for 1.5 %
	< 2 for 1 %
d_{50}	32
[μm]	
BET surface area	1.5
[$\text{m}^2 \text{g}^{-1}$]	
Density, ρ_S	~ 8000
[kg m^{-3}]	
Pd loading	0.22
[wt %]	

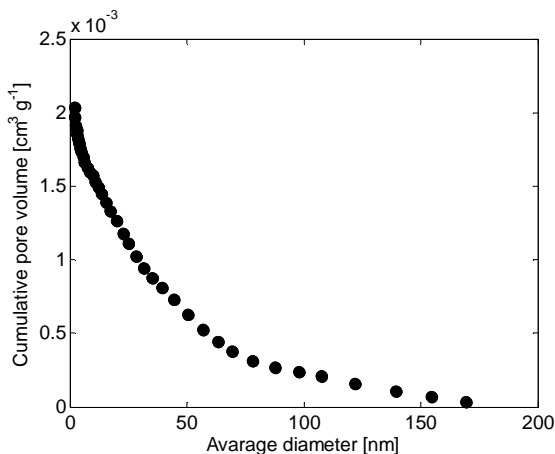


Figure 4.1: Cumulative pore volume distribution of Pd/ZnO catalyst supported on a metal powder with average diameter $d_{50} = 32 \mu\text{m}$.

Analysis of the catalyst surface using BET techniques gives a surface of $\sim 1.5 \text{ m}^2 \text{ g}^{-1}$, in addition to the cumulative pore size distribution depicted in Figure 4.1.

The analysis revealed a total specific pore volume of $\sim 2.0 \cdot 10^{-3} \text{ cm}^3 \text{ g}^{-1}$, a volume of mesopores (2 – 50 nm) of $\sim 1.3 \cdot 10^{-3} \text{ cm}^3 \text{ g}^{-1}$ and a negligible volume of micropores ($< 2 \text{ nm}$). The extremely low pore volume is beneficial in order to avoid internal diffusion limitations during kinetic studies.

Figure 4.2 (a) shows the TPR profiles obtained before (black) and after (red) the temperature oxidation study depicted in Figure 4.2 (b).

Higher intensity were observed after the oxidation of the sample. The principal peaks at around 730 K were attributed to the reduction of ZnO. It is reported that ZnO species start to be reduced at 875 K. However, this peak can be shifted to lower temperatures when Pd is supported on the surface of ZnO/Al₂O₃ [79]. The weak peak at around 330 K (red profile) after the oxidation of the sample can be ascribed to the reduction of PdO to metallic Pd.

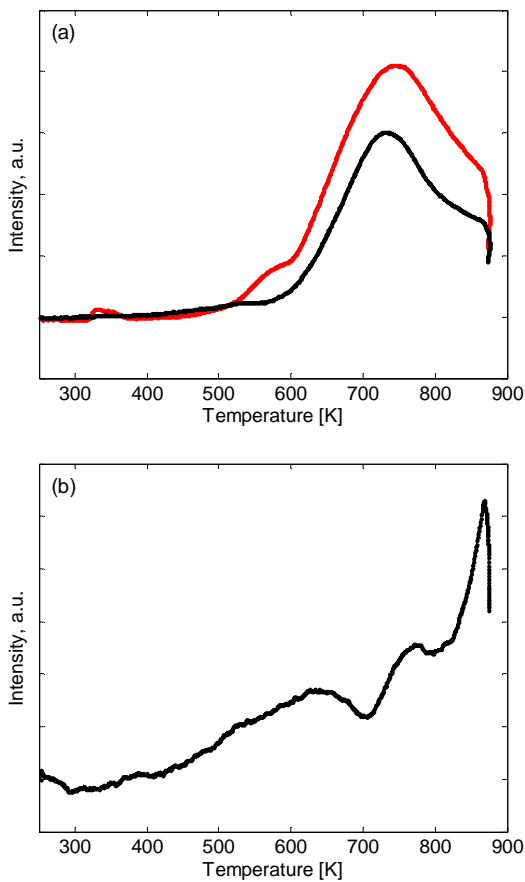


Figure 4.2: (a) TPR profiles of Pd/ZnO catalyst before (black) and after (red) temperature oxidation study. (b) TPO profile of Pd/ZnO catalyst.

The TPO profile shows three peaks at around 640, 760 and 850 K to which it is difficult to ascribe definite oxidation stages. The first peak at around 650 K could be ascribed to Pd oxidation. However, the recorded low signals, resulting from the low Pd loading of the catalyst, do not make the analysis suitable for quantitative investigations.

Figure 4.3 (a) and (b) show an SEM microphotograph of a catalyst particle with diameter of about 50 and its cross section obtained by FIB. A magnified detail of the coating layer is depicted in (c). The metal particle appears to be fully coated with an homogenous base layer. The coating layer (about 700 nm thick) remains intact after Pd deposition and thermal activation. EDX analysis reveals that Pd is dispersed only on the external surface of the catalyst while Al and Zn are the main components of the base layer [80]. The surface of the catalyst appears to be decorated by large metal clusters (sizes 100 – 200 nm) containing Pd according to EDX measurements [80].

HAADF-STEM images provided in Figure 4.4 reveal that the supported Pd-nanoparticles exhibit different diameters up to ca 10 nm. Nevertheless they are often agglomerated in certain regions.

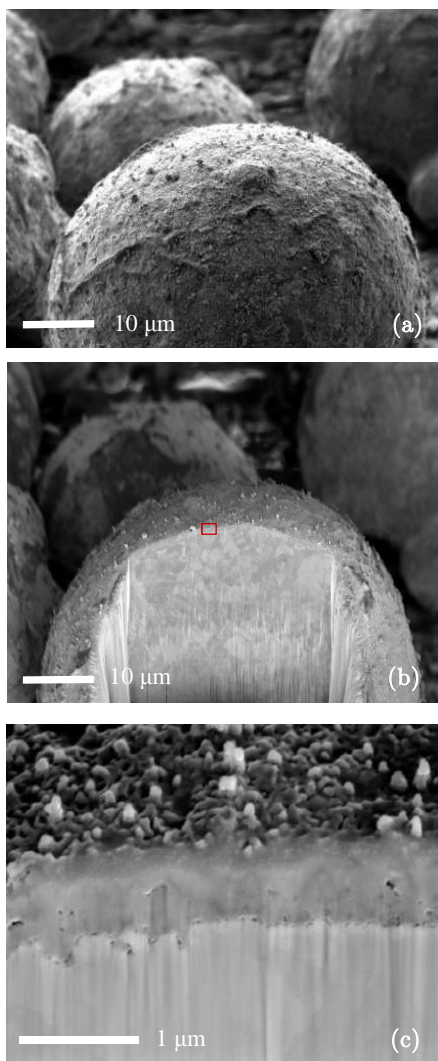


Figure 4.3: (a) SEM microphotograph of a catalyst particle with diameter of about 50 μm . Detector: SE2, voltage: 2 kV. (b) Cross section of the catalyst particle. Detector: In-Lens, voltage: 2 kV (c) Magnified image of the selected area (red box) in (b).

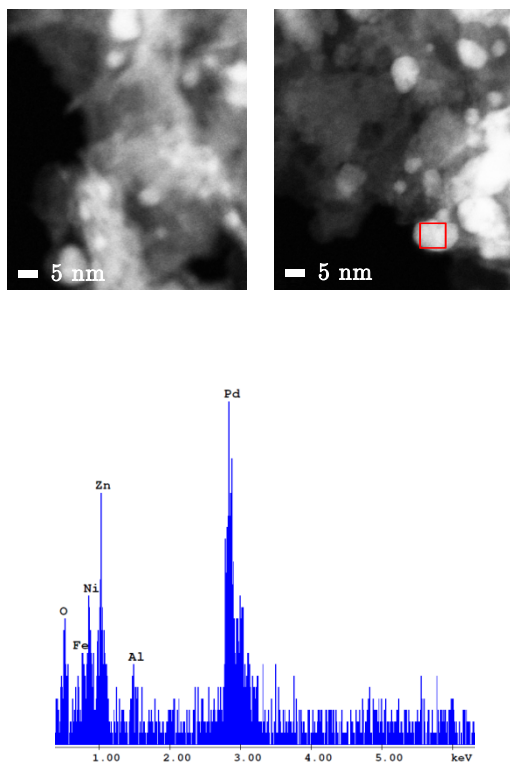


Figure 4.4: (Top) HAADF-STEM images of the catalyst surface with Pd nanoparticles dispersed on $\text{Al}_2\text{O}_3/\text{ZnO}$. (Bottom) Section of EDX spectrum recorded at the inspection field marked with the red box.

4.3.2 Mass transport resistances

In order to characterize quantitatively the G-L and L-S mass transport resistances, the criteria proposed in literature [65],[66] were used.

The theoretical calculation of G-L and L-S mass transfer coefficients k_{LA} and k_{SAS} has been extensively described in Chapter 2. The catalyst particles were approximated as spherical, according to the particle size distribution by weight basis (see Table 4.1).

Carberry numbers (defined in the previous chapter) calculated for all the experimental runs indicated the absence of any external mass-transfer resistance [80].

The absence of microporosity, confirmed by BET analysis, justifies the lack of internal L-S diffusion limitations.

The initial reaction rate was found to vary linearly with the catalyst loading in the investigated range of temperature as depicted in Figure 4.5. This trend was considered an additional verification that the reaction is under kinetic control.

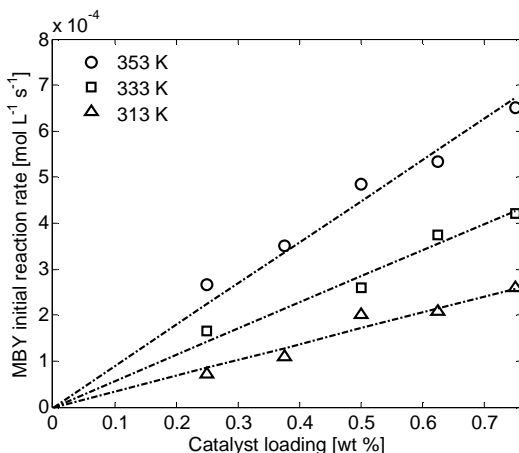


Figure 4.5: Effect of catalyst loading on the initial rate of MBY hydrogenation. Conditions: 7.0 bar.

4.3.3 Hydrogenation of MBY

During this study, 14 runs on MBY hydrogenation were carried out in a variety of experimental conditions. For each experiment, approximately 10 concentration data points at different reaction times were recorded. Some examples of experimental concentration profiles are shown in Figure 4.6 and Figure 4.7.

The proposed results show that, over the Pd/ZnO catalyst, MBE is hydrogenated with reaction rate significantly lower than MBY. Over the Lindlar catalyst, on the other hand, comparable hydrogenation rates were previously obtained for MBY and MBE (see Chapter 2). This tendency results into a higher selectivity of the process conducted over the Pd/ZnO catalyst.

Figure 4.8 shows the effect of pressure on the concentration of MBY, MBE and MBA at 353 K. Beyond increasing the hydrogenation rate of MBY, the pressure also promotes the overhydrogenation to MBA, resulting in a lower selectivity of the process.

In Figure 4.9 and Figure 4.10 the selectivity profile to MBE over the Pd/ZnO is compared with the one obtained with the Lindlar catalyst under the same experimental conditions and the same palladium loading. In both cases the Pd/ZnO exhibits a higher selectivity in the whole range of conversions.

More details about this selectivity increase will be provided in the next chapter.

The reaction carried out at 333 K and 7.0 bar using the commercial Lindlar catalyst showed a lower initial activity of $0.9 \text{ mol mol}_{\text{Pd}}^{-1} \text{ s}^{-1}$ compared with the $3.0 \text{ mol mol}_{\text{Pd}}^{-1} \text{ s}^{-1}$ of the Pd/ZnO catalyst. Similar trends were obtained during previous studies on the hydrogenation of MBY over Lindlar and Pd/ZnO catalysts [32][73]. The higher activity may be ascribed to the presence of the Pd-Zn alloy in the active phase of the catalyst suppressing the overhydrogenation of MBE to MBA.

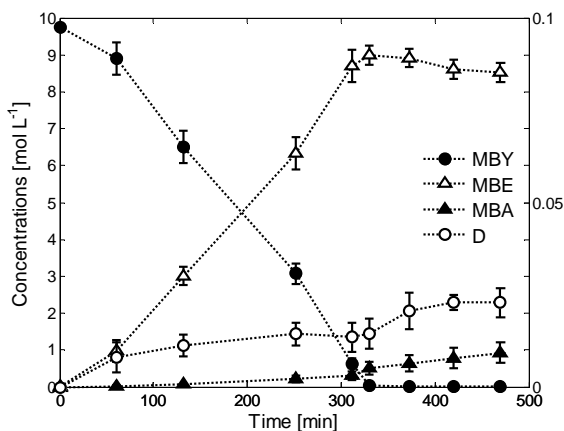


Figure 4.6: Experimental concentration profiles during the hydrogenation of MBY over a Pd/ZnO catalyst in a slurry reactor. Conditions: 333 K, 7.0 bar, 0.75 wt % of catalyst.

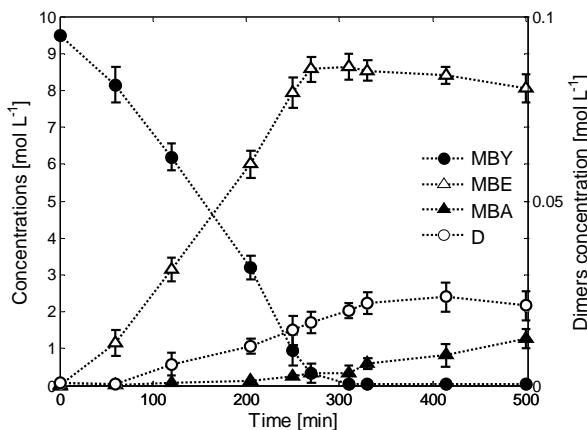


Figure 4.7: Experimental concentration profiles during the hydrogenation of MBY over a Pd/ZnO catalyst in a slurry reactor. Conditions: 353 K, 7.0 bar, 0.50 wt % of catalyst.

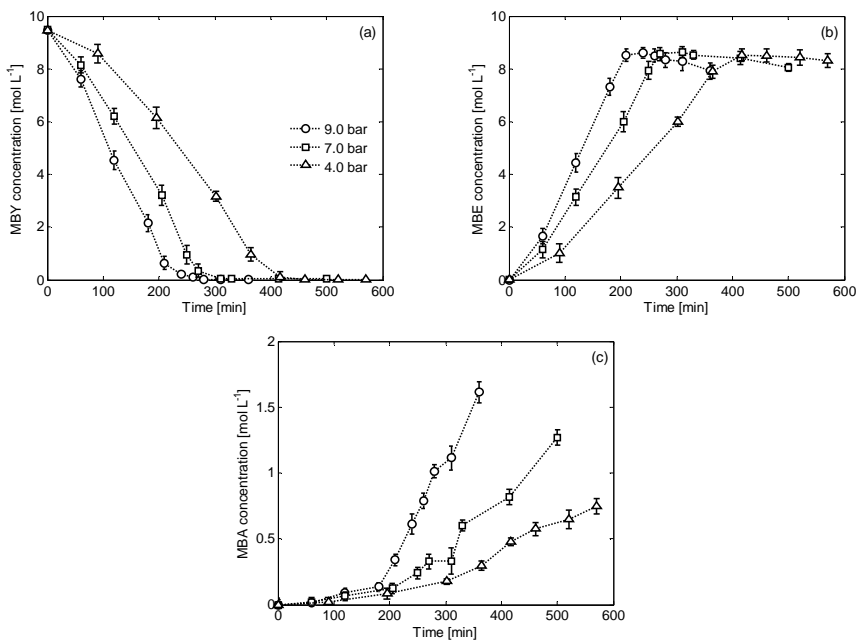


Figure 4.8: Effect of pressure on MBY hydrogenation. MBY (a), MBE (b) and MBA (c) experimental concentrations. Conditions: 353 K, 0.50 wt % of catalyst.

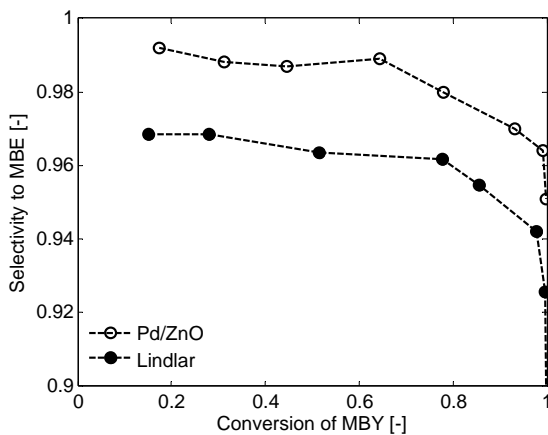


Figure 4.9: Selectivity to MBE vs MBY conversion during the hydrogenation of MBY over Pd/ZnO and Lindlar catalyst. Conditions: 333 K, 7.0 bar, $1.1 \cdot 10^{-3}$ wt % of Pd.

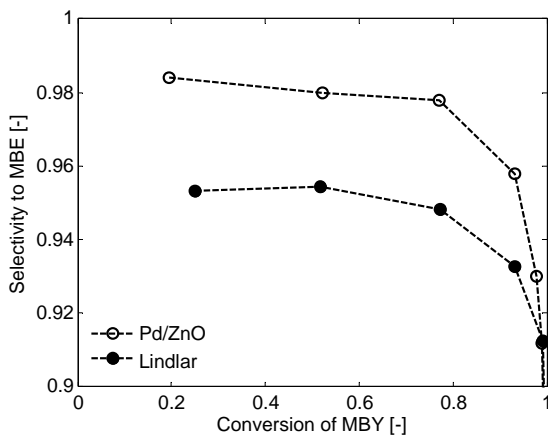


Figure 4.10: Selectivity to MBE vs MBY conversion during the hydrogenation of MBY over Pd/ZnO and Lindlar catalyst. Conditions: 353 K, 9.0 bar, $1.1 \cdot 10^{-3}$ wt % of Pd.

4.3.4 Hydrogenation of DIP

Figure 4.11 shows the representative concentration profiles during the hydrogenation of DIP over the Pd/ZnO catalyst. This figure can be directly compared to Figure 4.7 previously reported for the hydrogenation of MBY. It is evident that the catalyst does not inhibit significantly the overhydrogenation to HIP resulting in a very high concentration of this compound before the complete depletion of DIP.

The effect of pressure on the concentrations of DIP, IP and HIP is depicted at 353 K in Figure 4.12. The low maximum concentrations of IP are an additional indication of the poor inhibition effect of the catalyst on the overhydrogenation process.

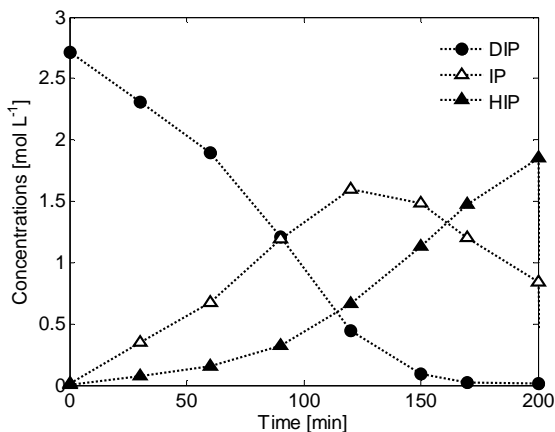


Figure 4.11: Experimental concentration profiles during the hydrogenation of DIP over a Pd/ZnO catalyst in a slurry reactor. Conditions: 353 K, 7.0 bar, 0.50 wt % of catalyst.

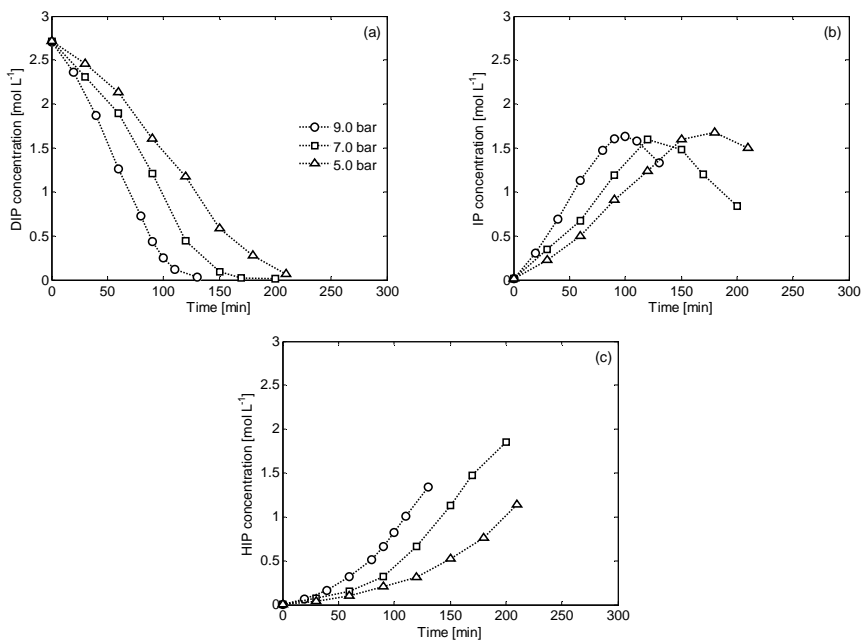


Figure 4.12: Effect of pressure on DIP hydrogenation. DIP (a), IP (b) and HIP (c) experimental concentrations. Conditions: 353 K, 0.50 wt % of catalyst.

The selectivity to MBE and IP over the Pd/ZnO catalyst are directly compared in Figure 4.13 under the same set of operating conditions. These results confirm that the selectivity of the hydrogenation process is strongly dependent on the hydrocarbon chain length.

It is worth noting that, according to literature, the alkyl chain of the alkynol molecule can also physically adsorb on the catalyst active sites through Van der Waals forces. The impact of this weak adsorption is proportional to the hydrocarbon chain length [81]. As consequence, the adsorption constant ratio alkynol/alkenol decreases for molecules with longer hydrocarbon chain, resulting in a lower selectivity to the corresponding alkenol. This is in good agreement with the values of K_Y/K_E and K_{DIP}/K_{IP} experimentally estimated during the previous investigations over the Lindlar catalyst.

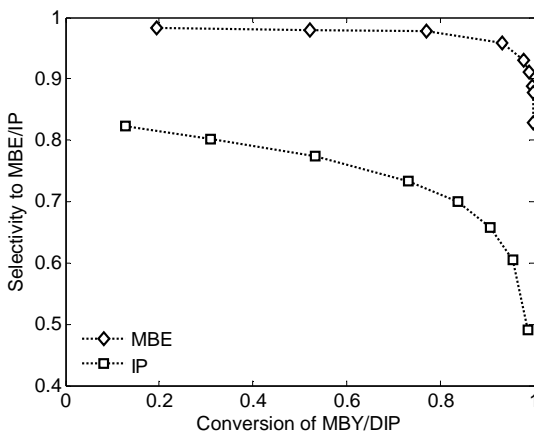


Figure 4.13: Selectivity to MBE and IP vs conversion of MBY and DIP over Pd/ZnO catalyst. Conditions: 353 K, 7.0 bar, 0.50 wt % of catalyst.

4.3.5 Catalyst reuse

The stability of the catalyst was evaluated performing MBY hydrogenation experiments over 6 consecutive reaction cycles. Between each run the catalyst was filtered, washed with isopropanol and dried. MBY initial reaction rate and selectivity to MBE for 6 consecutive runs conducted at 353 K and 7.0 bar are presented in Figure 4.14.

Both initial reaction rate and selectivity result constant over about 35 h of reaction. The high stability of the catalyst can be attributed to the strong interaction between Pd nanoparticles and ZnO leading to the formation of Pd-Zn alloy [61][32].

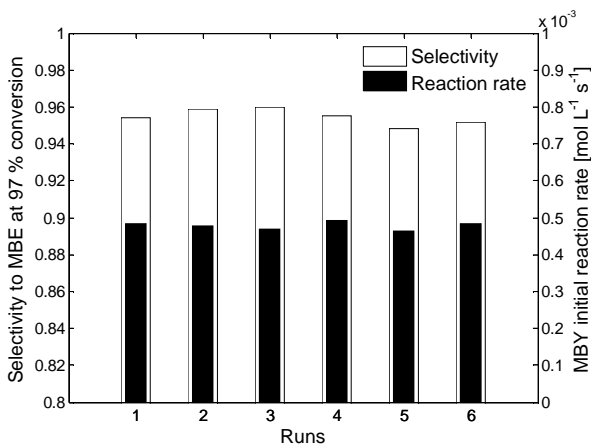


Figure 4.14: Selectivity to MBE at 97 % of conversion and MBY initial reaction rate for reactions over Pd/ZnO catalyst during consecutive runs. Conditions: 353 K, 7.0 bar, 0.50 wt % of catalyst.

4.3.6 Conclusions

A Pd-based catalyst was developed, characterized and tested in the hydrogenations of MBY under solvent free conditions. In contrast to the industrially used Lindlar catalyst, the new catalyst shows high activity and selectivity. The metal support was coated with a layer of

ZnO/Al₂O₃ and loaded with Pd. The characterization of the catalyst was conducted by FIB/SEM, STEM, EDX, TPO, TPR and BET.

External mass transfer limitations were studied in order to ensure the kinetic regime of the experimental runs. The high selectivity of the process to MBE was ascribed to the use of Zn acting as a promoter for selective hydrogenations. Both selectivity and initial reaction rate were found to be constant after catalyst reuse over about 35 h of reaction. For this reason, the Pd/ZnO catalyst seems to be suitable for continuous hydrogenation as well as a valuable alternative for the industrial hydrogenation of MBY with respect to commercial catalysts.

The catalyst exhibits higher selectivity during the hydrogenation of MBY as compared to the hydrogenation of DIP under the same reaction conditions. This difference in selectivity was ascribed to the physical adsorption of the molecules on the catalyst surface through Van der Waals forces, depending on the hydrocarbon chain length.

5 Alkyne hydrogenation in a structured reactor

5.1 Introduction

Industrially, alkyne hydrogenations for vitamin production are traditionally carried out in batch-wise operated slurry reactors under mild operating conditions [19]. Fine catalyst particles are used to avoid mass transfer limitations and to attain high product yield [59][82]. However, the handling of the catalyst and its separation after the reaction can strongly limit the efficiency of the process [83][84][85].

Packed-bed reactors are preferred for product and catalyst separation. In this case, low fluid velocities and large catalyst particles are necessary in order to limit excessive pressure drops, resulting in strongly mass transfer limited regimes [84]. Furthermore, randomly packed beds can give rise to non-uniform flow and reactant distributions due to channelling effects leading to wide ranges of residence times and poor performances [85][26]. An additional source of inefficiency of these reactors is related to their poor heat transfer capabilities leading to localized hot spots formation [27][28]. Hot zones can form due to non-uniform catalyst packing or to limited heat transfer among the packing elements [86]. Excellent heat transfer properties are decisive for exothermic reactions like alkynes and more in particular MBY hydrogenation (reaction enthalpy of $-170 \text{ kJ} \cdot \text{mol}^{-1}$ [33]). The unavoidable formation of hot spots and the heat accumulation due to the poor radial transfer area of catalyst packings can dramati-

ically affect the selectivity of the process to MBE due to the series-parallel reaction network depicted in Figure 2.1.

To overcome these problems, considerable efforts have been made in the application of structured reactors for continuous catalytic hydrogenations [87][88][89]. Structured reactors are characterized by large void fractions ($> 80\%$) allowing chemical reactions to be conducted with high flowrates and low pressure drops, in contrast to conventional packed-bed reactors [90][30].

Recently, Semagina et al. proposed a microstructured support for the deposition of Pd nanoparticles consisting in laser sintered metal fibers [73]. The size of the fibers (diameter between 10 and 20 μm) ensures high porosity and excellent fluid-solid mass transfer. However, the random packing results in the typical drawbacks previously listed for the packed bed reactors. Furthermore, a microstructured packing limits the scale up of the process which is a fundamental step in the realization and optimization of industrial plants.

Another approach recently applied to continuous alkyne hydrogenations is the falling film microreactor [91]. In this system a liquid film is generated by pulling down the liquid phase on the reactor surface via gravitational forces. The low liquid film thickness results in a rapid heat transfer. On the other hand the diffusive phenomena between gas and liquid phase and the small gas-liquid contact area strongly limit the mass transfer properties of this system.

Catalytic membranes are also an alternative to the aforementioned technologies allowing distributed addition of reactants and simultaneous removal of products [92]. The lifetime and the regeneration capability of these systems still need further investigation.

Different strategies for macrosystems have been reported to support the catalyst nanoparticles in monolithic reactors [93]. In general this involves the deposition on the monolithic structure of a precursor base layer in order to improve the adhesion of the catalyst active phase. The use of a metallic structure offers some advantages to prevent the formation of hot-spots. A common type of macrostructured catalyst are based on metal foams with interconnected cells. Ashby et al. describe their different production methods with copper and aluminium proposed as conventional materials [94]. The pore size

of these structures, directly affecting the hydraulic diameter of the reactor, is in general in the range 5 to 100 μm .

Recently, Hutter *et al.* developed a stream-wise periodic structure consisting in the negative pattern of tetrahedral overlapping spheres [95]. The regularly shaped geometry is extremely favourable in prospect of scaling up a laboratory facility to an industrial-size reactor. Scaling-up the reactor would involve a merely multiplication of the geometric elements of the structure. An industrial reactor could be considered in principle as a large number of identical cells operated in series and/or parallel. Furthermore, the designed geometry facilitates computational modelling approaches allowing a deeper understanding of the fluid dynamics [95]. Figure 5.1 shows an exemplary laser sintered metal support with inner diameter of 14 mm.



Figure 5.1: Laser sintered metal structure with inner diameter of 14 mm. The outer wall was partly removed for visualization purposes.

The proposed designed structured reactor was extensively compared with literature data of packed beds showing lower pressure drops and similar dispersion coefficients [96]. A comparison of the structure with commercially available metal foams inserted into an empty tube showed a strongly enhanced (30 % higher) heat transfer rate [97]. This improvement was ascribed to the fixed connection of the structure to the wall of the tube.

Elias *et al.* [98] tested the use of designed structured reactors for the hydrogenation of MBY applying a plug flow model to describe the concentration profiles of MBY and MBE at 333 K and 6.0 bar. That study suffers from some limitations such as the low explored initial concentration of alkyne and the limited ranges of operating conditions. Mass transfer effects were reported to strongly limit the reaction efficiency preventing a direct study of the intrinsic kinetics of the process. Furthermore, the low rates of conversion did not allow studying extensively the effect of the operating conditions on the behaviour of the reacting system.

In Chapter 2 a general mathematical model was proposed to describe the hydrogenation of MBY in a stirred slurry reactor, in the typical operating ranges of industrial reactors. In the present chapter the aforementioned model is applied to predict the kinetic behaviour of the hydrogenation of MBY in flow over a structured reactor coated with Pd on a ZnO/Al₂O₃ base layer.

A detailed set of kinetic and adsorption parameters has been estimated using experiments collected in the kinetic regime at different temperatures. The extension of the model to a mass transfer limited regime allowed the determination of the overall mass transfer coefficient under reacting conditions.

5.2 Experimental

5.2.1 Structured reactor

The structured reactor (inner diameter = 14 mm, length = 200 mm) was manufactured by selective laser sintering. The packing represents the negative pattern of tetrahedrally arranged overlapping spheres with diameter of 2.9 mm resulting in a porosity of 87 %. The interior geometry of the support structure was previously described in detail [95]. The full geometrical structure and the unit cell are depicted in Figure 5.2.

It is worth noting that the laser sintering technique used to produce this structure allows to design three-dimensional metal supports of nearly any shape.

The reactor was subjected to a thermal pre-treatment at 723 K for 3 h and coated at DSM Nutritional Products with an $\text{Al}_2\text{O}_3/\text{ZnO}$ base layer following an experimental procedure similar to the one previously presented for the powdered catalyst and reported below.

A precursor solution was obtained adding $\text{Al}(\text{NO}_3)_3 \cdot 9\text{H}_2\text{O}$ (200 g) in water (700 mL) and heating to 368 K. ZnO (43.4 g) was slowly added under stirring until complete dissolution. The solution was then cooled to ambient temperature and filtered through a 0.45 μm membrane filter. The deposition of $\text{Al}_2\text{O}_3/\text{ZnO}$ was performed by rinsing the inside of the reactor with 50 mL of the precursor solution. The reactor was then dried at 333 K and 125 mbar for 2 h and calcinated at 723 K for 1 h. This procedure was repeated 8 times.

Sodium molybdate dehydrate (79.5 mg) and anhydrous palladium(II)chloride (54.2 mg) were added to 30 mL of Millipore water. The solution was slowly evaporated under stirring until a solid residue was formed. Additional 30 mL of Millipore water were added to the solid residue. The evaporation-dissolving cycle was repeated two times in order to completely dissolve the palladium salt. 50 mL of hot water were added to the solid residue. The deep brown solution was cooled to room temperature and filtrated through a paper filter. The final volume was adjusted to 60 mL. The $\text{Pd}(0)$ suspension was obtained by bubbling hydrogen through the precursor solution for 1 h at room temperature. One end of the reactor was sealed with a rubber stopper and it was mounted in vertical position. The reactor was filled with 21 mL of the $\text{Pd}(0)$ suspension and the liquid was slowly evaporated at 363 K and 125 mbar. The same procedure was repeated sealing the opposite end of the reactor. This process was repeated three times. The structure was finally subjected to a thermal activation at 573 K for 4 h (temperature ramp: 10 K min^{-1}) under H_2/Ar flow (1:9; total flowrate: 450 mL min^{-1}). Palladium, Al_2O_3 and ZnO loadings were calculated by weighting the structure during the preparation procedure. The main features of the structured reactor are listed in Table 5.1.

After testing, the structured reactor was sectioned in small pieces (length = 10 mm) and observed by SEM (Zeiss NVision 40) equipped with EDX apparatus for characterization purposes. The SEM was operated at an acceleration voltage of 12 kV applying an in-lens secondary electron (SE). Pulse CO chemisorption was performed at 323 K with a 5 vol. % CO/He flow on a section of the inner part of the structured reactor (diameter = 5 mm, length = 10 mm). Before the measurement the sample was reduced at 723 K under flowing 5 vol. % H₂/Ar. The palladium dispersion was calculated considering an adsorption stoichiometry of Pd/CO = 2 [45].

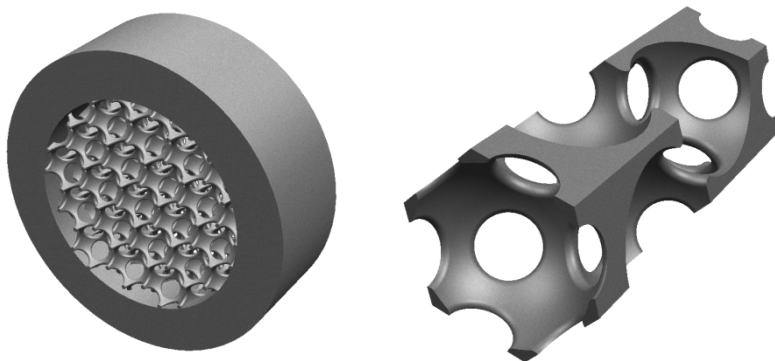


Figure 5.2: Left: Auxiliary view of the porous structure. Right: unit cell of the porous structure. Adapted from [99].

Table 5.1: Structured reactor characteristics.

Parameter	Units	Value
Length	m	0.2
Inner diameter	m	$1.4 \cdot 10^{-2}$
Cell diameter	m	$2.9 \cdot 10^{-3}$
Structure volume	m^3	$4.0 \cdot 10^{-6}$
Porosity	-	0.87
Specific surface area	m^{-1}	1122
Pores size	m	$9.2 \cdot 10^{-4}$
Hydraulic diameter	m	$3.1 \cdot 10^{-3}$
Pd loading	$\text{kg}_{\text{Pd}} \text{m}^{-3}$	8.5
<i>Coating layer composition</i>		
Pd	wt %	1.2
ZnO	wt %	44.3
Al_2O_3	wt %	54.5

5.2.2 Experimental setup

The experiments were conducted in a semi-batch reaction system which main components are sketched in Figure 5.3.

Batch experiments were conducted with respect to the liquid phase, continuously circulated through the loop. Pure hydrogen was continuously fed to the system. The hydrogen and the liquid mixture passed through the structured reactor in cocurrent upflow. All experiments were conducted charging the plant with 650 g of pure MBY. A membrane pump (Hydracell, Verder) was used to recirculate the liquid mixture from the separator to the reactor. The liquid recirculation rate and the hydrogen flowrate were regulated by mass flow controllers (Coriflow and EL, Bronkhorst respectively). A high liquid flowrate of 70 kg h^{-1} was selected in order to minimize the external L-S concentration gradient in the structured reactor. A static mixer (diameter = 7 mm, length = 200 m), consisting in a porous structure similar to the reactor, was installed before the reactor in order to improve the G-L mass transfer.

The two phase flow was observed through a view cell installed at the reactor inlet.

The liquid mixture was heated to the desired reaction temperature by means of a block of brass equipped with two heating cartridges (400 or 250 W depending on the operating temperature). The temperature was controlled at the outlet of the heater with a PID temperature controller and measured at the reactor inlet and outlet. The structured reactor was thermally insulated to minimize heat losses.

A back pressure regulator, located downstream of the structured reactor, (Flowsolve) controlled the pressure at the reactor inlet. An additional pressure sensor was located at the reactor outlet to gain information about the pressure drop in the structure.

The off-gas was separated from the liquid and cooled down with cooling water to condense eventual organic vapours recollected in the G-L separator. Although the off-gas could be fed back into the reactor, for ease of operation this was not done.

Before starting an experiment, the liquid was recirculated through the system in order to stabilize the temperature and the pressure to the required levels. As soon as the hydrogen was supplied to the reactor, the reaction time was initialized to zero.

Temperature and pressure of the reactor were considered constant along the reactor axis due to the small measured differences between reactor inlet and outlet (< 1 K and < 0.3 bar). At 70 kg h^{-1} the estimated conversion of MBY per pass was lower than 0.5 %. Therefore it is reasonable to assume that the bulk liquid phase concentrations were uniform throughout the whole loop depicted in Figure 5.3. After each experiment the setup was emptied and flushed by nitrogen.

Liquid samples were withdrawn at defined intervals of time through a manual valve and analysed by gas-chromatography following the procedure described in Chapter 2.

The total liquid removed during each run for analysis never exceeded 8 % of the initial liquid volume. Hence, the liquid-to-catalyst ratio was considered constant during the experiments.

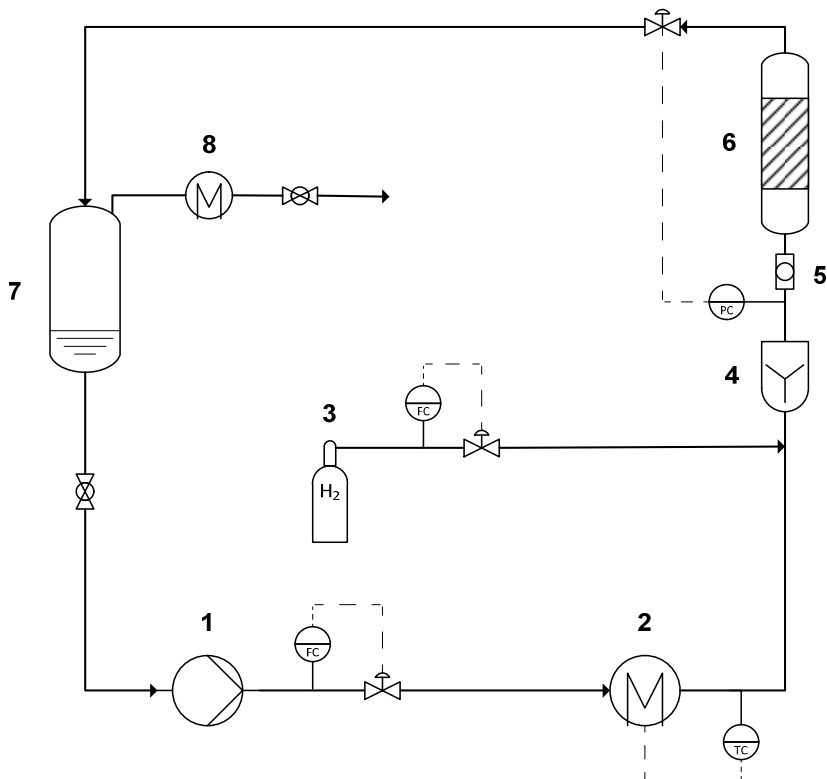


Figure 5.3: Simplified scheme of the experimental setup for semi-batch operation mode. (1) recirculation pump, (2) electrical heater, (3) hydrogen tank, (4) static mixer, (5) view cell, (6) structured reactor, (7) gas-liquid separator, (8) off-gas cooler.

5.3 Results

5.3.1 Reactor characterization

The homogeneity and the quality of the active coating of the structure, were verified by SEM analysis. SEM microphotographs of the structured catalyst cross section and of a fracture of the coating layer are shown in Figure 5.4. The metal support appears to be coated with an homogenous base layer with an estimated thickness between 4 and 7 μm (measured in different parts of the structure). The layer remains intact after high temperature treatment and hydrogenation testing.

The element mapping of the structured reactor obtained by EDX is presented in Figure 5.5 and Figure 5.6 showing coloured pixels corresponding to zinc (yellow), aluminium (pink), palladium (dark blue) and iron (blue). Tabulated semi-quantitative EDX data are reported in Figure 5.7 for different sampling areas of the structured reactor.

An intense signal of palladium is observed on the external surface of the catalyst. Aluminum and zinc signals clearly overlap on the cross section of the coating layer. Traces of zinc and aluminum are also detected on the external surface of the core support showing substantial adherence of the base layer. This strong adherence can be attributed to the formation of mixed oxides between ZnO and the metal support [73].

Iron appears to be one of the main components of the metal support together with nickel, molybdenum and cobalt.

The presence of palladium particles is almost completely restricted to the external surface of the reactor.

CO chemisorption indicated a low palladium dispersion (2.4 %). The BET analysis previously proposed on a Pd/ZnO powdered catalyst, synthesized with a similar procedure, showed a complete absence of microporosity (see Section 4.2.2) . This suggested to neglect any internal L-S diffusion limitation during the analysis of reaction data.

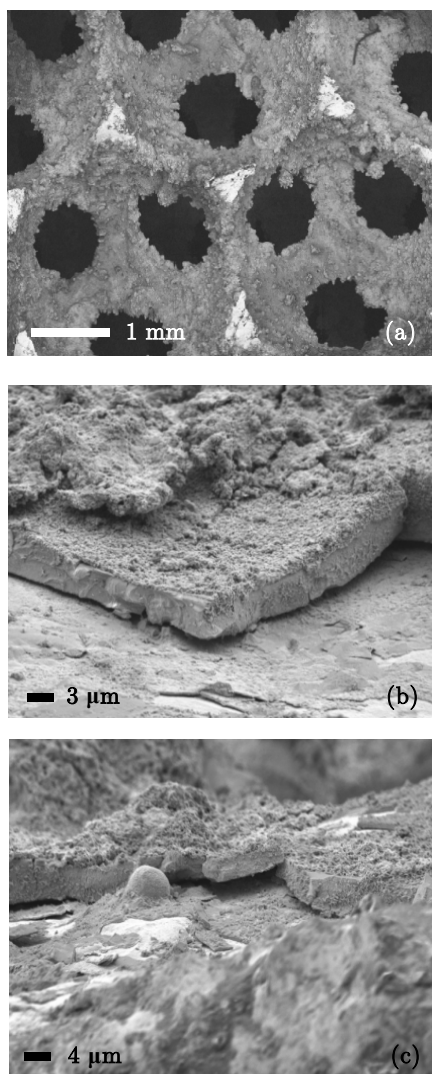


Figure 5.4: SEM microphotograph of the structured catalyst. Detector: In-lens, voltage: 12 kV. (a) Detail of the porous structure cross section. (b)(c) Magnified images of fractures of the coating layer.

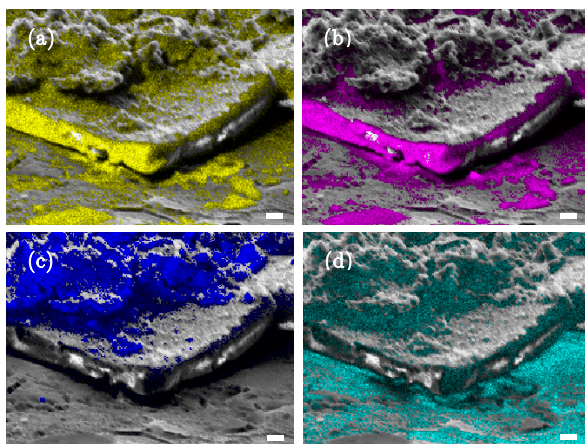


Figure 5.5: Element mapping of zinc (yellow), aluminum (pink), palladium (dark blue) and iron (blue) of the image in Figure 5.4 (b). The scale bar is 3 μm .

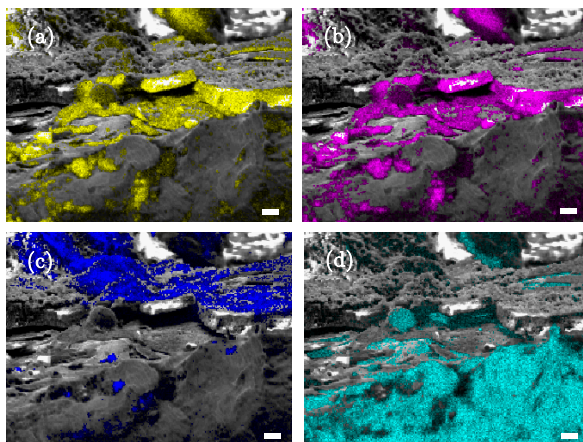
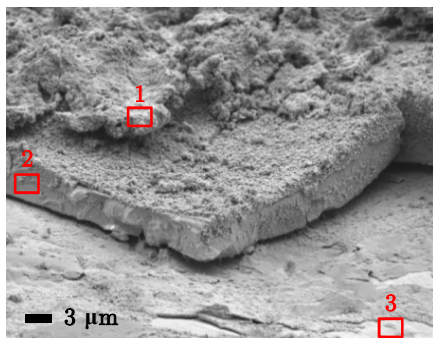
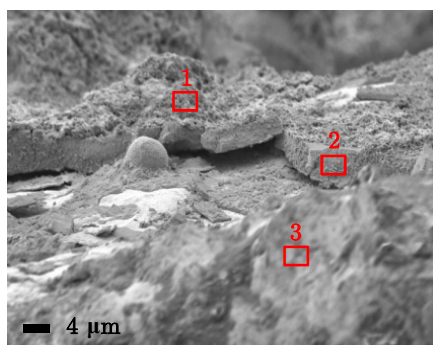


Figure 5.6: Element mapping of zinc (yellow), aluminum (pink), palladium (dark blue) and iron (blue) of the image in Figure 5.4 (c). The scale bar is 3 μm .



Element	wt %		
	1	2	3
C	9.2	6.7	5.5
O	2.6	5.6	-
Ni	-	1.0	23.3
Zn	14.1	34.9	2.4
Al	1.3	29.5	1.0
Mo	4.8	3.8	5.7
Pd	35.0	-	1.2
Fe	27.9	18.5	53.4
Co	2.2	-	6.0
Other	2.9	-	1.5



Element	wt %		
	1	2	3
C	12.7	15.5	1.0
O	1.9	4.9	-
Ni	6.7	2.0	17.7
Zn	10.4	32.9	-
Al	4.0	21.5	-
Mo	5.8	4.3	5.2
Pd	41.1	-	-
Fe	12.8	14.7	68.8
Co	2.5	2.2	5.1
Other	2.1	2.0	2.2

Figure 5.7: EDX analysis of different sampling areas of Figure 5.4 (b) and (c) marked with red boxes.

5.3.2 Analysis of initial rate data

The hydrogenation rate of MBY is constant during the reaction at low conversions [57]. Thus, an initial reaction rate can be calculated according to the MBY concentration decrease at conversions lower than 30 %.

Figure 5.8 presents the initial rate of MBY hydrogenation at various hydrogen flowrates in the investigated range of temperatures. The initial reaction rate significantly increases with hydrogen flowrate in the range 0.1 – 0.5 NL min⁻¹ indicating a non-negligible mass transfer effect.

The almost constant trend at higher flowrates (0.6 – 0.8 NL min⁻¹) suggests that the reaction is under kinetic control. Thus, Figure 5.8 can be divided into two regions depending on the hydrogen flowrate. The experimental results obtained during the runs at high flowrates were simultaneously used in a single optimization procedure to estimate the kinetic and adsorption parameters governing the process. In a second stage these best-estimated parameters allowed the modelling of the experimental results acquired in the mass transfer limited regime. As result of this procedure, the overall mass transfer coefficient of hydrogen from the G-L interface to the surface of the catalyst was estimated.

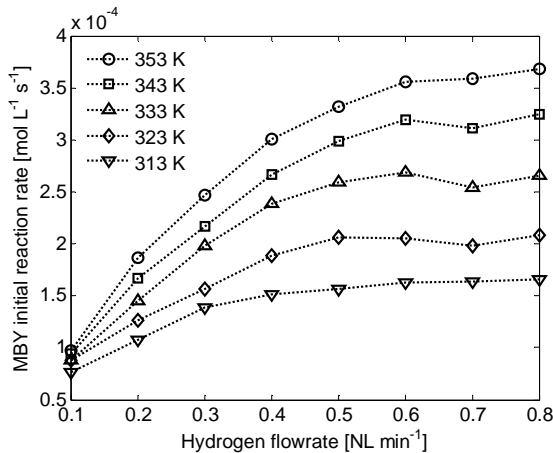


Figure 5.8: Effect of hydrogen flowrate on the initial rate of MBY hydrogenation. Pressure: 4.0 bar, Liquid flowrate: 70 kg h⁻¹.

5.3.3 Kinetic model

The kinetic mechanism developed for the hydrogenation of MBY over the Lindlar catalyst and reported in Chapter 2 was proposed to simulate the experimental results obtained using the structured reactor.

The main hypothesis of the mechanism are listed below:

- (i) All adsorption/desorption steps are assumed to be fast enough to remain equilibrated.
- (ii) The last hydrogen additions for production of MBE, MBA and dimers are considered to be the rate determining steps.
- (iii) Low coverages for the intermediate species R_x , P_x and Q_x are assumed in the mass balances for the catalyst active sites.
- (iv) The terms $K_A C_A$, $K_D C_D$, $K_H C_H$ are neglected in the denominator of the final kinetic expressions.

The experimental data showed a less evident negative order of MBY hydrogenation compared to the one obtained over the Lindlar catalyst. For this reason, the model presented in Section 2.3.5 was additionally simplified by neglecting the term $K_\phi C_Y$. Thus, the following hydrogenation rates were considered:

$$r_1 = k_1 \frac{K_Y C_Y K_H C_H}{1 + K_Y C_Y + K_E C_E} \quad (5.1)$$

$$r_2 = k_2 \frac{K_E C_E K_H C_H}{1 + K_Y C_Y + K_E C_E} \quad (5.2)$$

$$r_3 = k_3 \frac{K_Y C_Y^2 K_H^2 C_H^2}{1 + K_Y C_Y + K_E C_E} \quad (5.3)$$

where k_i are the apparent kinetic constants for the three hydrogenations involved in the process.

The loop in Figure 5.3 behaves like a stirred batch reactor with respect to the liquid phase operating at constant temperature and pressure. This hypothesis is justified by low conversion per pass and small temperature and pressure differences between reactor inlet and outlet. Under this assumption the mole balances in the liquid phase on the five species involved in the system can be expressed in the kinetic regime by the following set of differential and algebraic equations:

$$\frac{dC_Y}{dt} = \frac{n_{Pd}}{V_L} (-r_1 - 2r_3) \quad (5.4)$$

$$\frac{dC_E}{dt} = \frac{n_{Pd}}{V_L} (r_1 - r_2) \quad (5.5)$$

$$\frac{dC_A}{dt} = \frac{n_{Pd}}{V_L} r_2 \quad (5.6)$$

$$\frac{dC_D}{dt} = \frac{n_{Pd}}{V_L} r_3 \quad (5.7)$$

$$C_H = C_H^* \quad (5.8)$$

Eq. (5.8) results from the hypothesis of absence of external mass transfer resistances. Thus, the hydrogen concentration in the liquid

phase can be considered equal to its equilibrium value at the operating temperature and pressure calculated using Eq (2.13).

The kinetic and adsorption constants k_i and K_i were assumed to obey an Arrhenius-type temperature dependency, according to Eq. (2.46) and (2.47).

The proposed mathematical model was numerically integrated to minimize the objective function $\varphi(\Theta)$ following the procedure described in Section 2.3.6. The values of the kinetic parameters listed in Table 2.5 for the Lindlar catalyst were used as initial attempts during the optimization procedure.

Some examples of calculated (continuous lines) and experimental (symbols) concentration profiles are shown in Figure 5.9 at hydrogen flowrate of $0.7 \text{ NL min}^{-1}[100]$.

The obtained results show a good agreement between calculated and experimental kinetic profiles. However, it is worth mentioning that the proposed model results intrinsically limited by its empirical nature. Thus, its validity is restricted to the operating conditions for which it has been developed.

The model satisfactorily predicts the concentration profiles also on a quantitative basis as confirmed by the overall percentage standard deviations reported in Table 5.2.

The estimated values for the unknown parameters are reported in Table 5.3 along with their 95 % confidence intervals.

The activation energies of MBY and MBE hydrogenation (E_1 , E_2) agree with the values of $25.2 \pm 1.6 \text{ kJ mol}^{-1}$ [32] and $32.6 \pm 2.4 \text{ kJ mol}^{-1}$ [101] respectively reported in literature. It is worth noting that the ratio $E_2/E_1 > 1$ makes the kinetic constant of the undesired hydrogenation r_2 more sensitive than the one of r_1 to the temperature increase. According to the thermodynamics of alkyne and alkene hydrogenation, the high selectivity to the olefinic product is due to the stronger adsorption of the alkyne compared to the alkene and not to its higher kinetic constant. This is confirmed by the ratio k_2/k_1 ranging between 1.6 and 2.8 depending on the investigated temperatures. The enthalpies of adsorption $-\Delta H_Y$ and $-\Delta H_E$ are lower than 30 kJ mol^{-1} in good agreement with the values reported in literature for similar alkynes and alkenes[32][51].

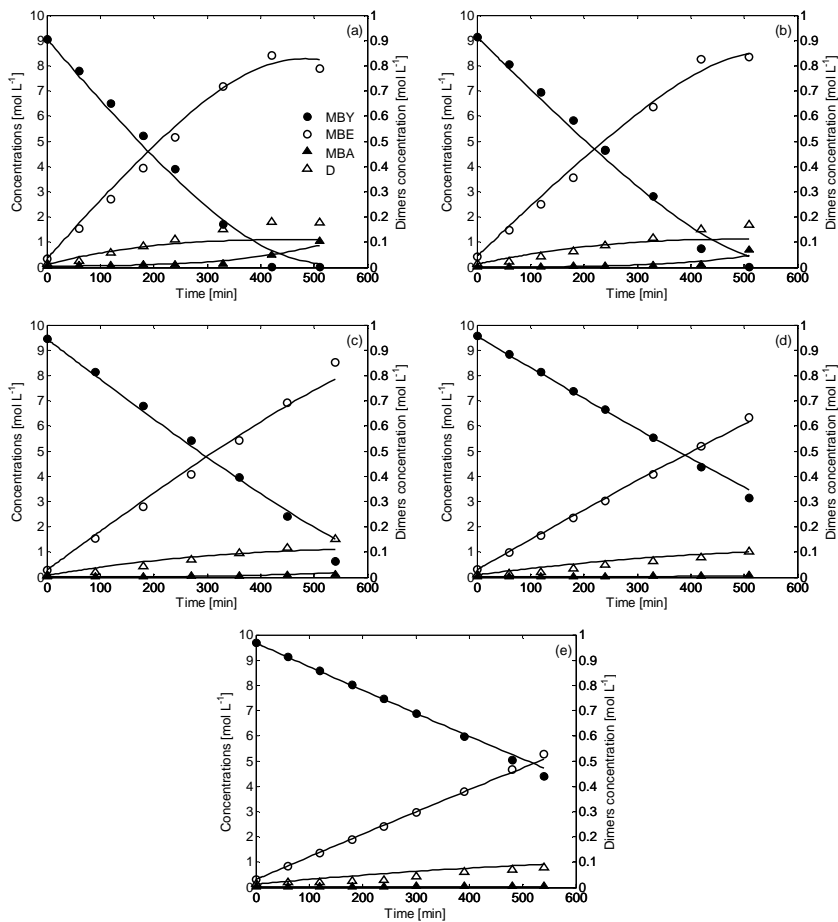


Figure 5.9: Experimental points and calculated kinetic curves of MBY, MBE, MBA (left axis) and dimers (right axis). Temperature: 353 K (a), 343 K (b), 333 K (c), 323 K (d), 313 K (e), pressure: 4.0 bar, liquid flowrate: 70 kg h^{-1} , hydrogen flowrate: 0.7 NL min^{-1} .

Table 5.2: Overall percentage standard deviations for the experimental runs depicted in Figure 5.9.

Run	σ [%]
a	14.8
b	13.9
c	14.8
d	5.8
e	7.9

Table 5.3: Kinetic parameter estimates with 95 % confidence intervals.

k_{01} [mol(mol _{Pd} s) ⁻¹]	$(9.1 \pm 0.4) \cdot 10^6$	E_1 [kJ mol ⁻¹]	26.2 ± 1.3
k_{02} [mol(mol _{Pd} s) ⁻¹]	$(1.4 \pm 0.1) \cdot 10^9$	E_2 [kJ mol ⁻¹]	37.9 ± 1.8
k_{03} [L(mol _{Pd} s) ⁻¹]	$(4.8 \pm 0.7) \cdot 10^{10}$	E_3 [kJ mol ⁻¹]	28.1 ± 1.4
K_{0Y} [L mol ⁻¹]	$(9.0 \pm 1.1) \cdot 10^{-5}$	$-\Delta H_Y$ [kJ mol ⁻¹]	26.9 ± 1.4
K_{0E} [L mol ⁻¹]	$(1.9 \pm 0.2) \cdot 10^{-5}$	$-\Delta H_E$ [kJ mol ⁻¹]	18.0 ± 1.0
K_{0H} [L mol ⁻¹]	$(1.6 \pm 0.1) \cdot 10^{-2}$	$-\Delta H_H$ [kJ mol ⁻¹]	5.1 ± 0.2

The ratio K_Y/K_E ranges between 98 and 145 for temperatures between 313 and 353 K as reported in literature for common alkyne/alkene systems [12]. This value is $\sim 40\%$ higher than the corresponding one previously reported for the Lindlar catalyst (see Section 2.3.6).

In accordance with published data, the formation of a Pd-Zn alloy can change the adsorption strength of alkynes and alkenes affecting the selectivity of the hydrogenation [54][102]. The addition of Zn, in particular, is considered to be beneficial for the selectivity of the process towards the alkene [54]. It affects the electronic structure of Pd resulting in a decrease of the heat of adsorption of alkynes and alkenes [75][103]. As a result of the observed increase of the ratio K_Y/K_E , the selectivity of the process to MBE is significantly enhanced. This tendency was depicted in Chapter 4 where the selectivity of the process to MBE over the Pd/ZnO catalyst was compared with the one obtained with the Lindlar catalyst under the same experimental conditions. The selectivity drop with temperature at various conversions is depicted in Figure 5.10 in the range of temperature 313 – 353 K.

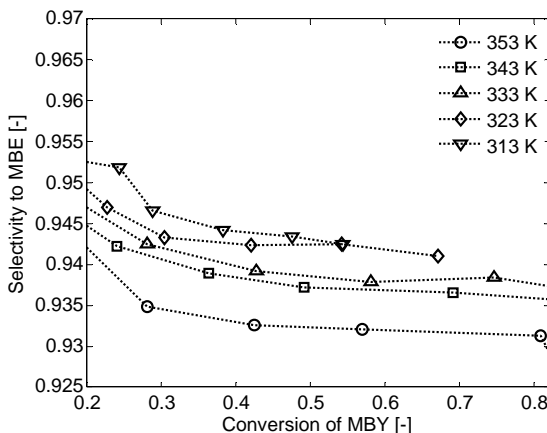


Figure 5.10: Effect of temperature on the selectivity to MBE. Pressure: 4.0 bar, liquid flowrate: 70 kg h⁻¹, hydrogen flowrate: 0.7 NL min⁻¹.

5.3.4 Mass transfer limited regime

The experimental runs under mass transfer controlled regime were simulated using the previously estimated set of kinetic parameters depicted in Table 5.3. The initial hydrogenation rates calculated during these experiments are depicted in Figure 5.8 at hydrogen flowrates varying between 0.1 and 0.5 NL min⁻¹.

Eq. (5.8) of the mathematical model was replaced by:

$$\frac{dC_H}{dt} = K_{ov}(C_H^* - C_H) - \frac{n_{Pd}}{V_L}(r_1 + r_2 + 2r_3) \quad (5.9)$$

G-L and L-S mass transfer steps can be considered in series. Thus, an overall mass transfer coefficient K_{ov} was defined as:

$$\frac{1}{K_{ov}} = \frac{1}{k_L a} + \frac{1}{k_S a_S} \quad (5.10)$$

This approach neglects the G-S mass transfer which is important only for large gas segments [104].

The same numerical optimization procedure used for the kinetic regime was implemented during this phase to estimate the only unknown parameter K_{ov} . The overall mass transfer coefficients were estimated by fitting the mathematical model to the experimental results obtained in the whole range of investigated temperatures. The effect of the temperature on K_{ov} was neglected during this study.

Figure 5.11 shows the simulated and experimental conversion profiles of MBY for different hydrogen flowrates at four investigated temperatures.

These figures confirm the reliability of the proposed model to predict the experimental results obtained under mass transfer limitation at hydrogen concentration lower than its solubility.

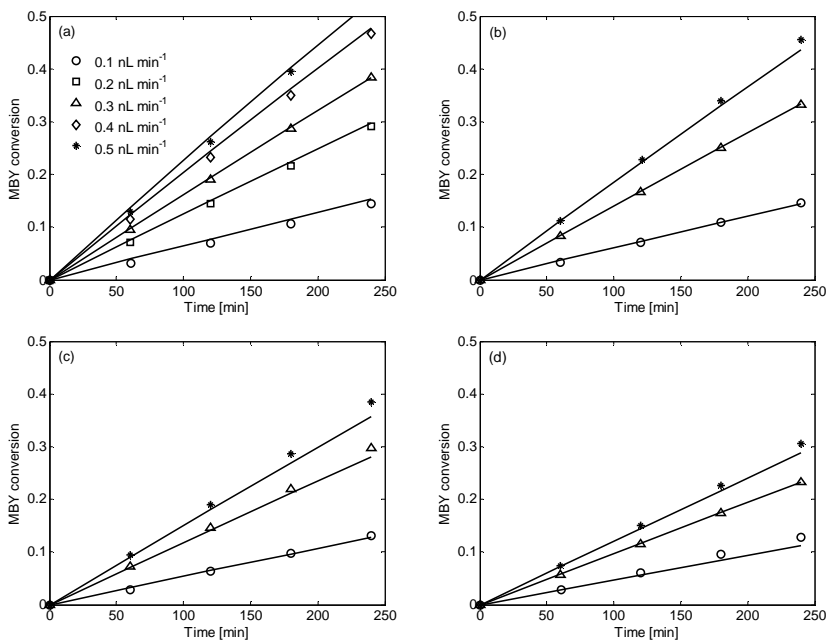


Figure 5.11: Effect of hydrogen flowrate on the conversion profiles of MBY: experimental (symbols) and calculated (continuous lines) conversions. Temperature: 353 K (a), 343 K (b), 333 K (c), 323 K (d). Pressure: 4.0 bar, Liquid flowrate: 70 kg h⁻¹.

The mass transfer coefficients resulting from the optimization procedure are depicted in Figure 5.12 together with their 95 % confidence intervals for different hydrogen flowrates. The error bars smaller than the symbols are not shown. Values lower than 0.25 s^{-1} were obtained in the mass transfer limited regime.

The increase of the mass transfer coefficient with hydrogen flowrate is related to the structural properties of the porous reactor. At high flowrates local turbulences are produced that improve the G-L-S mass transfer.

Assuming a controlling mass transfer resistance located on the liquid side [105], the overall mass transfer coefficient defined by Eq. (5.10) can be approximated to $k_L a$.

The following criteria, already introduced in Chapter 3 was used to identify the kinetic regime:

$$Ca^{GL} = \frac{r_H}{k_L a \cdot C_H^*} < 0.1 \quad (5.11)$$

The Carberry numbers calculated for the 25 experiments performed at low hydrogen flowrates ($0.1 - 0.5 \text{ NL min}^{-1}$) are depicted in Figure 5.13.

The threshold line at $Ca^{GL} = 0.1$ represents the criteria described by Eq. (5.11). Almost all the experimental results obtained in this operating range appear to be limited by mass transfer phenomena. However, limit values were obtained at 0.5 NL min^{-1} validating the hypothesis of absence of any external mass-transfer resistance for all the runs conducted at higher hydrogen flowrates ($0.6 - 0.8 \text{ NL min}^{-1}$).

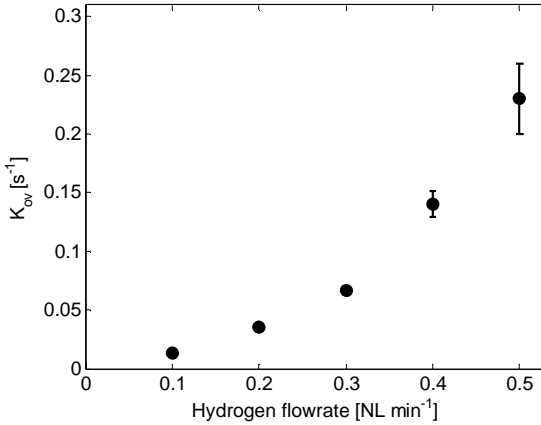


Figure 5.12: Effect of hydrogen flowrate on the overall mass transfer coefficient. Pressure: 4.0 bar, Liquid flowrate: 70 kg h⁻¹.

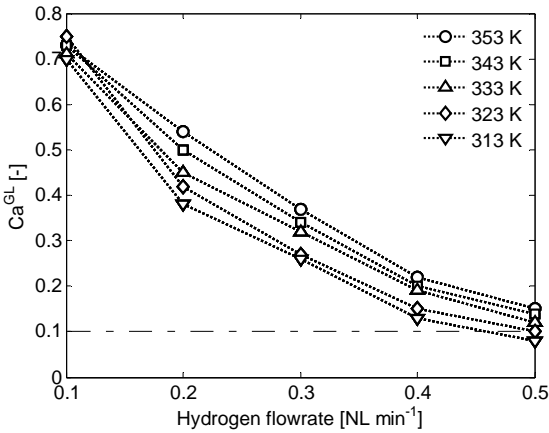


Figure 5.13: Effect of hydrogen flowrate on Carberry number Ca^{GL} . The threshold line at $Ca^{GL} = 0.1$ represents the criteria proposed in [65]. Pressure: 4.0 bar, Liquid flowrate: 70 kg h⁻¹.

5.3.5 Model validation

In order to validate the estimated parameters, further experiments were conducted at 343 K and 353 K, at additional operating pressure levels (2.0 and 6.0 bar). The mathematical model proposed for the kinetic regime and the set of estimated parameters were used without any further adjustment to simulate these experimental results. The comparison between experimental and calculated concentrations, result of this simulation, is shown in Figure 5.14.

In both cases the model can successfully describe the kinetic behaviour of the system with percentage standard deviations in line with the ones previously calculated during the optimization procedure. Figure 5.15 shows the influence of pressure on MBY hydrogenation rate. The continuous lines at 2.0 and 6.0 bar were obtained during the validation procedure. An increase in operating pressure leads to an increase in hydrogen solubility according to Eq. (2.13) and consequently in a higher reaction rate.

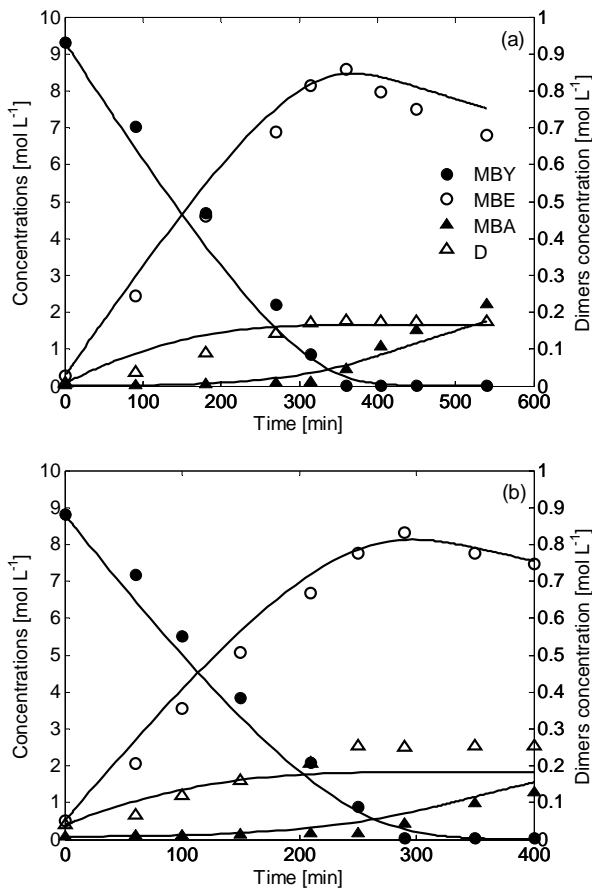


Figure 5.14: Comparison between experimental and simulated kinetic curves. Temperature: 343 K (a), 353 K (b). Pressure: 6.0 bar, Liquid flowrate: 70 kg h⁻¹, Hydrogen flowrate: 0.7 NL min⁻¹.

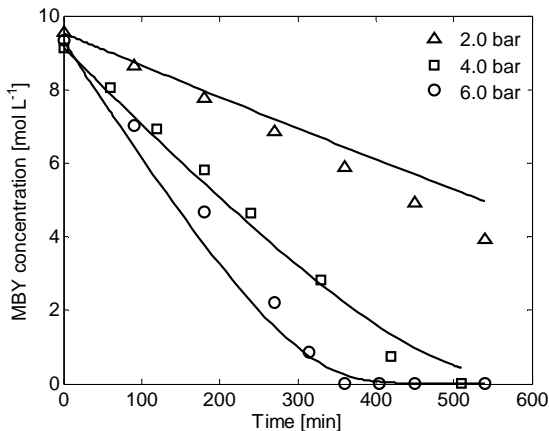


Figure 5.15: Comparison between experimental and simulated kinetic curves. Temperature: 343 K (a), 353 K (b). Pressure: 6.0 bar, Liquid flowrate: 70 kg h⁻¹, Hydrogen flowrate: 0.7 NL min⁻¹.

5.3.6 Catalyst reuse

The deactivation of the catalyst was studied by periodically testing a benchmark set of reaction conditions (343 K, 4.0 bar, liquid flowrate: 70 kg h⁻¹, hydrogen flowrate: 0.6 NL min⁻¹). A turnover frequency (TOF) of 34.5 s⁻¹ was calculated for the fresh structured reactor as:

$$TOF = 100 \frac{r_H \cdot V_L}{n_{Pd} \cdot \delta} \quad (5.12)$$

where δ is the palladium dispersion estimated by CO chemisorption.

After 270 h of operation, the TOF decreased of ~13 % compared to the original value. Thus, a window of 200 h of operation was selected before the thermal reactivation of the structured reactor with the procedure described in Section 5.2.1. Within this interval the TOF decrease was assumed to be lower than 10 % and for this reason neglected in the evaluation of the experimental results.

5.3.7 Conclusions

This chapter presents a study of the solvent-free hydrogenation of MBY in flow over a structured reactor consisting in a laser sintered metal support coated with a Pd/ZnO/Al₂O₃ based catalyst. The liquid phase was circulated through the reactor and hydrogen was continuously fed in cocurrent upflow.

The kinetics of the reaction were assumed to obey a Langmuir-Hinshelwood mechanism with non-competitive adsorption between hydrogen and organics and dissociative adsorption of hydrogen. A series of experiments was performed at varying temperatures and hydrogen flowrates. The runs conducted at high hydrogen flowrates (0.6 – 0.8 NL min⁻¹) did not show a significant dependence of the initial reaction rate on the hydrogen flowrate and were, for this reason, assumed to occur in absence of any mass transfer limitation.

The results of these experiments were used in an optimization procedure to estimate the kinetic and adsorption coefficients governing the process. These best-estimated values allowed the modelling of the behavior of the system at lower hydrogen flowrates (0.1 – 0.5 NL min⁻¹). The overall coefficient K_{ov} , describing the hydrogen mass transfer from the gas phase to the surface of the catalyst, was calculated by extending the model to the mass transfer limited regime. The reaction appears to be strongly dependent on the hydrogen flowrate with estimated K_{ov} ranging between 0.01 and 0.25 s⁻¹ at hydrogen flowrates between 0.1 and 0.5 NL min⁻¹. The occurrence of mass transfer limitations under these operating conditions was verified by using an empirical criteria.

The complete mathematical model is able to reliably estimate the concentrations profiles of the species involved in the system MBY, MBE, MBA and dimers in a range of temperatures (313 – 353 K) and hydrogen flowrates (0.1 – 0.8 NL min⁻¹). The accuracy of the optimization procedure was confirmed by the values of the overall standard deviations always lower than 15 %. The model was validated using the best estimated kinetic and adsorption parameters to simulate the concentration profiles of additional experiments not included in the pool used for the optimization at a different operating pressure level.

6 Continuous hydrogenation in a structured reactor

6.1 Introduction

As with many other branches of industry, the evolution of fine chemical and pharmaceutical manufacture includes the conversion of traditional batch processes into continuous operations.

The development of continuous manufacture receives since many years increasing interests from R&D and industrial sectors. Cost and quality considerations drive the transition from batch to continuous processing including smaller equipment, better process control and energy savings [107]. Batch processes are known to be less flexible, involving a number of discontinuous steps with the intermediate products being collected, stored and often transported to the other facilities.

In addition to more efficient processes, continuous manufacturing can also be considered safer, allowing access to hazardous chemistries in a controlled manner [108][109]. In continuous mode rather than batch processes, the chemical reactions generally can take advantage of smaller reactor volumes resulting in less material in the system. Exothermic reactions and particularly hydrogenations can be considered safer when continuously run because of the higher heat transfer resulting from a larger specific surface area. This was reported to be up to ~5 times higher for continuous stirred tank reactors and up to ~50 times higher for plug flow reactors compared to batch reactors [110].

Furthermore, reactions involving hazardous gas reagents like hydrogenations are safer because plug flow reactors can operate more than 97 % liquid filled resulting in small amounts of gas in the reactor compared to batch processes [110].

Industrially alkyne hydrogenations for vitamin production are traditionally carried out in batch-wise operated slurry reactors under mild operating conditions [19]. While fine catalyst particles are used in order to avoid mass transfer limitations and to obtain high product yield the smallest possible size of the particles is limited due to catalyst handling [59][82]. Solid charging, filtration processes and discharging can often create environmental and safety problems.

To overcome these drawbacks, considerable efforts are directed to the application of structured reactors for continuous processing of multiphase catalytic reactions.

In the previous chapter a designed structured reactor was proposed and characterized from chemical and kinetic point of view for the semi-batch hydrogenation of MBY, chosen as model reaction.

Previous studies conducted on this designed structure reactor concern a variety of fluid dynamic investigations such as bubble droplet size measurements [112][113][114], large eddy simulations [95] and particle image velocimetry [115] [116].

This chapter presents the continuous operation of the proposed structured reactor in the hydrogenation of MBY. A plug flow model was applied to describe the experimental results in terms of overall mass transfer coefficient at various temperatures, pressures, liquid and gas flowrates. The kinetic and adsorption parameters previously estimated and presented in Chapter 5 were used to describe the intrinsic kinetics of the process. The reactor activity and the conversion appear to be strongly dependent on the hydrogen flowrate demonstrating the occurrence of mass transfer phenomena.

An empirical correlation was proposed to calculate the overall mass transfer coefficient under reacting conditions at varying process parameters. This model is able to accurately predict the dependency of the mass transfer coefficient on the operating temperature, pressure, gas and liquid velocity.

6.2 Experimental

The hydrogenation experiments in fully continuous mode were carried out in the hydrogenation plant described in Section 5.2.2 conveniently modified. The main components of this experimental setup are sketched in Figure 6.1.

The reaction was conducted in the same structured reactor previously presented for the experiments in semi-batch mode.

Before the starting of the typical hydrogenation experiment the liquid phase (10 wt % MBY, 90 wt % MBE) was recirculated through the loop in Figure 6.1 (valve V2 closed) at high velocity (70 kg h^{-1}) and heated up in order to reach the desired reaction temperature.

After stabilization of pressure and temperature, the liquid mass flowrate was regulated to the desired value ($10 - 20 \text{ kg h}^{-1}$) and pure hydrogen was supplied from an external tank.

As soon as the hydrogen bubbles were visible in the view cell installed at the reactor inlet, the valve V1 was closed and the valve V2 was simultaneously opened. Before entering the reactor, the gas and the liquid phases were pre-mixed using an additional uncoated structure (diameter = 14 mm, length = 200 m) similar to the one used as metal support for the reactor. The size of the static mixer was increased compared to the semi-batch experimental analysis in order to improve the external mass transfer due to the lower liquid flowrate.

The structured reactor was thermally insulated to reduce the heat losses. After each experiment the setup was emptied and flushed with nitrogen.

Liquid samples were regularly withdrawn after stabilization of the operating conditions through a manual valve placed at the reactor outlet. The samples were analysed using a gas-chromatograph following the procedure previously described in Section 2.2.3.

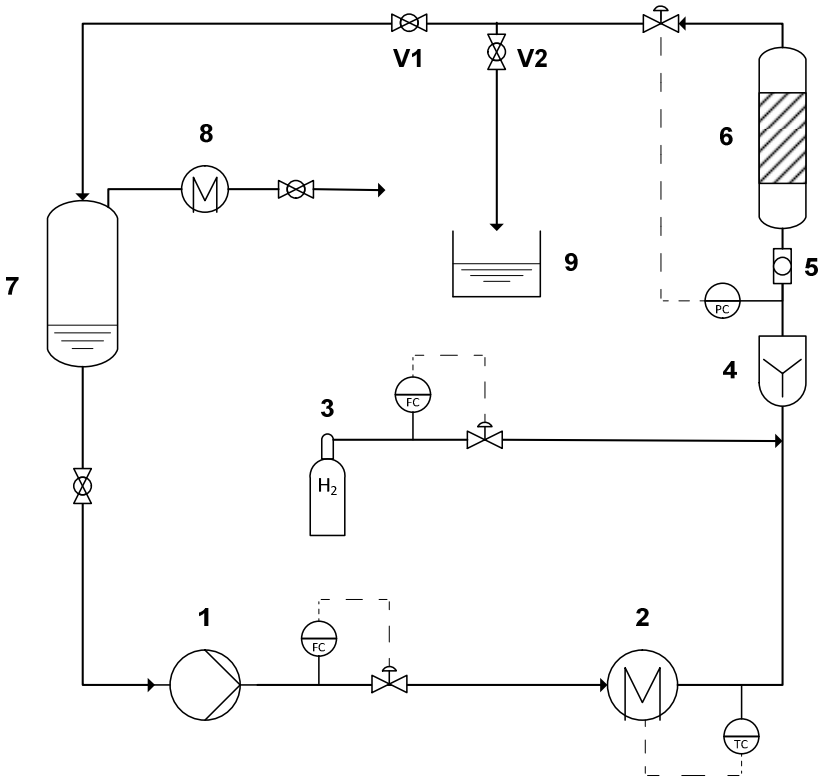


Figure 6.1: Simplified scheme of the experimental setup for continuous operation mode. (1) recirculation pump, (2) electrical heater, (3) hydrogen tank, (4) static mixer, (5) view cell, (6) structured reactor, (7) gas-liquid separator, (8) off-gas cooler (9) waste container.

6.3 Results

6.3.1 Reaction rate

The Péclet number is a measure of the relative importance of convective to diffusive phenomena. A liquid Péclet number was calculated according to [106] as:

$$Pe = \frac{u_L \cdot L}{D_{ax}} \quad (6.1)$$

where L is the length of the structured reactor and u_L is the superficial liquid velocity defined as:

$$u_L = \frac{4Q_L}{\pi \cdot d_r^2 \cdot \varepsilon} \quad (6.2)$$

The volumetric liquid flowrate was calculated as:

$$Q_L = \frac{\dot{m}_L}{\rho_L} \quad (6.3)$$

The axial dispersion D_{ax} in the streamwise-periodic porous media was established by Hutter *et al.* [96]:

$$D_{ax} = 6.98 \cdot 10^{-6} Re_{pore}^{0.72} \quad (6.4)$$

where the pore Reynolds number is defined as:

$$Re_{pore} = \frac{\rho_L \cdot u_L \cdot d_{pore}}{\mu_L} \quad (6.5)$$

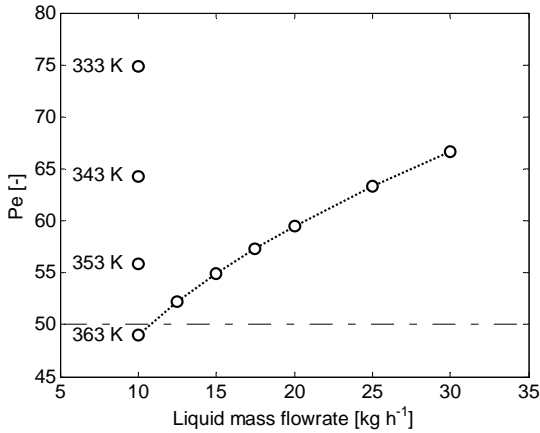


Figure 6.2: Péclet number at various liquid mass flowrates. Pressure: 7.0 bar, Hydrogen flowrate: 1.0 NL min⁻¹.

The values of Péclet number higher than 50 over almost the entire range of operating conditions allows the assumption of a plug flow model to describe the results according to the criterion reported in [106]. Under this assumption the MBY reaction rate can be expressed as:

$$r_1 = \frac{Q_L \cdot C_Y^0 \cdot X_Y}{n_{pd}} \quad (6.6)$$

The reaction rate was regularly calculated during the course of each experiment by withdrawing and analyzing samples at intervals of time between 2 and 5 min. Stable results were obtained in the whole range of conditions (Figure 6.3). No loss in catalyst activity was observed during this time. Each experiment was repeated three times and an average value was obtained.

Figure 6.4 shows the trend in the observed reaction rate over the investigated ranges of temperature (333 – 363 K) and pressure (3.0 – 7.0 bar). The linear variation of the reaction rate with the operating pressure confirms that it can be well described by a first-order de-

pendency with respect to hydrogen pressure, as previously demonstrated in Chapter 2.

Gas and liquid flowrates were adjusted in the ranges $10 \text{ kg h}^{-1} < \dot{m}_L < 30 \text{ kg h}^{-1}$ and $0.2 \text{ NL min}^{-1} < Q_G < 1 \text{ NL min}^{-1}$ in order to study the influence of superficial gas and liquid velocities on MBY conversion.

The gas superficial velocity was defined as:

$$u_G = \frac{4Q_G}{\pi \cdot d_r^2 \cdot \varepsilon} \quad (6.7)$$

The results are depicted in Figure 6.5. Conversion decreases with raised superficial liquid velocity due to the reduced residence time in the structured reactor. Furthermore, a higher superficial gas velocity results in a higher MBY conversion indicating a mass transfer limitation.

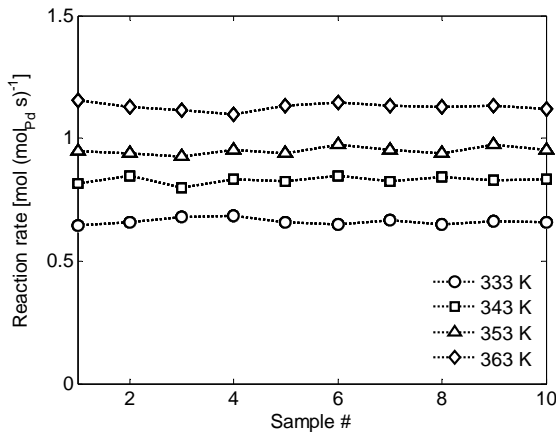


Figure 6.3: Catalyst activity versus sample number at varying temperatures. Pressure: 7.0 bar, Liquid flowrate: 10 kg h^{-1} , Hydrogen flowrate: 1 NL min^{-1} .

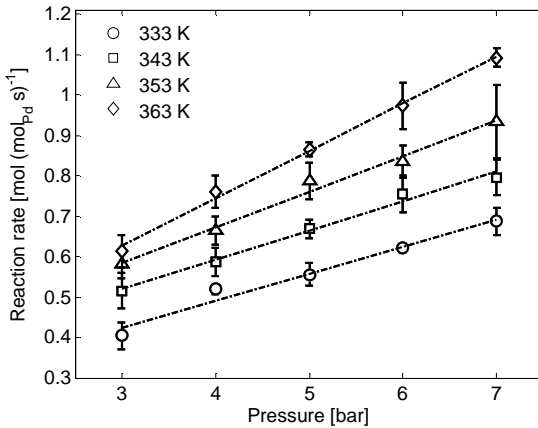


Figure 6.4: Effect of pressure and temperature on MBY reaction rate. Liquid flowrate: 10 kg h⁻¹. Hydrogen flowrate: 1 NL min⁻¹.

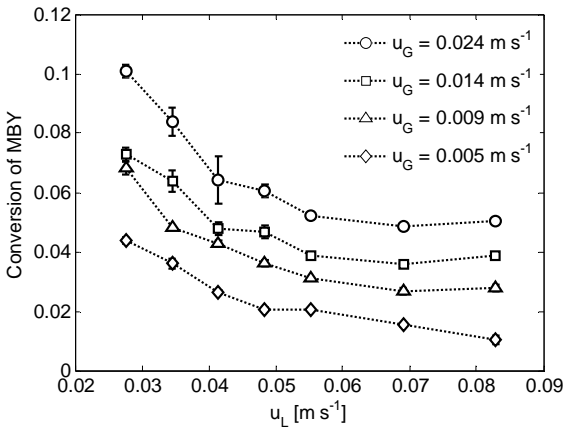


Figure 6.5: Effect of gas and liquid superficial velocities on MBY conversion. Temperature: 363 K, pressure: 7.0 bar.

6.3.2 Overall external mass transfer coefficient

The calculated conversions were used to estimate an overall G-L-S mass transfer coefficient K_{ov} , assumed to be constant along the reactor axis.

The reaction network was simplified to the first hydrogenation step from MBY to MBE. According to Chapter 5, the kinetics of this reaction are clearly dependent on the concentration of MBY and MBE according to:

$$r_1 = \left(\frac{k_1 K_Y C_Y K_H}{1 + K_Y C_Y + K_E C_E} \right) C_H \quad (6.8)$$

However the conversion obtained per pass was always lower than 15 % in the range of investigated conditions. Therefore, the kinetic expression was simplified assuming the concentration of MBY and MBE not to change during the reaction. Under this assumption the Langmuir-Hinshelwood kinetic expression can be simplified in a first order dependence with respect to the hydrogen concentration in the structured reactor C_H .

$$r_1 = k_1^* C_H \quad (6.9)$$

A similar approach was previously proposed in literature for the hydrogenation of MBY [32][82].

The hydrogen mass transfer between the gas phase and the surface of the catalyst can be expressed at the steady state as:

$$K_{ov}(C_H^* - C_H) \cdot V_R = r_1(C_H) \cdot n_{pd} \quad (6.10)$$

The system of Eqs. (6.6), (6.8)-(6.10) was solved in order to calculate the unknown K_{ov} and the corresponding hydrogen concentration at the surface of the catalyst in a wide range of experimental conditions.

6.3.3 Mass transfer modelling

A first attempt to model the mass transfer limitations was made assuming the controlling resistance on the liquid side. In this case the overall mass transfer coefficient can be approximated to $k_L a$.

This hypothesis is generally accepted at high liquid superficial velocities, as in the case of the present work [87].

A possible G-S resistance was neglected assuming that, due to the low hydrogen flowrates, the surface of the structured reactor was fully wetted.

A Sherwood number correlation was previously proposed in literature to describe the G-L mass transfer in tubular reactors containing foam packings [87][89]. This correlation expresses Sherwood number as function of the Reynolds (liquid and gas) and Schmidt numbers following the form:

$$Sh_{GL} \cdot a \cdot d_{cell} = \alpha \cdot Re_L^b \cdot Re_G^c \cdot Sc^{1/3} \left(\frac{d_{cell}}{d_r} \right)^d \quad (6.11)$$

with Sherwood number defined as:

$$Sh_{GL} \cdot a = \frac{k_L a \cdot d_{cell}}{D_H} \quad (6.12)$$

In Eq. (6.11) a represents the G-L specific surface area which is difficult to estimate. As consequence, the term $k_L a$ was kept undivided following the approach of Tourvieille *et al.* [89].

The Sherwood number for packed bed reactors is known to be influenced by particle and channel diameters [111]. The regular geometry of the structured reactor allows the definition of a cell diameter d_{cell} as the diameter of the spheres constituting the tetrahedral arrangement of the structure (see Table 5.1).

However, the experiments reported in this work were conducted without varying the cell diameter of the structured reactor. For this reason, the parameter d in Eq. (6.11) was fixed to the value of 1.14 reported by Tourvieille *et al.* [89].

The Schmidt number was calculated with respect to the liquid phase as:

$$Sc = \frac{\mu_L}{\rho_L \cdot D_H} \quad (6.13)$$

where D_H is the molecular diffusivity of hydrogen in the liquid phase estimated from the Wilke-Chang equation (2.9).

The Reynolds numbers were expressed using the cell diameter as characteristic length:

$$Re_G = \frac{\rho_G \cdot u_G \cdot d_{cell}}{\mu_G} \quad (6.14)$$

$$Re_L = \frac{\rho_L \cdot u_L \cdot d_{cell}}{\mu_L} \quad (6.15)$$

Around 70 experimental mass transfer coefficients estimated for different temperatures, pressures, gas and liquid flowrates were used in a single optimization procedure in order to estimate the three empirical parameters reported in Eq. (6.11).

The objective function $\varphi(\Theta)$ to be minimized, was obtained as sum of the squares of the errors between experimental and calculated overall mass transfer coefficients and expressed as:

$$\varphi(\Theta) = \sum_{i=1}^n \left(K_{ov}^{exp}{}_i - K_{ov}^{cal}{}_i(\Theta) \right)^2 \quad (6.16)$$

where n is the number of estimated experimental mass transfer coefficients and Θ a vector, containing the empirical parameters to be estimated (a , b and c).

In Figure 6.6 and Figure 6.7 the experimental (points) and the calculated (continuous lines) overall mass transfer coefficients are shown over different combinations of pressures (3.0 – 7.0 bar), temperatures (333 – 363 K) and two liquid flowrates (10 and 20 kg h⁻¹).

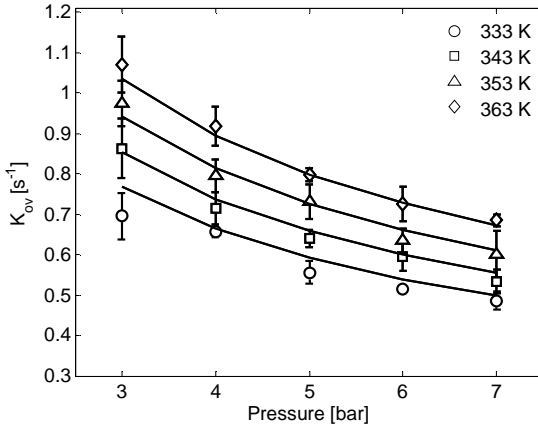


Figure 6.6: Effect of pressure and temperature on the overall mass transfer coefficient: experimental (points) and calculated (continuous lines) K_{ov} . Liquid flowrate: 10 kg h⁻¹. Hydrogen flowrate: 1 NL min⁻¹.

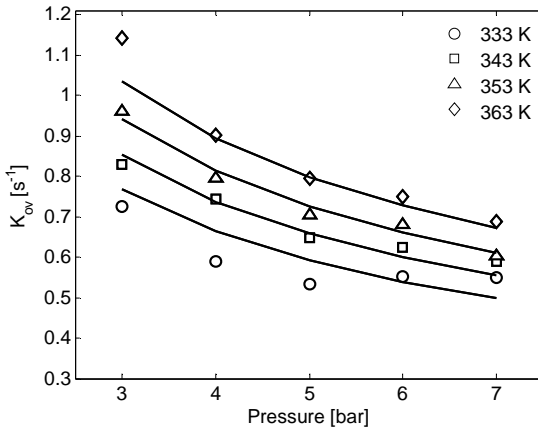


Figure 6.7: Effect of pressure and temperature on the overall mass transfer coefficient: experimental (points) and calculated (continuous lines) K_{ov} . Liquid flowrate: 20 kg h⁻¹. Hydrogen flowrate: 1 NL min⁻¹.

The overall mass transfer coefficient decreases with increasing the operating pressure of the reactor. The intrinsic volumetric coefficient k_L is usually considered to be independent of system pressure if the flow conditions remain constant. However, the experiments at various pressures were conducted using constant hydrogen mass flowrates. Higher pressures result in lower volumetric flowrates and, as a consequence, in a lower interfacial surface area a .

The decrease of diffusivity with temperature implies a direct increase of K_L . Additionally, the resulting lower viscosity and surface tension lead to a decrease of the average bubble sizes.

Figure 6.8 shows the effect of gas superficial velocity ($0.005 - 0.024 \text{ m s}^{-1}$) and liquid superficial velocity ($0.025 - 0.085 \text{ m s}^{-1}$) on K_{ov} . It is evident that increasing the liquid velocity up to 0.06 m s^{-1} does not significantly affect the mass transfer coefficient.

At higher liquid velocity the turbulence induced in the flow enhances the mass transfer properties. This results in a larger deviation of the calculated values from the experimental ones.

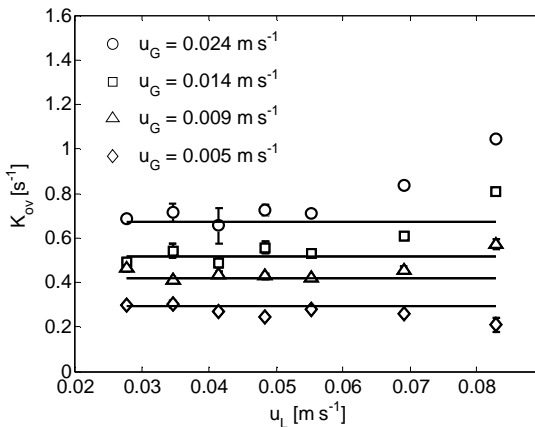


Figure 6.8: Effect of gas and liquid superficial velocities on the overall mass transfer coefficient: experimental (points) and calculated (continuous lines) K_{ov} . Temperature: 363 K, pressure: 7.0 bar.

The proposed model appears to have a good capability to simulate the behaviour of the system at low liquid velocities ($0.025 - 0.060 \text{ m s}^{-1}$) where the liquid flowrate does not significantly influence the overall mass transfer coefficient. At higher values this effect is not negligible resulting in larger deviations from the calculated values.

For this reason the validity of the proposed correlation was limited to the following range of liquid Reynolds number:

$$80 < Re_L < 300 \quad (6.17)$$

The experimental results obtained at $u_L > 0.06 \text{ m s}^{-1}$ were excluded from the optimization procedure.

The final correlation resulting from the optimization procedure can be expressed as:

$$Sh_{GL} \cdot a \cdot d_{cell} = (50 \pm 2) \cdot Re_G^{0.51 \pm 0.02} \cdot Sc^{1/3} \left(\frac{d_{cell}}{d_{reac}} \right)^{1.14} \quad (6.18)$$

An exponent b close to zero was found for Re_L in the Sh_{GL} expression as expected due to the considerations above.

It is worth noting that the proposed empirical model is a first attempt to model the mass transfer phenomena in the structured reactor. The correlation can certainly be improved by characterizing bubble sizes and distributions by means of a direct measurement method.

In order to validate the mass transfer model, the estimated parameters were used without any further adjustment to simulate the experimental results collected during additional experiments under a different combination of operating temperatures and gas velocities. A comparison between calculated and experimental mass transfer coefficients, the results of this validation procedure, is depicted in Figure 6.9. Figure 6.10 shows the parity plot for experimental and calculated mass transfer coefficients for $Re_L < 300$. The model was considered satisfactory with maximum deviations from the experimental values of approximately 15 %.

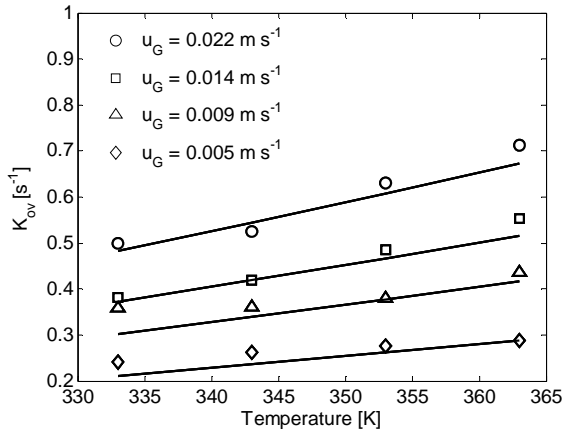


Figure 6.9: Comparison between experimental (points) and calculated (continuous lines) overall mass transfer coefficients K_{ov} . Pressure: 7.0 bar, liquid flowrate: 10 kg h^{-1} .

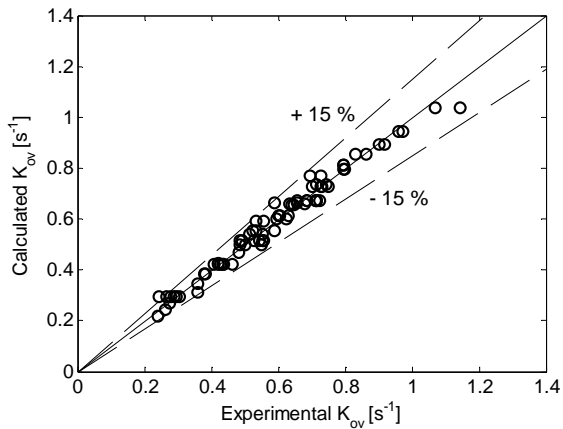


Figure 6.10: Parity plot of experimental and calculated values of the overall mass transfer coefficient K_{ov} . $Re_L < 300$.

6.3.4 Reactor design

The following model, combining the knowledge acquired on the intrinsic kinetics of the system and on the hydrogen mass transfer coefficient was finally used to simulate the concentration profiles in a system of several porous structured reactors in series.

$$u_L \frac{dC_Y}{dz} = -\frac{n_{Pd}}{V_R}(r_1 + 2r_3) \quad (6.19)$$

$$u_L \frac{dC_E}{dz} = \frac{n_{Pd}}{V_R}(r_1 - r_2) \quad (6.20)$$

$$u_L \frac{dC_A}{dz} = \frac{n_{Pd}}{V_R}r_2 \quad (6.21)$$

$$u_L \frac{dC_D}{dz} = \frac{n_{Pd}}{V_R}r_3 \quad (6.22)$$

$$u_L \frac{dC_H}{dz} = K_{ov}(C_H^* - C_H) - \frac{n_{Pd}}{V_R}(r_1 + r_2 + 2r_3) \quad (6.23)$$

The hydrogen mass transfer coefficients were calculated using Sherwood number estimated by Eqs. (6.18). The proposed model allows to simulate the concentrations of the reacting species along the axis of the series of structured reactors under a defined set of operating conditions as depicted in the exemplary Figure 6.11 and Figure 6.12.

Figure 6.13 shows the calculated MBY concentration profiles at various temperatures. Temperature affects both intrinsic kinetics and overall mass transfer coefficient of the process resulting in higher reaction rates.

The model is clearly based on the simplifying assumption of isobaric and isothermal conditions along the reactor axis. This is obviously not realistic for a reactor consisting of several porous structures in series due to the pressure drop and to the heat losses along the axis. Nevertheless, it can be considered a practical tool for a preliminary design of a pilot plant for continuous hydrogenation of MBY in flow.

The model also allows prediction of conversion, reaction rate and selectivity and can be used, therefore, to optimize the operating conditions of the process depending on the desired output.

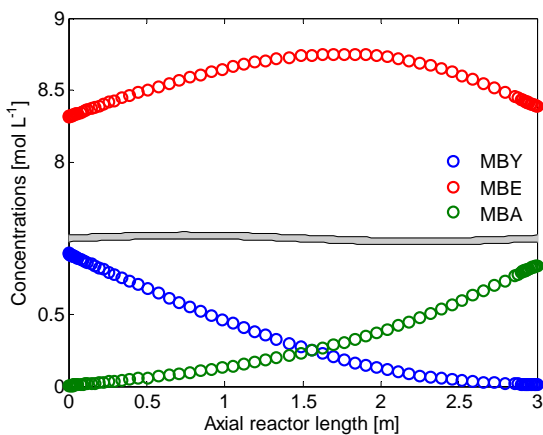


Figure 6.11: Calculated concentration profiles along the axial length of the structured reactor. Conditions: 363 K, 7.0 bar, liquid flowrate: 10 kg h⁻¹, gas flowrate: 1.0 NL min⁻¹, initial concentration of MBY: ca 10 wt %.

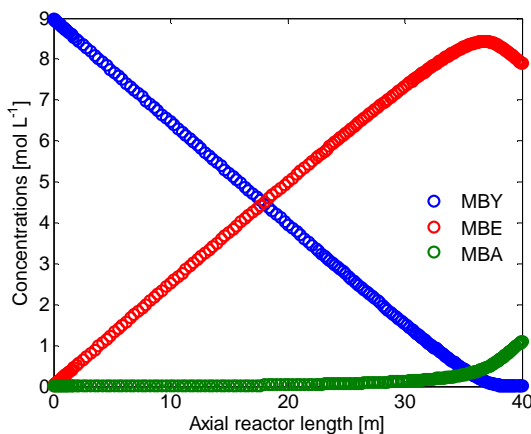


Figure 6.12: Calculated concentration profiles along the axial length of the structured reactor. Conditions: 363 K, 7.0 bar, liquid flowrate: 10 kg h⁻¹, gas flowrate: 1.0 NL min⁻¹, pure MBY as initial solution.

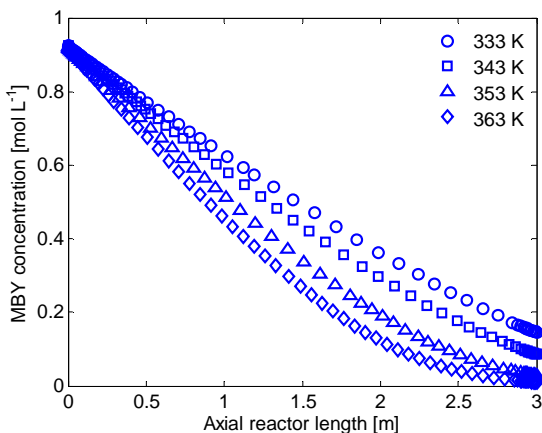


Figure 6.13: Calculated concentration profiles of MBY along the axial length of the structured reactor at various temperatures. Conditions: 7.0 bar, liquid flowrate: 10 kg h⁻¹, gas flowrate: 1.0 NL min⁻¹.

6.3.5 Conclusions

In this chapter, the designed structured reactor was tested in the continuous solvent-free hydrogenation of MBY. A simple plug flow model was assumed because of the liquid Péclet number was higher than 50 in the range of investigated conditions.

MBY reaction rate was found to increase linearly with pressure. The strong effect of the gas velocity on the conversion of MBY was attributed to the mass transport phenomena limiting the experimental results.

The overall external mass transfer coefficients K_{ov} were estimated based on the knowledge of the intrinsic kinetics of the process acquired during previous investigations. The K_{ov} values for hydrogen were found to range between 0.2 and 1.2 s⁻¹ under the reacting conditions. An empirical correlation was proposed to estimate these coefficients with very good agreement ($\pm 15\%$) with experimental data for liquid Reynolds number lower than 300. The mathematical model can accurately describe the influence of the process parameters

(temperature, pressure, gas and liquid flowrates) on the experimental mass transfer coefficients.

Separate G-L and L-S mass transfer measurements as well as a detailed hydrodynamic study would be useful to validate these results.

The developed mathematical model, combining kinetics and mass transfer, can be used for a preliminary design of a structured reactor for continuous hydrogenation of MBY.

7 Conclusions

In this work the kinetic mechanisms and the mass transfer properties of alkyne hydrogenations with industrial relevance in vitamin synthesis have been addressed.

These reactions are industrially carried out in the liquid phase in batch processes in the presence of Lindlar catalyst, a Pd/CaCO₃ powder modified by the addition of lead to improve alkene selectivity.

This thesis originates from the practical need to intensify these processes in prospect of a transition from batch to continuous. Particular attention was dedicated to the use of a Pd-based lead-free catalyst in combination with structured reactors.

In the following paragraphs the main findings are shortly summarized.

Kinetic modelling of MBY and DIP hydrogenations

In order to understand the intrinsic kinetics of the reacting systems, batch experiments were performed in a stirred reactor over a commercial Lindlar catalyst. Kinetic studies were conducted on the selective hydrogenations of MBY and DIP, which are key reactions in the manufacture of α -tocopherol, one of the components with the highest vitamin E activity.

Langmuir-Hinshelwood mechanisms based on non-competitive adsorption between hydrogen and organic species and dissociative adsorption of hydrogen were proposed to describe the kinetics of these reacting processes.

Volumetric G-L mass transfer coefficients were estimated in a range of temperature and in the absence of the catalyst by gas ab-

sorption experiments. The L-S mass transfer coefficients were theoretically calculated by means of empirical correlations and found to be significantly higher than the corresponding G-L coefficients. G-L mass transfer resistances which presented non-negligible values were included in the model.

The main aim of this study was proposing a general mathematical model and a detailed set of kinetic parameters able to accurately predict the concentration profiles of the species involved in the hydrogenation processes at varying temperatures, pressures and catalyst loadings.

The experiments were designed to investigate the typical mild operating conditions of industrial reactors.

The mathematical models, successfully validated allow to predict the influence of the operating conditions and of the addition of quinoline, as reaction modifier, on the selectivity of the process. The selectivity of dehydroisophytol hydrogenation to the corresponding alkene was found to decrease with temperature. On the other hand, no significant effect of the hydrogen pressure on the selectivity was observed in the investigated operating range.

Pd/ZnO catalyst for selective hydrogenations of alkynes

A Pd/ZnO catalyst was developed and tested in the selective hydrogenation of MBY. The catalyst was prepared by coating a metal powder with a ZnO/Al₂O₃ base layer impregnated, in a later stage, with Pd nanoparticles. The microstructure of the catalyst was observed and chemically characterized by FIB/SEM equipped with EDX apparatus.

The metal particles appear to be fully coated with a homogeneous base layer about 700 nm thick. HAADF-STEM analysis reveals that Pd is dispersed on the external surface of the catalyst in the form of nanoparticles with diameters up to 10 nm and larger agglomerations in certain regions.

The process exhibits higher initial activity and selectivity compared to the commercial Lindlar catalyst. The high selectivity of the process to MBE was ascribed to the thermodynamics of the alkyne

hydrogenation. Zn acts as a promoter in Pd-based catalysts resulting in a lower adsorption strength of alkynes and alkenes and, as a consequence, in a higher process selectivity.

Hydrogenation of MBY in a structured reactor with Pd/ZnO catalyst

A porous tubular metal structure characterized by a regular geometry was coated with a layer of ZnO/Al₂O₃ and impregnated with Pd nanoparticles. The reactor was operated in semi-batch mode with recirculation of the process liquid and continuous supply of hydrogen with co-current upward flow.

Several experimental runs were performed at varying temperatures and hydrogen flowrates. The experiments conducted at high gas flowrates showed constant initial reaction rate and were, for this reason, assumed to occur in absence of any mass transfer limitation.

On the other hand, at low hydrogen flowrates, the experimental reaction rate was found to be strongly dependent on gas velocity.

The Langmuir-Hinshelwood kinetic model, previously developed for the hydrogenation over Lindlar catalyst, was adapted and used to estimate the relevant kinetic and adsorption parameters governing the process.

The extension of the model to the mass transfer limited regime, at low hydrogen flowrates, allowed the estimation of an overall mass transfer coefficient. The occurrence of transport limitations in this operating window was confirmed by high values of Carberry number.

The mathematical model, successfully validated, is able to accurately predict the concentration profiles of the species involved in the system at varying temperatures and pressures in both kinetic and mass transfer limited regimes.

Continuous hydrogenation of MBY in a structured reactor

The previously characterized structured reactor was tested in the continuous hydrogenation of MBY aiming at Process Intensification.

Overall external mass transfer was found to strongly limit the performance of the process. The kinetic and adsorption parameters, previously estimated during the experimental campaign in semi-batch mode, were used during this study without any further adjustment.

A simple plug flow reactor model, justified by high values of Péclet number, was applied to estimate the overall mass transfer coefficient under reacting conditions. The results were modelled proposing a Sherwood number correlation which gives good agreement with experimental data.

The mass transfer behaviour can reasonably reflect the performance of an industrial multi-tubular reactor with higher capacity.

8 Outlook

In this work the kinetic mechanisms and the mass transfer properties of alkyne hydrogenations with industrial relevance in vitamin synthesis have been addressed.

This section tries to give directions for future research on the topic with respect to applications of new measurement techniques and design of the reactor support.

8.1 Design of the porous structure

The laser sintering technique used to produce the designed structured reactor allows to design three-dimensional metal supports of nearly any shape. The optimal geometry of a structured reactor for exothermic three-phase reactions is related to the following requirements:

- L-S specific surface area for catalyst loading
- G-L specific surface area
- Mixing properties
- Heat transfer and thermal homogenization

Simple design procedures can improve some of these requirements.

A novel structured reactor geometry (triangular structure) was recently designed with larger specific surface area and improved dispersion properties [117][118]. The geometrical structure and the unit cell of the reactor support are depicted in Figure 8.1.

The triangular structure is characterized by triangular channels following the concept of a monolith reactor. However, the channels are radially translated resulting in break-up of the gas bubbles and improved mixing properties.

The triangular channels were chosen to increase the specific surface area of the reactor while keeping low pressure drops.

The main features of this structured reactor are listed in Table 8.1.

It is worth noting that the triangular structure exhibits a double specific surface area compared to the previously investigated porous structure. Therefore, this novel support could be theoretically loaded with a bigger amount of active catalyst.

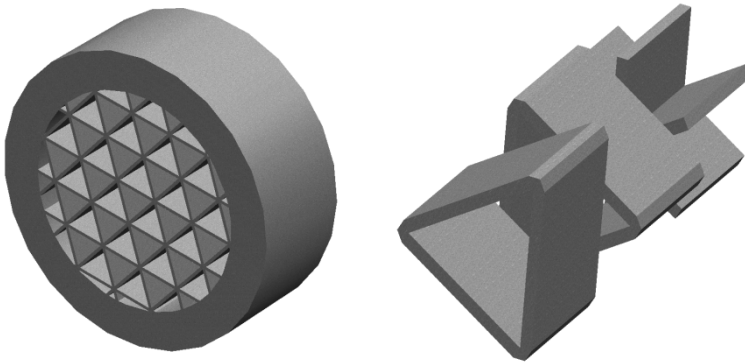


Figure 8.1: Left: Auxiliary view of the triangular structure. Right: unit cell of the triangular structure. Adapted from [117].

Table 8.1: Triangular structured reactor characteristics.

Parameter	Units	Value
Length	m	0.2
Inner diameter	m	$1.4 \cdot 10^{-2}$
Side length triangle	m	$2.4 \cdot 10^{-3}$
Structure volume	m^3	$7.0 \cdot 10^{-6}$
Porosity	-	0.77
Specific surface area	m^{-1}	2587
Hydraulic diameter	m	$1.2 \cdot 10^{-3}$

8.2 Preliminary experiments

The triangular structured reactor was subjected to thermal pre-treatment, coating with an $\text{Al}_2\text{O}_3/\text{ZnO}$ base layer, Pd deposition and thermal activation following the same experimental procedure presented in Section 5.2.1 (same catalyst loading). Figure 8.2 shows the cross section of the metal support before and after the catalyst deposition.

SEM analysis should be conducted on sections of the structure in order to gain knowledge of the base layer thickness and the Pd distribution.

The triangular structured reactor was tested in the continuous hydrogenation of MBY using the experimental setup and procedure previously described in Section 6.2.

Figure 8.3 and Figure 8.4 show a comparison of the MBY hydrogenation rate over the porous and the triangular structured reactors at various temperatures and pressures. These preliminary results obtained using this novel structured reactor show an increased reaction rate (30 – 40 %) compared to the porous structure. The improved performance can be ascribed to the larger L-S surface area and to a higher G-L mass transfer coefficient. However, a detailed study under a wide range of operating conditions has to be conducted in order to

characterize the mass transport properties of the structure. Further investigations in this direction are currently in progress.

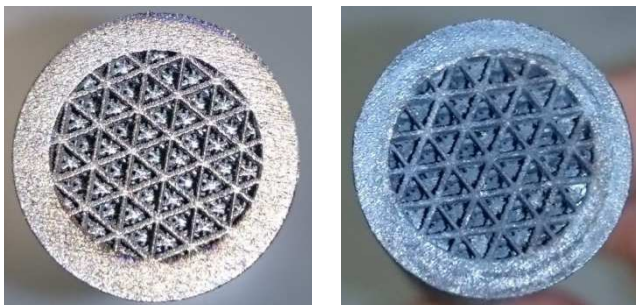


Figure 8.2: Left: Cross section of the metal support of the triangular structured reactor. Right: Cross section of the Pd-Al₂O₃/ZnO coated triangular structured reactor.

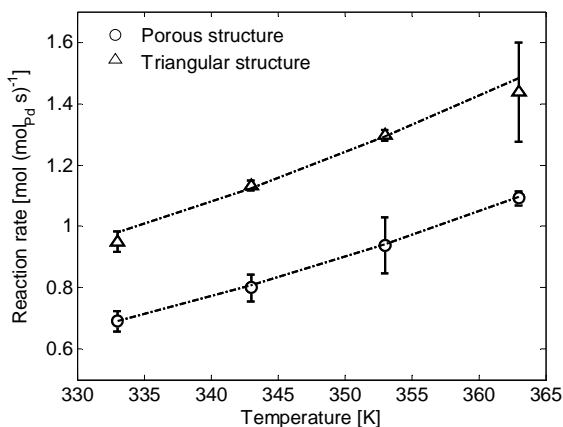


Figure 8.3: Effect of temperature on the MBY hydrogenation rate over porous and triangular structured reactor. Pressure: 7.0 bar, liquid flowrate: 10 kg h⁻¹, hydrogen flowrate: 1 NL min⁻¹.

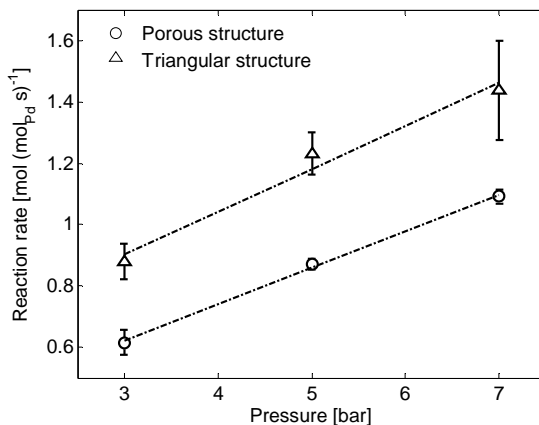


Figure 8.4: Effect of pressure on the MBY hydrogenation rate over porous and triangular structured reactor. Temperature: 363 K, liquid flowrate: 10 kg h⁻¹, hydrogen flowrate: 1 NL min⁻¹.

8.3 Bubble size measurement

G-L mass transfer phenomena were found to strongly affect the experimental results during the hydrogenation experiments.

The mathematical model describing the intrinsic kinetics of the system was extended to the mass transfer limited regime using an overall coefficient K_{ov} . This mass transfer coefficient includes the fundamental information on the G-L specific surface, affecting the transport phenomena.

The mathematical model can certainly be improved by means of direct characterization of bubble sizes and distributions.

The view-cell installed in the experimental setup at the reactor inlet offers the possibility of predicting the impact of the operating parameters (temperature, pressure, liquid and gas velocity) on the bubble size. Bubble diameters are expected to decrease with increasing Re due to increasing shear forces in the structure.

However, the break-up of the bubbles in the porous channel is expected to increase the G-L specific contact surface resulting in improved mass transport.

Recently, Alzheimer *et al.* applied shadow imaging to a bubbly G-L two-phase flow in a porous structure [113]. This technique is a useful method to acquire information on gas hold-up and total interfacial area for two-phase flow in complex geometries. During that study this method was applied to a porous structure made of a clear epoxy resin. Optical access was provided by using an aqueous solution of sodium iodide and zinc iodide as liquid phase in order to have the same refractive index as the structure material. Nitrogen was injected as gas phase for safety issues.

Taking into account the complexity of the proposed measurement technique in combination with the system MBY/hydrogen, the G-L two-phase flow could be investigated in numerical simulations. In this way, details on bubble size, as well as velocity profiles, liquid velocity fields and additionally, heat transfer, could be determined.

A functional trend to describe the change of the G-L specific surface along the reactor axis under different operating conditions could be implemented in the mathematical model in order to improve the model predictions.

Bibliography

- [1] F. Roessler, Catalytic hydrogenations in the liquid phase, *Chimia* 57 (2003) 791 – 798.
- [2] F. Nerozzi, Heterogeneous catalytic hydrogenation, *Platinum Metals Rev.* 56 (2012) 236 – 241.
- [3] L. Guzzi, Á. Molnár, D. Teschner, Hydrogenation reactions: concepts and practice. In *Comprehensive inorganic chemistry II: from elements to applications*, vol. 7, Elsevier.
- [4] P. Pollak, *Fine Chemicals: the industry and the business*, Wiley, Hoboken, USA, 2011.
- [5] W. Bonrath, T. Netscher, Catalytic processes in vitamins synthesis and production. *Appl. Catal. A* 280 (2005) 55 – 73.
- [6] W. Bonrath, M. Eggersdorfer, T. Netscher, Catalysis in the industrial preparation of vitamins and nutraceuticals. *Cat. Today* 121 (2007) 45 – 57.
- [7] M. Eggersdorfer, G. Adam, *Ullmann's Encyclopedia of Industrial Chemistry*, vol. A27, 5th ed., VCH, Weinheim, 1996, 446.
- [8] R. A. Sheldon, H. van Bekkum, *Fine chemicals through heterogeneous catalysis*, Weinheim, Wiley-VCH.

- [9] T. Netscher, Synthesis of vitamin E, Vitamins and hormones, Elsevier, 76, 2012.
- [10] M. F. Carroll, Addition of α,β -unsaturated alcohols on the active methylene group. Part I. The action of ethyl acetoacetate on linalool and geraniol. *J. Chem. Soc.* (1940) 704 – 706.
- [11] G. Saucy, R. Marbet, Über die Reaktion von tertiären Vinylicarbinolen mit Isopropenyläther. Eine neue Methode zur Herstellung von γ,δ -ungesättigten Ketonen. *Helv. Chim. Acta* 50 (2001).
- [12] A. Molnar, A. Sarkany, M. Varga, Hydrogenation of carbon-carbon multiple bonds: chemo-, regio- and stereo-selectivity. *J. Mol. Catal. A* 73 (2001) 185 – 221.
- [13] P. N. Rylander, Hydrogenation methods, Academic Press, New York, USA, 1990.
- [14] H. Lindlar, Ein neuer Katalysator für selektive Hydrierungen. *Helv. Chim. Acta* 35 (1992) 446.
- [15] H. Lindlar, R. Dubuis, Palladium catalyst for partial reduction of acetylenes. Organic Synthesis, vol. 5, Wiley, New York, 1973, 880.
- [16] S. L. Y. Tang, R. L. Smith, M. Poliakoff, Principles of green chemistry: productively. *Green Chem.* 7 (2005) 761 – 762.
- [17] I. Pálincó, Effects of surface modifiers on the liquid-phase hydrogenation of alkenes over silica-supported platinum, palladium and rhodium catalysts I. Quinoline and carbon tetrachloride. *Appl. Catal. A* 126 (1995) 39 – 49.

-
- [18] C. T. Campbell, Catalyst-support interactions: electronic perturbations. *Nat. Chem.* 4 (2012) 597 – 598.
- [19] W. Bonrath, J. Medlock, J. Schütz, B. Wüstenberg, T. Netscher, Hydrogenation in the vitamins and fine chemical industry – an overview, Hydrogenation, Karamé, Rijeka, 2012.
- [20] C. Ramshaw, The incentive for process intensification, Proceedings 1st Int. Conf. Proc. Intensif. for Chem. Ind. 18, BHR Group London (1995) 1.
- [21] A. I. Stankiewicz, J. A. Moulijn, Process intensification: transforming chemical engineering. *Chem. Eng. Prog.* 96 (2000) 22 – 34.
- [22] G. S. Calabrese, S. Pissavini, From batch to continuous flow processing in chemicals manufacturing. *AIChE J.* 57 (2011) 828 – 834.
- [23] D. M. Roberge, L. Ducry, N. Bieler, P. Cretton, B. Zimmermann, Microreactor technology: a revolution for the fine chemical and pharmaceutical industry? *Chem. Eng. Technol.* 28 (2005) 318 – 323.
- [24] E. H. Stitt, Alternative multiphase reactors for fine chemicals: a world beyond stirred tanks? *Chem. Eng. J.* 90 (2002) 47 – 60.
- [25] S. G. Newman, K. F. Jensen, The role of flow in green chemistry and engineering. *Green Chem.* 15 (2013) 1456 – 1472.
- [26] J. Gascon, J. R. van Ommen, J. A. Moulijn, F. Kapteijn, Structuring catalyst and reactor – an inviting avenue to process intensification. *Catal. Sci. Technol.* 5 (2015) 807 – 817.

- [27] A. Montebelli, C. G. Visconti, G. Groppi, E. Tronconi, S. Kohler, Optimization of compact multitubular fixed-bed reactors for the methanol synthesis loaded with highly conductive structured catalysts. *Chem. Eng. J.* 255 (2014) 257 – 265.
- [28] G. Che-Galicia, R. S. Ruiz-Martinez, F. Lopez-Isunza, C. O. Castillo-Araiza, Modeling of oxidative dehydrogenation of ethane to ethylene on a MoVTeNbO/TiO₂ catalyst in an industrial-scale packed bed catalytic reactor. *Chem. Eng. J.* 280 (2015) 682 – 694.
- [29] J. A. Moulijn, A. Stankewicz, F. Kapteijn, The potential of structured reactors in Process Intensification. *Chem. Sus. Dev.* 11 (2003) 3 – 9.
- [30] A. Cybulski, J. A. Moulijn, Structured catalysts and reactors, CRC Press, Taylor & Francis Group, 2006.
- [31] 3-buten-2-ol, 2-methyl-, CAS No. 115-18-4, UNEP Publications.
- [32] M. Crespo-Quesada, M. Grasemann, N. Semagina, A. Renken, L. Kiwi-Minsker, Kinetics of the solvent-free hydrogenation of 2-methyl-3-buten-2-ol over a structured Pd-based catalyst. *Catal. Today* 147 (2009) 247 – 254.
- [33] A. Bruehwiler, N. Semagina, M. Grassmann, A. Renken, L. Kiwi-Minsker, A. Saaler, H. Lehmann, W. Bonrath, F. Roessler, Three-phase catalytic hydrogenation of a functionalized alkyne: mass transfer and kinetic studies with in situ hydrogen monitoring. *Ind. Eng. Chem. Res.* 47 (2008) 6862 – 6869.
- [34] V. E. Rebrov, A. E. Klinger, A. Berenguer-Murcia, M. E. Sulman, C. J. Schouten, Selective hydrogenation of

- 2-methyl-3-butyn-2-ol in a wall-coated capillary microreactor with Pd₂₅Zn₇₅/TiO₂ Catalyst. *Org. Process Res. Dev.* 13 (2009) 991 – 998.
- [35] P. E. Liley, G. H. Thompson, D. G. Friend, T. E. Daubert, E. Buck, Physical and chemical data. In Perry's Chemical Engineers' Handbook, ed. 8. D. W. Green, ed. New York, McGraw-Hill, 2008.
- [36] E. Dietrich, C. Mathieu, H. Delmas, J. Jenck, Raney-nickel catalyzed hydrogenations: gas-liquid mass transfer in gas-induced stirred slurry reactors. *Chem. Eng. Sci.* 47 (1992) 3597 – 3604.
- [37] A. Deimling, B. M. Karandikar, Y. T. Shah, Solubility and mass transfer of CO and H₂ in Fischer – Tropsch liquids and slurries. *Chem. Eng. J.* 28 (1984) 127 – 140.
- [38] V. Meille, N. Pestre, P. Fongarland, C. de Bellefon, Gas/liquid mass transfer in small laboratory batch reactors: comparison of methods. *Ind. Eng. Chem. Res.* 43 (2004) 924 – 927.
- [39] J. Inga, B. I. Morsi, Effect of catalyst loading on gas/liquid mass transfer in a slurry reactor: a statistical experimental approach. *Can J. Chem. Eng.* 75 (1997) 872 – 881.
- [40] M. Oyevaar, A. Zijl, R. Westerterp, Interfacial areas and gas hold-ups at elevated pressures in mechanically agitated gas-liquid reactors. *Chem. Eng. Techn.* 11 (1988) 1 – 10.
- [41] C. Gérard, C. Roizard, N. Midoux, A. Laurent, J. C. Charpentier, Influence de la pression sur l'absorption d'un gaz

dans un liquid suivie de réaction chimique. *Récents progrès en génie des procédés* 3. 8 (1989) 26 – 31.

- [42] Y. Sano, N. Yamaguchi, T. Adachi, Mass transfer coefficients for suspended particles in agitated vessels and bubble columns. *J. Chem. Eng. Jpn.* 7 (1974) 255 – 261.
- [43] R. L. Bates, P. L. Fondy, R. R. Corpstein, An examination of some geometric parameters of impeller power. *Ind. Eng. Chem. Proc. Des. Dev.* 2 (1963) 310 – 314.
- [44] C. R. Wilke, P. Chang, Correlation of diffusion coefficients in dilute solutions. *AIChE J.* 1 (1955) 264.
- [45] G. Vilé, N. Almora-Barrios, S. Mitchell, N. Lopez, J. Perez-Ramirez, From the Lindlar catalyst to supported ligand-modified palladium nanoparticles: selectivity patterns and accessibility constraints in the continuous flow three-phase hydrogenation of acetylenic compounds. *Chem. Eur. J.* 20 (2014) 5926 – 5937.
- [46] B. Fillion, B. I. Morsi, Gas-liquid mass transfer and hydrodynamic parameters in a soybean oil hydrogenation process under industrial conditions. *Ind. Eng. Chem. Res.* 39 (2000) 1163 – 1168.
- [47] M. Meyberg, F. Roessler, In situ measurement of steady-state hydrogen concentrations during a hydrogenation reaction in a gas-inducing stirred slurry reactor. *Ind. Eng. Chem. Res.* 44 (2005) 9705 – 9711.

- [48] S. L. Kiperman, Some problems of chemical kinetics in heterogeneous hydrogenation catalysis. *Stud. Surf. Sci. Catal.* 27 (1986) 1 – 52.
- [49] S. L. Kiperman, Kietic models of heterogeneous catalytic reactions (review), *Russ. Chem. Bull.* 40 (1991) 2350 – 2365.
- [50] L. Zh. Nikoshvili, A. S. Makarova, N. A. Lyubimova, A. V. Bykov, A. I. Sidorov, I. Yu. Tyamina, V. G. Matveeva, E. M. Sulman, Kinetic study of selective hydrogenation of 2-methyl-3-butyn-2-ol over Pd-containing hypercrosslinked polystyrene. *Catal. Today* 256 (2015) 231 – 240.
- [51] J. A. Alves, S. P. Bressa, O. M. Martinez, G. F. Barreto, Kinetic study of the liquid-phase selective hydrogenation of 1-butyne in presence of 1-butene over a commercial palladium-based catalyst. *Chem. Eng. Res. Des.* 89 (2011) 384 – 397.
- [52] S. P. Bressa, O. M. Martinez, G. F. Barreto, Kinetic study of the hydrogenation and hydroisomerization of the n-butenes on a commercial palladium/alumina catalyst. *Ind. Eng. Chem. Res.* 42 (2003) 2081 – 2092.
- [53] J. A. Alves, S. P. Bressa, O. M. Martinez, G. F. Barreto, Kinetic study of the liquid-phase hydrogenation of 1-butyne over a commercial palladium/alumina catalyst. *Chem. Eng. J.* 125 (2007) 131 – 138.
- [54] A. Yarulin, I. Yuranov, F. Cardenas-Lizana, P. Abdulkin, L. Kiwi-Minsker, Size-effect of Pd-(poly(N-vinyl-2-pyrrolidone)) nanocatalysts on selective hydrogenation of alkynols with different alkyl chains. *J. Phys. Chem. C* 117 (2013) 13424 – 13434.

- [55] M. Crespo-Quesada, R. R. Dykeman, G. Laurenczy, P. J. Dyson, L. Kiwi-Minsker, Supported nitrogen-modified Pd nanoparticles for the selective hydrogenation of 1-hexyne. *J. Catal.* 279 (2011) 66 – 74 .
- [56] G. V. Smith, F. Notheisz, Heterogeneous catalysis in organic chemistry. Academic press, San Diego, 1999.
- [57] S. Vernuccio, Ph. Rudolf von Rohr, J. Medlock, General kinetic modeling of the selective hydrogenation of 2-methyl-3-butyne-2-ol over a commercial palladium-based catalyst. *Ind. Eng. Chem. Res.* 54 (2015) 11543 – 11551.
- [58] E. Joannet, C. Horny, L. Kiwi-Minsker, A. Renken, Palladium supported on filamentous active carbon as effective catalyst for liquid-phase hydrogenation of 2-butyne-1,4-diol to 2-butene-1,4-diol. *Chem. Eng. Sci.* 57 (2002) 3453 – 3460.
- [59] N. Semagina, A. Renken, L. Kiwi-Minsker, Monodispersed Pd-nanoparticles on carbon fiber fabrics as structured catalyst for selective hydrogenation. *Chem. Eng. Sci.* 62 (2007) 5344 – 5348.
- [60] E. M. Sulman, L. Zh. Nikoshvili, V. G. Matveeva, I. Yu. Tyamina, A. I. Sidorov, A. V. Bykov, G. N. Demidenko, B. D. Stein, L. M. Bronstein, Palladium containing catalysts based on hypercrosslinked polystyrene for selective hydrogenation of acetylene alcohols. *Top. Catal.* 55 (2012) 492 – 497.
- [61] A. Yarulin, I. Yuranov, F. Cardenas-Lizana, D. T. L. Alexander, L. Kiwi-Minsker, How to increase the selectivity of Pd-based catalyst in alkynol hydrogenation: effect of second metal. *Appl. Catal. A* 478 (2014) 186 – 193.

- [62] W. Bonrath, B. Ondruschka, C. Schmoeger, A. Stolle, Novel selective hydrogenation catalyst comprising palladium on porous silica glass and the use thereof, Patent EP2328679 A1, 2011.
- [63] D. V. Sokol'skii, T. O. Omarkulov, Zh. Mukataev, L. K. Zhubanova, L. V. Babenkova, Hydrogenation of 3,7,11,15-tetramethyl-1-hexadecyn-3-ol (dehydroisophytol) over cerium and palladium-cerium catalysts on alumina under hydrogen pressure. *Kinet. Catal.* 26 (1985) 643 – 645.
- [64] T. O. Omarkulov, Zh. Mukataev, S. V. Goncharova, G. M. L'dokova, D. V. Sokol'skii, Kinetics and selectivity of the hydrogenation of a C₂₀ acetylenic alcohol (dehydroisophytol) on supported palladium catalysts under hydrogen pressure in a flow system. *J. Appl. Chem. USSR* 58 (1985) 1409 – 1412.
- [65] P. A. Ramachandran, R. V. Chaudari, Three phase catalytic reactors, Gordon and Breach Science Publishers, New York, 1983.
- [66] J. B. Butt, Reaction Kinetics and Reactor Design, Marcel Dekker Inc., New York, 2000.
- [67] R. Tschan, M. M. Schubert, A. Baiker, W. Bonrath, H. Lansink-Rotgerink, Continuous semihydrogenation of a propargylic alcohol over amorphous Pd₈₁Si₁₉ in dense carbon dioxide: effect of modifiers. *Cat. Lett.* 75 (2001) 31 – 36.
- [68] J. A. Alves, S. P. Bressa, O. M. Martinez, G. F. Barreto, Kinetic evaluation of the set of reactions in the selective hydrogenation of 1-butyne and 1,3-butadiene in presence of n-butenes. *Ind. Eng. Chem. Res.* 52 (2013) 5849 – 5861.

- [69] S. Vernuccio, A. Meier, Ph. Rudolf von Rohr. Kinetic investigation of the solvent-free hydrogenation of dehydroisophytol. *Ind. Eng. Chem. Res.* 56 (2017) 4929 – 4937.
- [70] A. J. McCue, A. Gibson, J. A. Anderson, Palladium assisted copper/alumina catalysts for the selective hydrogenation of propyne, propadiene and propene mixed feeds. *Chem. Eng. J.* 285 (2016) 384 – 391.
- [71] T. A. Nijhuis, G. van Koten, F. Kaptejn, J. A. Moulijn, Separation of kinetics and mass-transport effects for a fast reaction: the selective hydrogenation of functionalized alkynes. *Catal. Today* 315 (2003) 79 – 80.
- [72] T. Mallat, A. Baiker, Selectivity enhancement in heterogeneous catalysis induced by reaction modifiers. *Appl. Catal. A* 200 (2000) 3 – 22.
- [73] N. Semagina, M. Grasemann, N. Xanthopoulos, A. Renken, L. Kiwi-Minsker, Structured catalyst of Pd/ZnO on sintered metal fibers for 2-methyl-3-butyne-2-ol selective hydrogenation. *J. Catal.* 251 (2007) 213 – 222.
- [74] M. Garcia-Mota, J. Gomez-Diaz, G. Novell-Leruth, C. Vargas-Fuentes, L. Bellarosa, B. Bridier, J. Perez-Ramirez, N. Lopez, A density functional theory study of the ‘mythic’ Lindlar hydrogenation catalyst. *Theor. Chem. Acc.* 128 (2011) 663 – 673.
- [75] I. S. Mashkovsky, G. N. Baeva, A. Y. Stakheev, M. N. Vargaftik, N. Y. Kozitsyna, I. I. Moiseev, Novel Pd-Zn/C catalyst for selective alkyne hydrogenation: evidence for the formation of Pd-Zn bimetallic alloy particles. *Mendeleev Commun.* 24 (2014) 355 – 357.

- [76] L. N. Protasova, E. V. Rebrov, K. L. Choy, S. Y. Pung, V. Engels, M. Cabaj, A. E. H. Wheatley, J. C. Schouten, ZnO based nanowires grown by chemical vapour deposition for selective hydrogenation of acetylene alcohols. *Catal. Sci. Technol.* 1 (2011) 768 – 777.
- [77] E. V. Ramos-Fernandez, A. F. P. Ferreira, A. Sepulveda-Escribano, F. Kapteijn, F. Rodriguez-Reinoso, Enhancing the catalytic performance of Pt/ZnO in the selective hydrogenation of cinnamaldehyde by Cr addition to the support *J. Catal.* 258 (2008) 52 – 60.
- [78] W. Bonrath, A. Buss, Metal powderdous catalyst for hydrogenation processes, wo 2013/124392, patent.
- [79] J. Xu, X. Su, X. Liu, X. Pan, G. Pei, Y. Huang, X. Wang, T. Zhang, H. Geng, Methanol synthesis from CO₂ and H₂ over Pd/ZnO/Al₂O₃: catalyst structure dependence of methanol selectivity. *Appl. Catal. A* 514 (2016) 51 – 59.
- [80] S. Vernuccio, R. Goy, Ph. Rudolf von Rohr, J. Medlock, W. Bonrath, Hydrogenation of 2-methyl-3-butyn-2-ol over a Pd/ZnO catalyst: kinetic model and selectivity study. *React. Chem. Eng.* 1 (2016) 445 – 453.
- [81] A. Antony, C. Hakanoglu, A. Asthagiri, J. F. Weaver, Dispersion-corrected density functional theory calculations of the molecular binding of n-alkanes on Pd(111) and PdO(101). *J. Chem. Phys.* 136 (2012) 054702/1 – 054702/9.
- [82] M. Grasemann, A. Renken, M. Kashid, L. Kiwi-Minsker, A novel compact reactor for three-phase hydrogenations. *Chem. Eng. Sci.* 65 (2010) 364 – 371.

-
- [83] K. Pangarkar, T. J. Schildhauer, J. R. van Ommen, J. Nijenhuis, F. Kapteijn, J. A. Moulijn, Structured packings for multiphase catalytic reactors. *Ind. Eng. Chem. Res.* 47 (2008) 3720 – 3751.
- [84] S. Roy, T. Bauer, M. Al-Dahhan, P. Lehner, T. Turek, Monoliths as multiphase reactors: a review. *AIChE J.* 50 (2004) 2918 – 2938.
- [85] G. Biardi, G. Baldi, Three-phase catalytic reactors. *Catal. Today* 52 (1999) 223 – 234.
- [86] M. Wallenstein, M. Kind, B. Dietrich, Radial two-phase thermal conductivity and wall heat transfer coefficient of ceramic sponges – experimental results and correlation. *J. Heat. Mass. Transfer* 79 (2014) 486 – 495.
- [87] J. Lévêque, Ph. Régis, M. Zanota, V. Meille, F. Sarrazin, L. Baussaron, C. de Bellefon, Hydrodynamics and mass transfer in a tubular reactor containing foam packings for intensification of G-L-S catalytic reactions in co-current up-flow configuration. *Chem. Eng. Res. Des.* 109 (2016) 686 – 697.
- [88] F. Lali, Characterization of foam catalysts as packing for tubular reactors. *Chem. Eng. Proc.* 105 (2016) 1 – 9.
- [89] J.-N. Tourvieille, R. Philippe, C. de Bellefon, Milli-channel with metal foams under an applied gas-liquid periodic flow: mass transfer performance and pressure drop. *Chem. Eng. J.* 267 (2015) 332 – 346.
- [90] R. Häfeli, C. Hutter, M. Damsohn, H. M. Prasser, Ph. Rudolf von Rohr, Dispersion in fully developed flow through regular

- porous structures: experiments with wire-mesh sensors. *Chem. Eng. Proc.* 69 (2013) 104 – 111.
- [91] T. H. Rehm, C. Berguerand, S. Ek, R. Zapf, P. Löb, L. Nikoshvili, L. Kiwi-Minsker, Continuously operated falling film microreactor for selective hydrogenation of carbon-carbon triple bond. *Chem. Eng. J.* 293 (2016) 345 – 354.
- [92] G. Centi, S. Perathoner, Integrated design for solid catalysts in multiphase reactions. *Cattech* 7 (2003) 78 – 89.
- [93] D. Albani, G. Vilé, M. A. B. Toro, R. Kaufmann, S. Mitchell, J. Perez-Ramirez, Structuring hybrid palladium nanoparticles in metallic monolithic reactors for continuous-flow three-phase alkyne hydrogenation. *React. Chem. Eng.* 1 (2016) 454 – 462.
- [94] M. F. Ashby, A. Evans, N. A. Fleck, L. J. Gibson, J. W. Hutchinson, H. N. G. Wadley, Metal foams: a design guide. Elsevier Inc 2000.
- [95] C. Hutter, A. Zenklusen, S. Kuhn, Ph. Rudolf von Rohr, Large eddy simulation of flow through a streamwise-periodic porous structure. *Chem. Eng. Sci.* 66 (2011) 519 – 529.
- [96] C. Hutter, A. Zenklusen, R. Lang, Ph. Rudolf von Rohr, Axial dispersion in metal foams and streamwise-periodic porous media. *Chem. Eng. Sci.* 66 (2011) 1132 – 1141.
- [97] C. Hutter, D. Büchi, V. Zuber, Ph. Rudolf von Rohr, Heat transfer in metal foams and designer porous media. *Chem. Eng. Sci.* 66 (2011) 3806 – 3814.

- [98] Y. Elias, Ph. Rudolf von Rohr, W. Bonrath, J. Medlock, A. Buss, A porous structured reactor for hydrogenation reactions. *Chem. Eng. Proc.* 95 (2015) 175 – 185.
- [99] M. Altheimer, D. Becker, F. P. D'Aleo, Ph. Rudolf von Rohr, Flow regime and liquid-solid mass transfer investigation in a designed porous structure using electrochemical micro-probes. *Chem. Eng. Sci.* 152 (2016) 699 – 708.
- [100] S. Vernuccio, R. Goy, A. Meier, Ph. Rudolf von Rohr, J. Medlock. Kinetics and mass transfer of the hydrogenation of 2-methyl-3-butyn-2-ol in a structured Pd/ZnO/Al₂O₃ reactor. *Chem. Eng. J.* 316 (2017) 121 – 130.
- [101] J. E. Samad, J. A. Nychka, N. Semagina, Structured catalysts via multiple stage thermal oxidation synthesis of FeCrAl alloy sintered microfibers. *Chem. Eng. J.* 168 (2011) 470 – 476.
- [102] A. Sarkany, Z. Zsoldos, B. Furlong, J. W. Hightower, L. Guzzi, Hydrogenation of 1-butene and 1,3-butadiene mixtures over Pd/ZnO catalysts. *J. Catal.* 141 (1993) 566 – 582.
- [103] F. Studt, F. Abild-Pedersen, Th. Bligaard, R. Z. Sørensens, C. H. Christensen, J. K. Nørskov, Identification of non-precious metal alloy catalysts for selective hydrogenation of acetylene. *Science* 320 (2008) 1320 – 1322.
- [104] R. Langsch, J. Zalucky, S. Haase, R. Lange, Investigation of a packed bed in a mini channel with a low channel-to-particle diameter ratio: Flow regimes and mass transfer in gas-liquid operation. *Chem. Eng. Proc.* 75 (2014) 8 – 18.

- [105] J.-N. Tourvieille, F. Bornette, R. Philippe, Q. Vandenberghe, C. de Bellefon, Mass transfer characterization of a microstructured falling film at pilot scale. *Chem. Eng. J.* 227 (2013) 182 – 190.
- [106] J.-N. Tourvieille, R. Philippe, C. de Bellefon, Milli-channel with metal foams under an applied gas-liquid periodic flow: Flow patterns, residence time distribution and pulsating properties. *Chem. Eng. Sci.* 126 (2015) 406 – 426.
- [107] Swiss competence center for energy research, Efficiency of industrial processes – innovation roadmap (2015). URL <http://www.sccer-eip.ch/roadmap/>
- [108] I. R. Baxendale, The integration of flow reactors into synthetic organic chemistry. *J. Chem. Technol. Biotechnol.* 88 (2013) 519 – 552.
- [109] R. L. Hartman, J. P. McMullen, K. F. Jensen, Deciding wheter to go with the flow: evaluating the merits of flow reactors for synthesis. *Angewandte Chemie – international* ed. 50 (2011) 7502 – 7519.
- [110] I. R. Baxendale, R. D. Braatz, B. K. Hodnett, K. F. Jensen, M. D. Johnson, P. Sharratt, J. P. Sherlock, A. J. Florence, Achieving continuous manufacturing: technologies and approaches for synthesis, workup, and isolation of drug substance May 20-21, 2014 Continuous manufacturing symposium. *J. Pharm. Sci.* 104 (2015) 781 – 791.
- [111] A. Marino, J. Lim, S. Keijers, S. Vanmaercke, A. Aerts, K. Rosseel, J. Deconinck, J. Van den Bosch, A mass transfer correlation for packed bed of lead oxide spheres in flowing

lead-bismuth eutectic at high Péclet numbers. *Int. J. Heat Mass Transfer* 80 (2015) 737 – 747.

- [112] R. Häfeli, O. Rüegg, M. Altheimer, Ph. Rudolf von Rohr, Investigation of emulsification in static mixers by optical measurement techniques using refractive index matching. *Chem. Eng. Sci.* 143 (2016) 86 – 98.
- [113] M. Altheimer, R. Häfeli, C. Wälchli, Ph. Rudolf von Rohr, Shadow imaging in bubbly gas–liquid two-phase flow in porous structures. *Exp. Fluids* 56 (2015) 1 – 16.
- [114] M. Altheimer, C. Wälchli, Ph. Rudolf von Rohr, Bubble tracking in bubbly gas–liquid two-phase flow in porous structures. *Multiph. Sci. Technol* 27 (2015) 27 – 49.
- [115] R. Häfeli, M. Altheimer, D. Butscher, Ph. Rudolf von Rohr, PIV study of flow through porous structure using refractive index matching. *Exp. Fluids* 55 (2014) 1 – 13.
- [116] D. Butscher, C. Hutter, S. Kuhn, Ph. Rudolf von Rohr, Particle image velocimetry in a foam-like porous structure using refractive index matching: a method to characterize the hydrodynamic performance of porous structures. *Exp. Fluids* 53 (2012) 1123 – 1132.
- [117] M. Altheimer, Gas-liquid two phase flows in structured tubular reactors. Dissertation Thesis (2017).
- [118] M. Altheimer, W. Bonrath, R. Goy, J. Medlock, Ph. Rudolf von Rohr, S. Vernuccio. Device for processing and conditioning of material transported through the device. Patent (filing date 01.05.2017).

List of publications

Journal publications

1. S. Vernuccio, Ph. Rudolf von Rohr, J. Medlock. General kinetic modeling of the selective hydrogenation of 2-methyl-3-butyn-2-ol over a commercial palladium-based catalyst. *Ind. Eng. Chem. Res.* 54 (2015) 11543 – 11551.
2. S. Vernuccio, R. Goy, Ph. Rudolf von Rohr, J. Medlock, W. Bonrath. Hydrogenation of 2-methyl-3-butyn-2-ol over a Pd/ZnO catalyst: kinetic model and selectivity study. *React. Chem. Eng.* 1 (2016) 445 – 453.
3. S. Vernuccio, R. Goy, A. Meier, Ph. Rudolf von Rohr, J. Medlock. Kinetics and mass transfer of the hydrogenation of 2-methyl-3-butyn-2-ol in a structured Pd/ZnO/Al₂O₃ reactor. *Chem. Eng. J.* 316 (2017) 121 – 130.
4. H. C. Reymond, S. Vitas, S. Vernuccio, Ph. Rudolf von Rohr. Reaction process of resin-catalysed methyl formate hydrolysis in biphasic continuous flow. *Ind. Eng. Chem. Res.* 56 (2017) 1439 – 1449.
5. S. Vernuccio, A. Meier, Ph. Rudolf von Rohr. Kinetic investigation of the solvent-free hydrogenation of dehydroisophytol. *Ind. Eng. Chem. Res.* 56 (2017) 4929 – 4937.
6. S. Vernuccio, D. Dempfle, R. Goy, J. Medlock, Ph. Rudolf von Rohr. External mass transfer in a laser sintered structured reactor for continuous hydrogenation of alkynes. *Submitted*.

Patents

1. M. Altheimer, W. Bonrath, R. Goy, J. Medlock, Ph. Rudolf von Rohr, S. Vernuccio. Device for processing and conditioning of material transported through the device (filing date 01.05.2017).

Conference contributions

1. S. Vernuccio, Ph. Rudolf von Rohr. General kinetic modeling of the selective hydrogenation of 2-methyl-3-butyn-2-ol over a commercial Pd-based catalyst. *10th European Congress of Chemical Engineering*. Nice (France) 2015 (oral).
2. S. Vernuccio, Y. Elias, Ph. Rudolf von Rohr. Understanding fundamentals of designed porous structured reactors. *Swiss Competence Center for Energy Research (SCCER) Annual Conference*. Zurich (Switzerland) 2015 (poster).
3. S. Vernuccio, Ph. Lang, Ph. Rudolf von Rohr. A structured Pd-based catalyst for the selective hydrogenation of 2-methyl-3-butyn-2-ol. *4th Zing Continuous Flow Chemistry Conference*. Albufeira (Portugal) 2016 (poster).
4. S. Vernuccio, Ph. Rudolf von Rohr. Three-phase hydrogenation of 2-methyl-3-butyn-2-ol over a Pd/ZnO catalyst: development of a kinetic model. *International Congress of Chemical and Process Engineering*. Prague (Czech Republic) 2016 (oral).
5. S. Vernuccio, Ph. Rudolf von Rohr. Kinetics of the hydrogenation of 2-methyl-3-butyn-2-ol over a structured palladium-based catalyst. *International Congress of Chemical and Process Engineering*. Prague (Czech Republic) 2016 (poster).
6. S. Vernuccio, Ph. Rudolf von Rohr. Continuous manufacturing in vitamin production. *Swiss Competence Center for Energy Re-*

- search (SCCER) Networking Meeting*. Zurich (Switzerland) 2016 (oral).
7. R. Goy, S. Vernuccio, M. Altheimer, Ph. Rudolf von Rohr, W. Bonrath, J. Medlock. Catalytic coatings for continuous and highly selective semi-hydrogenation in vitamin and fine chemical production. *13th European Congress on Catalysis*. Florence (Italy) 2017 (oral).
 8. F. Trachsel, A. Ladosz, H. Reymond, B. Tidona, M. Altheimer, S. Vernuccio, Ph. Rudolf von Rohr. Mikroreaktoren unter Druck. *Mikroverfahrenstechnik Jahrestreffen*. Frankfurt am Main (Germany) 2017 (oral).
 9. S. Vernuccio, R. Goy, D. Dempfle, J. Medlock, Ph. Rudolf von Rohr. Mass transfer in a structured reactor for continuous hydrogenation of alkynes. *13th International Conference on Gas-Liquid and Gas-Liquid-Solid Reactor Engineering*. Brussels (Belgium) 2017 (poster).
 10. S. Vernuccio, R. Goy, J. Medlock, Ph. Rudolf von Rohr. Three-phase alkyne hydrogenation in a structured reactor. *13th International Conference on Gas-Liquid and Gas-Liquid-Solid Reactor Engineering*. Brussels (Belgium) 2017 (keynote lecture).

Curriculum Vitae

Sergio Vernuccio

Date of birth: 28. January 1986

Nationality: Italian

Marital status: Single

- 04.2014 - 07.2017 Doctoral studies at the institute of Process Engineering, ETH Zurich, Switzerland.
- 01.2011 - 03.2014 Process Engineer, Technip Italy, Rome, Italy.
- 01.2011 - 10.2011 Postgraduate specialization in Design and Construction of Process Plants, University “La Sapienza”, Rome, Italy.
- 09.2008 - 10.2010 Master studies in Chemical Engineering, University “Federico II”, Naples, Italy.
- 09.2009 - 02.2010 Exchange studies in Chemical Engineering, ENSI Bourges, France.
- 09.2004 - 09.2008 Bachelor studies in Chemical Engineering, University “Federico II”, Naples, Italy.

Zurich, July 2017